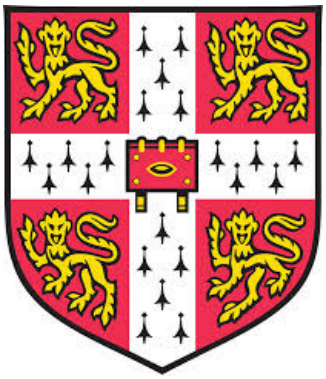
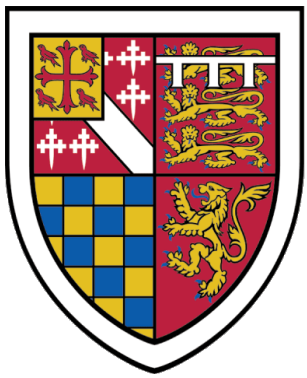
Structural evolution during the plastic deformation of nanostructured steel

Gebril M. A. M. El-Fallah

St Edmund's College
University of Cambridge





A dissertation submitted for the degree of
Doctor of Philosophy

September 2019

Cambridge, U. K.

Declaration

This thesis is submitted for the degree of Doctor of Philosophy at the University of Cambridge. The research was conducted under the academic supervision of Professor Sir H. K. D. H. Bhadeshia in the Phase Transformations and Complex Properties Research Group of the Department of Materials Science and Metallurgy between 2015 and 2019.

I declare that all of the enclosed work is original, except where explicitly acknowledged and referenced. I declare that I have not submitted this thesis, or any part thereof, for any award, degree, diploma or any other qualification at any other institution. I declare that this thesis does not exceed the prescribed limit of 60,000 words.

Aspects of this work have been published in the following academic papers:

G. M. A. M. El-Fallah, & H. K. D. H. Bhadeshia. Tensile behaviour of thermally-stable nanocrystalline bainitic-steels. *Materials Science & Engineering A*, 746:145–153, 2019.

G. M. A. M. El-Fallah, S. W. Ooi, & H. K. D. H. Bhadeshia. Effect of nickel aluminide on the bainite transformation in a Fe-0.45C–13Ni–3Al–4Co steel, and associated properties. *Materials Science & Engineering A*, 767:1–9, 2019.

Gebril M. A. M. El-Fallah
Cambridge, U.K., September 2019

Structural evolution during the plastic deformation of nanostructured steel

G. M. A. M. El-Fallah

Abstract

Nanostructured bainitic steels represent a major advance in technology, because it is now possible to produce very large quantities of three-dimensional objects containing an incredible density of interfaces. This can be done at a reasonable cost so that thousands of tonnes can actually be produced.

The nanostructure usually is a mixture of slender plates of bainitic ferrite embedded in a matrix of carbon enriched austenite. This austenite is stable under ambient conditions but can decompose into a mixture of ferrite and carbides at temperatures in the vicinity of 400 ℃. However previous research has discovered that it is possible to make the alloys heat resistant either by increasing the silicon concentration which makes carbides less stable, or by adding solutes that increase the thermodynamic stability of the austenite.

The purpose of the work presented in the thesis was to examine the stability of the steels using a variety of characterisation techniques. It is discovered for example that austenite can actually grow at temperatures as low as 400 ℃ in one of the alloys, and dramatically influence the resulting mechanical properties. This has been studied systematically and modelled mathematically to show the different kinds of behaviour that occur when mechanical properties are measured at temperature.

In the alloy variant that does not contain nickel as an austenite stabilising element, it is the precipitation of carbides at relatively high testing temperatures that leads to a significant deterioration of properties. The temperature at which this occurs is much higher than in "conventional" nanostructured steels.

In another scenario it has been demonstrated that it is possible to precipitate intermetallic compounds which then influence the progress of transformation. Detailed kinetic measurements and microscopy have shown that the intermetallic compounds influence kinetics either by depleting the parent phase from certain solutes, or by stimulating the intragranular nucleation of bainitic ferrite.

The major outcome of this work is that there is a new understanding of the thermal stability of high silicon or high nickel bulk nanostructured bainitic steel. In addition, it is possible now to specify the optimum stability of the austenite in the nanostructure with respect to achieving the best mechanical property combinations.

Acknowledgements

I would first like to sincerely thank my academic supervisor, Professor Sir Harshad Kumar Dharamshi Hansraj Bhadeshia for all his frequent and vital advice, ideas, encouragement and patience. It was a great relief to always find help, assistance and advice whenever I needed it. His astonishing knowledge and experience allowed me to progress in my Ph.D. at a pleasantly fast pace. Sincere thanks also to Libyan Higher Education and Scientific Research for funding this project, and in particular to Dr Mohammed Hassan Abu-Bakr.

I would also like to thank Professor Paul Midgley for the provision of laboratory facilities in the Department of Materials Science and Metallurgy at the University of Cambridge. I must give special mention to those without whom this project would have been much more difficult, all of whom have my heartfelt gratitude: Andrew Moss for getting me started with X-ray diffractometry, Simon Griggs for his help with scanning electron microscopy, Chris Dolan and Giorgio Divitini for assistance with transmission electron microscopy, Paul Stokes and Susan Rhodes for sample machining.

I am thankful to the past and present members of the Phase Transformation and Complex Properties group for their help and friendship. Steve Ooi and Chris Hulme-Smith deserve special mention for much useful discussions and help with the project. My sincere thanks to Mathew Peet, Tim Ramjaun, Wilberth Solano Alvarez, Arunim Ray, Guo Lei, Neel Bhattacharya, Joachim Dias, Zixin Huang, Shaumik Lenka, Appa Rao Chintha and Mohammed Alshahrani for their friendship and for made my laboratory and office a lovely place to work.

Rosie Ward, Anita Bailey and Jean Pomfrett need a special mention on helping me over official matters. Special thanks to my undergraduate friends, Divesh Soni, Bishal Chalise, Omear Gul and Waleed Khawaja, for providing me with all the necessary entertainment.

I will be eternally grateful to my lovely wife, Helena, for all the support, practical help, tolerance and patience over the last years of this project.

Finally, I would like to express my profound gratitude to my family, especially my beloved Mum for her support, good wishes, endless encouragement and many sacrifices over the years to help me achieve what I have. Without her support this venture would not have been fulfilled.

بِسْمِ اللَّهِ الرَّحْمَٰنِ الرَّحِيمِ

﴿لَقَدْ أَرْسَلْنَا رُسُلَنَا بِالْبَيِّنَاتِ وَأَنزَلْنَا مَعَهُمُ الْكِتَابَ وَالْمِيزَانَ لِيَقُومَ النَّاسُ بِالْقِسْطِ وَأَنزَلْنَا الْحَدِيدَ فِيهِ بَأْسٌ شَدِيدٌ وَمَنَافِعُ لِلنَّاسِ وَلِيَعْلَمَ اللَّهُ مَن يَنصُرُهُ وَرُسُلَهُ بِالْغَيْبِ إِنَّ اللَّهَ قَوِيٌّ عَزِيزٌ﴾ سورة الحديد آية ﴿٢٥﴾

{We have already sent our messengers with clear evidences and sent down with them the scripture and the balance that the people may maintain [their affairs] in justice. And We sent down iron, in which is [material for] mighty war, as well as many benefits for the mankind, and so that Allah "God" may make evident those who support him and his messengers unseen. Indeed, Allah is powerful and exalted in might.}❀

Quran, Chapter (57) – *The Iron*, Verse (25)

Nomenclature

Ae_3	the highest temperature at which ferrite is thermodynamically stable at equilibrium
α	ferrite
α'	martensite
α_a	acicular ferrite
α_i	idiomorphic ferrite
α_{lb}	lower bainite
α_{ub}	upper bainite
α_w	Widmanstätten ferrite
BCC	body-centred cubic
B_S	bainite-start tempeature
β-NiAl	nickel aluminide, NiAl
CCT	continuous cooling transformation diagram
d	grain size
δ	delta (high temperature) ferrite

EDM	electrical discharge machining
ε	total strain
ε_{e}	elastic component of strain
ε_{p}	plastic component of strain
$\boldsymbol{\varepsilon}$	epsilon carbide, $Fe_{2.4}C$
FCC	face-centred cubic
$\boldsymbol{\gamma}$	austenite
$\boldsymbol{\gamma}$'	austenite existing in equilibrium with other products following the transformation of austenite of a different composition
γ_{p}	plastic shear strain
$\boldsymbol{\gamma}_{\mathrm{r}}$	retained austenite
IPS	invariant plane strain
$\bar{L}$	mean lineal intercept
$\boldsymbol{\alpha}'_{\mathrm{T}}$	twins martensite
M_{F}	martensite-finish tempeature
M_{S}^{γ}	martensite-start temperature for the case where the alloy is fully austenitic
$M_{\mathrm{S}}^{\gamma\mathrm{r}}$	martensite-start temperature for the retained austenite structure
M_{S}	martensite-start tempeature
R_{exp}	expected R-factor

R_{wp}	weighted profile R-factor
SEM	scanning electron microscopy
σ_{UTS}	ultimate tensile strength
σ_{y}	yield stress
T_0	the temperature at which austenite and ferrite of the same composition have the same Gibbs free energy
T_0'	the temperature at which austenite and ferrite of the same composition have the same Gibbs free energy if the stored strain energy is taken into account
TEM	transmission transmission electron microscopy
TTT	time-temperature transformation
θ	cementite, Fe_3C
VAR	vacuum arc remelting
VIM	vacuum induction melting
W_{s}	Widmanstätten-start temperature
XRD	X-ray diffraction
x_{T_0}	carbon content of austenite and ferrite of the same composition and Gibbs free energy at a specified temperature
$x_{T_0'}$	carbon content of austenite and ferrite of the same composition and Gibbs free energy at a specified temeprature if the stored strain energy is taken into account

Contents

Academic Declaration **i**

Acknowledgements **v**

Nomenclature **ix**

Contents **xiii**

1 Introduction **1**

2 Scientific background **5**

2.1 Transformations in steel 5

2.1.1 Reconstructive transformations 6

2.1.2 Pearlite 7

2.1.3 Martensite 7

2.1.4 Bainite 9

2.1.5 Distribution of carbon 10

2.1.6 Shape change 15

2.1.7 Mechanical properties of bainite 16

2.2 Nanostructured bainitic steels 18

2.2.1 Alloy design 18

2.2.2 Thermal stability of nanostructured bainitic steels 24

2.3 Nanostructured bainite: some special effects 24

2.4 Steel with mixture of transformation products 26

2.5 Summary 28

3 Experimental Methods **29**

3.1 Materials 29
3.2 Sample preparation 30
3.3 Microstructural observations 30
3.3.1 Optical microscopy 30
3.3.2 Scanning electron microscopy 31
3.3.3 Electron back-scatter diffraction 31
3.3.4 Focused ion-beam milling of samples 31
3.3.5 Transmission electron microscopy 32
3.3.6 X-ray diffraction 32
3.4 Metallurgical experiments 32
3.4.1 Thermodynamic calculations 32
3.4.2 Dilatometry 33
3.4.3 MTTTData 34
3.5 Mechanical testing 34
3.5.1 Hardness measurement 34
3.5.2 Tensile tests 35
3.5.3 Toughness tests 36

4 Phase transformations **39**

4.1 Initial microstructures 39
4.2 Initial experiments 39
4.2.1 M_S temperature 41
4.2.2 Transformation kinetics of Alloy A 42
4.3 Dilatometric study of phase transformations 45
4.3.1 Experimental determination of martensite start temperature 45
4.4 Transformation kinetics 46
4.5 Transformation microstructures 49
4.5.1 Alloy A 49
800 ℃ 55

750 ℃ and 700 ℃ 55
650 ℃ 59
600 ℃ and 550 ℃ 63
500 ℃ – 400 ℃ 66
Below 400 ℃ 68
4.5.2 Alloy B 71
600 ℃ and 450 ℃ 71
350 ℃ and 300 ℃ 73
250 ℃ 75
4.6 Conclusions 76

5 Tensile deformation of stable bainite **77**
5.1 Heat treatment 77
5.2 As-transformed microstructures 78
5.3 Mechanical behaviour 79
5.4 Retained austenite 82
5.5 Austenite reversion in Alloy B 86
5.6 Cementite precipitation 90
5.7 Mechanical stability of retained austenite 94
5.8 Conclusions 99

6 Bainite with intermetallic-compound **101**
6.1 Experimental procedure 102
6.2 Heat treatment 102
6.3 Dilatometry 105
6.3.1 Kinetics of the bainite transformation 109
6.4 Deformation of austenite 113
6.5 Microstructural observations 115
6.6 Hardness measurements 119
6.7 Mechanical properties 119
6.7.1 Toughness 119
6.7.2 Tensile properties 122

6.8 Fractograph 126
6.9 Conclusions 131

General conclusions **133**
Future work 135

A SEM micrographs of Alloy B **xvii**

B EBSD orientation images of Alloy B **xviii**

C SEM fractographs of Alloy B **xx**

Bibliography **xxii**

Chapter 1

Introduction

The introduction of thermomechanical processing and microalloying has resulted in the production of millions of tonnes of dependable steel, one of the greatest triumphs of the twentieth century [1]. The idea that a fine structure is always good for ambient temperature properties, and in particular the expectation that strength and toughness should simultaneously improve, became engrained in metallurgy following the tremendous success of microalloyed, thermomechanically processed steels. The increase in strength is easy to explain because boundaries present barriers to the transfer of slip, whereas toughness is said to increase primarily because other phases, such as cementite which are more brittle, are also refined during the processing. Hence the drive to refine the structure even beyond the capabilities of established thermomechanical processing methods. Even though nanostructured materials are the fashion of the day, to take the idea to a point where nanostructured steel can be produced industrially has been more difficult than anticipated. Many methods have been studied including:

- **Shape preserving deformations:** severe plastic deformation that preserves shape, for example, equal channel angular processing [2], where the entry and exit cross-sections of an extruded sample are identical, the deformation achieved by forcing the entire sample around a corner. Substantial samples can be produced by this method, sufficient to do both structural and

mechanical characterisation, but not suitable for mass production because the process is onerous on the die material and expensive to scale up in the case of steels.

Another such method is accumulative roll-bonding [3, 4] which involves plane strain deformation by rolling, of two separate pieces of steel which become cold-bonded as they emerge from the rolls. The final thickness is identical to that of the individual pieces. Therefore, this also is a shape-preserving solution and one that can be scaled up using conventional rolling equipment that already exists in industry. However, the properties achieved are not particularly impressive with strengths reaching about 850 MPa with a ductility of just 3 % [5]. Better properties can routinely be obtained in a much simpler manner in commercially available steels.

- **Shape altering deformations:** Extreme strength in excess of 3 GPa can be obtained in steel wires and ropes which being with a pearlitic microstructure prior to deformation by drawing. These wires and ropes have major applications such as reinforcement in automotive tires, in cables for suspension bridges and cranes etc. However, the shape is limited to circular cross-sections.

In contrast, there is an approach based on bainite that achieves the required nanostructure and can be delivered in large volumes and in sizes that are large in all dimensions at an affordable price [1]. Before discussing this, it is useful to consider some elementary aspects of strengthening and to introduce the meaning of nanostructures.

Nanostructured bainitic steels are an ongoing area of development in steel metallurgy, delivered by means of the bainite transformation at temperatures in the range 150 °C – 350 °C. The follow-up material contains exceptionally fine combinations of irregular platelets of bainitic ferrite, commonly ≈ 50 nm wide and *films* of retained austenite, ≈ 50 nm wide, together with greater *blocks* of retained austenite, typically a few micrometres in size.

The disruption in the methodical arrangement of atoms is essentially one of the principles of metallurgy which leads to strengthening of the material as long as the temperature and time of the investigation are adequately small to prevent the diffusion of atoms. These low-temperature bainitic steels show remarkable combinations of strength and toughness. Most steels with extremely fine grain structures are delivered either by fast cooling or by serious plastic deformation, so there is a limitation on the size and state of the material that can be formed. However, the production of nanostructured bainite does not require deformation or rapid cooling, it requires heat treatment alone to achieve the nanostructure. The packing density of that interfaces is so intense, that in combination with the presence of retained austenite, the material has a natural work hardening mechanism that results in exceptional properties. This type of steel can be strong, ductile and sensibly tough, although the latter can do with improvement.

Macroscopic defects, for example dislocations, can be produced in single crystals and in this manner the material can be strengthened. The volume of the single crystals impacts its quality when it is compared to the volume per defect. This is on the grounds that it is more probable that a small crystal can be and is perfect [6]. Polycrystalline samples can be more isotropic and both the orientation of the grain boundaries and the relative orientation of the crystals that they connect can additional variable. To ensure ductility, every crystal must have the capacity to slip on no less than five independent slip systems, thus enhancing the work hardening capacity [7].

It then becomes harder to characterise the structure of the grain boundaries and their capacity to disrupt the stream of matter when the objects inside of a polycrystalline material have a variety of crystal structures. The resulting interphase interfaces are generally more difficult for dislocations to penetrate [8]. Both multiple phases and fine precipitates can contribute to work hardening which is essential for avoiding plastic instabilities and hence ductility [9, 10]. Refining the crystal size leads to increased strength which is regularly expressed via the Hall-Petch equation which relates the yield stress and the grain size for equiaxed structures

[11, 12]. For plate-shaped grains the strength relies on $(\bar{L})^{-1}$, where $\bar{L}$ is the mean lineal intercept defining the crystal size [13, 14].

The refinement of crystal size during the thermomechanical processing is a triumph of micro-alloying, where current steels routinely reach a grain size of 10 μm. Furthermore, with the progress of thermodynamic principles, steels with a grain size of 1 μm are now possible [15]. It is logical therefore, to go for much smaller grain sizes to create tough and strong steels that can be mass produced particularly where mass must be limited, such as in an aerospace application [16, page 230] [17, page 12].

One possible application of nanostructured bainitic steels is as parts in gas turbine engines, supplanting different ferrous alloys that are unlikely to serve future engine designs. The material use in such applications needs to perform for prolonged timeframes at fairly higher temperatures (e.g. 350 °C for 40000 h). Current nanostructured bainitic steels are not thermally stable and this makes them unsatisfactory for use at high temperatures that are substantially greater than that required to generate the nanostructure.

Nanostructured bainite cannot easily be joined by welding [18]. Many attempts have been made, some of them quite ingenious, but all impractical. It is likely, given the level of overall activity in the field, that the methodology utilised for the design of the nanostructured bainite will prompt another class of lower strength steels with a more extensive range of properties and further applications than have been accomplished so far. However, damage mechanisms in these systems have not been characterised or understood in detail.

The purpose of the work described in this thesis is to investigate, in thermally stable alloys how the nanostructure influences mechanical properties. There was a need to gain a generic, quantitative and mechanistic understanding of the mechanical behaviour of mixtures of bainitic ferrite plates and retained austenite, irrespective of the scale of the structure therein.

Chapter 2

Scientific background

2.1 Transformations in steel

A wide variety of the physical properties of steels can be obtained by carefully controlling the processing conditions. This is one of the main reasons, along with low production costs, that makes steel the most widely used amongst the metals. Nevertheless, the production of steel is extremely polluting in terms of CO_2. Developments that improve the mechanical properties of steel without increasing the cost of production would not only allow a reduction in the consumption of steel but also would result in a positive impact on the environment.

During processing it is common for steel to be heated to temperatures in excess of 1000 ℃, so that austenite, which has a face-centred cubic crystal structure is generated. Various phase changes occur when the steel is then cooled to ambient temperatures. In particular, at temperatures below about ~ 900 ℃, a body-centred cubic structure called ferrite becomes stable.

These changes in stability as a function of temperature, and indeed of chemical composition and processing, can be exploited to control the structure and properties of steels. Moreover the changes can occur by a variety of atomic mechanisms so that the palette of microstructures available becomes quite extensive, more so than many other common metallic systems.

Transformations where diffusion is not an essential are accomplished by the concerted motion of atoms, leading to systematic displacements. Others involve the breaking of bonds and reconstruction into another structure in a manner that is closer to equilibrium. The common transformations in steels are described briefly before progressing into topics of most relative to the research reported in the theses.

2.1.1 Reconstructive transformations

If heat treatments are carried out in circumstances where there is sufficient atomic mobility, then the system may reach close to thermodynamic equilibrium, whereby all elements are able to migrate to minimise the overall Gibbs free energy of the system. *Allotriomorphic ferrite*, which follows the contours of austenite grain boundaries, has a shape which does not reflect its internal crystalline symmetry. *Idiomorphic ferrite* nucleates intragranularly (e.g., on inclusions). It has a crystallographically faceted shape [10]. These structures are illustrated schematically in Fig. 2.1.

Both of these morphologies involve the diffusion of all atoms and hence are in the category of reconstructive transformations. They can occur only if diffusion is possible over length scales consistent with the size of the transformation product, and within the time scale of the experiment.

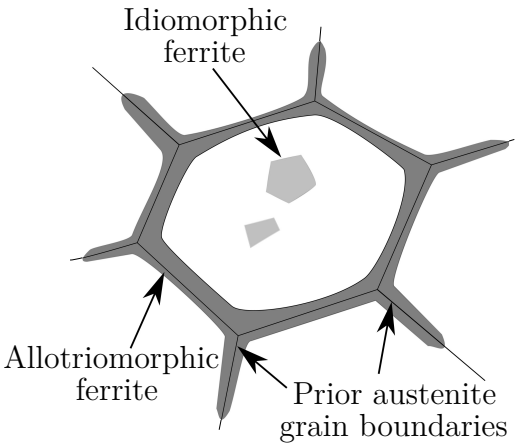


Figure 2.1: Schematic illustration of grain boundary allotriomoph of ferrite and intragranular idiomorphic ferrite.

2.1.2 Pearlite

Pearlite generated by the cooperative growth of ferrite and cementite from the parent austenite. In Fe-C systems, the average chemical composition of the pearlite is equal to that of the austenite; the latter can then entirely transform into pearlite. In a hypoeutectoid steel, a colony of pearlite grows with the nucleation of ferrite as illustrated schematically in Fig. 2.2a. This in turn initiates the nucleation of a particle of cementite. The two phases then are able to establish cooperative growth Fig. 2.2b at the single front with the austenite phase, with much of the solute diffusion happening within the austenite parallel to the front.

2.1.3 Martensite

Martensite tends to form when there is a large driving force and in circumstances (such as low temperature or high strain rate) where atomic mobility is limited. The transformation is generally athermal meaning that the increase in volume fraction of martensite occurs only by increasing the undercooling below the M_S temperature. Note that when pearlite forms in substitutionally alloyed steel, de-

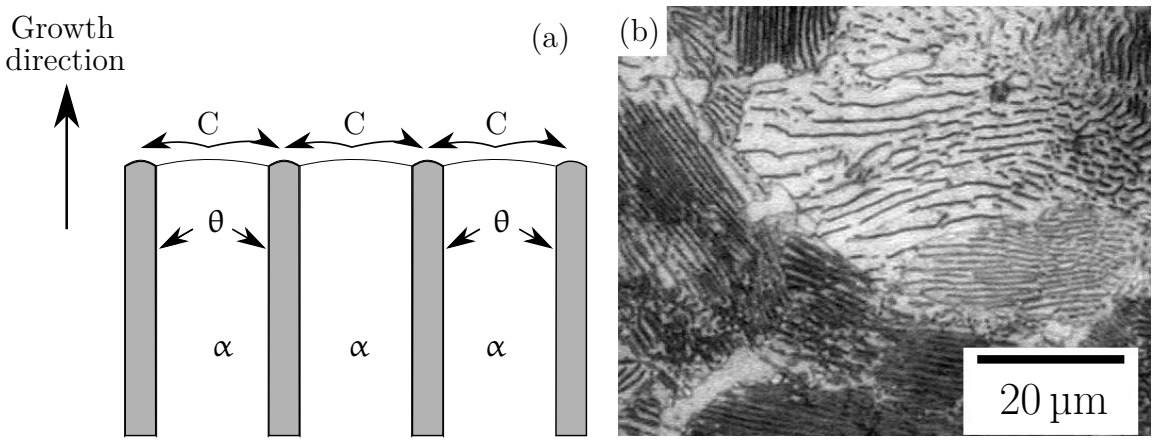


Figure 2.2: Schematic representation of the growth of a colony of pearlite, α and θ refer to ferrite and cementite respectively. Optical micrograph showing pearlitic microstructure, where the dark lamellae are cementite, adapted from [19, micrograph 15].

composition of the austenite change during the course of transformation. This is because cementite, austenite and ferrite can coexist in equilibrium and the pearlite reaction may not then go to completion.

This is because the nuclei become easily exhausted during cooling so further progress is made only when the temperature is reduced and less potent nuclei can be activated at the greater driving force than available. The accumulation of strain as the transformation progresses may also have a role in this behaviour. Diffusionless transformation is achieved by the deformation of the parent lattice, so it is amenable to rapid growth, controlled only by the rate at which atoms can move in a synchronised manner. It is not surprising therefore that there may be acoustic emissions accompanying rapid growth, in some cases reported to be at the speed of sound in the metal [20–22].

In alloys containing large concentrations of solutes (e.g., Fe-30Ni wt%), the plate shape of martensite is obviously revealed because substantial amounts of retained austenite exist in the microstructure, as shown in Fig. 2.3a. However, lower alloy steels transform almost entirely into martensite when cooled adequately rapidly.

Thus, the microstructure looks different (Fig. 2.3b) but still contains plates or laths of martensite.

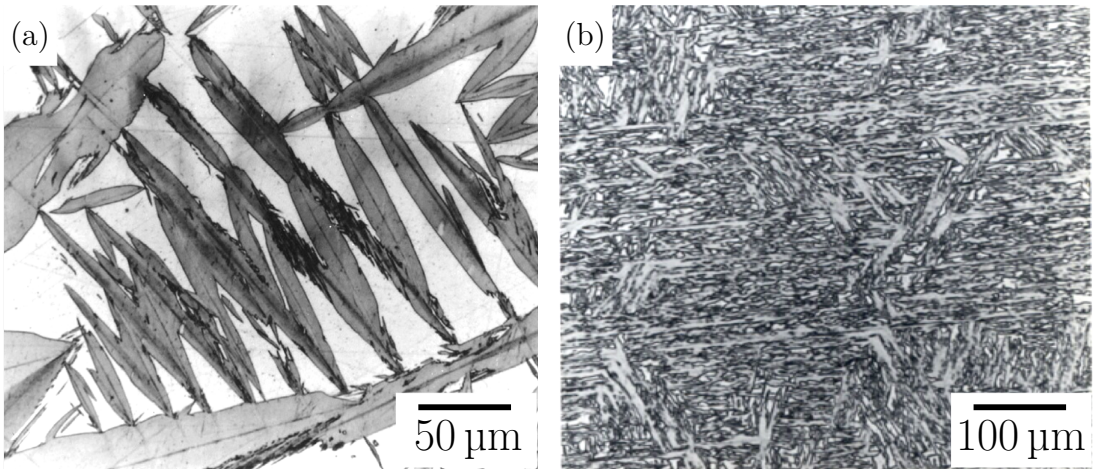


Figure 2.3: Optical micrographs of martensite, (a) Lenticular martensite in a nickel-rich steel. Adapted from [10, micrograph 5.11]; (b) Martensite in a low-alloy steel, adapted from [23, micrograph 28].

2.1.4 Bainite

Martensite forms at undercoolings where there is a large driving force that is able to overcome the barrier to diffusionless nucleation. Other transformations can happen at smaller undercoolings because there are mechanisms which lead to an increase in the available driving force, for example by the partitioning of carbon during the nucleation stage or during both the nucleation and growth stages. And yet, these mechanisms can lead to displacive transformation because carbon is an interstitial element, whose motion does not affect the generation of the new crystal structure.

Bainite "α_b" is able to form at temperatures that are too high to sustain diffusionless nucleation, but where diffusionless growth is possible [24]. Although growth is diffusionless, the carbon is able to partition into the austenite shortly

after growth has ceased. The highest temperature at which bainite forms is designated the bainite-start temperature, B_S [25]. This is at the upper limit to the bay between the overlapping curves of pearlite and bainite in some steels in the ***t**ime-**t**emperature-**t**ransformation* "TTT" diagram [26].

2.1.5 Distribution of carbon

Bainite grows at temperatures where any excess carbon inherited during growth tends subsequently to migrate into the residual austenite and precipitates as cementite between the aggregated ferrite platelets [27–29], leading to *upper bainite* "α_{ub}" (Fig. 2.5a). The aggegates of plate are called *sheaves* [30] and the plates within each sheaf are known as *sub-units*. At lower temperatures, the partitioning is slower, so there is an opportunity for precipitation inside the ferrite plates as well, [1, 31, 32] leading to *lower bainite* "α_{lb}" (Fig. 2.5b). The lower bainite sub-units tend to be finer than those in upper bainite, but both morphologies are similar in terms of microstructure and crystallography. The carbides are extremely fine in the lower bainite. Since they precipitate inside the ferrite plates Fig.2.4, a smaller amount of carbon migrates into the residual austenite. This leads to fewer and finer cementite particles between the ferrite plates when compared to the upper bainite microstructure Fig.2.4. An essential consequence is that, despite its greater strength, the lower bainite is usually found to be much tougher than the upper variety. In upper bainite, the coarse cementite particles are well-known for their ability to nucleate voids and cleavage [10].

In the same steel, upper bainite forms at higher temperatures (≈ 550 – $400\,^{\circ}\mathrm{C}$) than lower bainite (≈ 400 – $250\,^{\circ}\mathrm{C}$). The carbon concentration of the steel also determines the mechanism of the transition [10]. Mixtures of upper and lower bainite can be achieved by isothermal transformation because the carbon concentrations of the residual austenite changes as more bainite forms. A greater carbon concentration favours lower bainite because it takes longer for carbon to partition.



Figure 2.4: Schematic representation of the microstructural features of upper and lower bainite, after [10].

Elements that are insoluble in cementite, particularly silicon, can suppress precipitation during the bainite transformation leading to *carbide-free bainite*. A remarkable microstructure results when the silicon-alloyed steel (normally contains 1.5 Si wt%) is transformed into upper bainite. The carbon that has migrated into the residual austenite, remains there and stabilises the austenite down to ambient temperature, rather than precipitating as cementite. As a result, the microstructure consists of a mixture of bainitic ferrite plates separated by carbon-enriched austenite regions [27]. Since the bainitic ferrite plates are almost free of carbon, in high-strength steel and during plastic deformation it expected that the microstructure becomes more resistance to failure. However, by suppressing cementite precipitation, there may remain regions of relatively large blocks of austenite between the sheaves of bainite, that readily transform into martensite under stress. This untempered, hard and coarse martensite can severely embrittle the steel [33–35]. Such blocks of austenite are therefore unfavourable to toughness, so any attempt to reduce their fraction or increase their stability to martensitic transformation, would be beneficial. This effect can be controlled by altering the alloy composition to shift the thermodynamic limit to the austenite carbon concentration to larger values.

Given the mechanism of transformation, and in the absence of carbide precipitation, the formation of α_b will stop when the austenite composition reaches a point where diffusionless transformation is thermodynamically impossible. This is defined by the temperature at which ferrite and austenite of identical composition have the same free energy, identified as T_0 on a plot of temperature versus carbon content. The corresponding limiting carbon content at any temperature is donated

as x_{T_0}. When the strain energy due to the displacement accompanying bainite is taken into account, the T_0 curve is converted to T_0', and x_{T_0} to $x_{T_0'}$.

The T_0 and T_0' curves in a Fe–x C–1.0 Mn (wt%) steel are shown in Fig. 2.6a and the relation between the T_0 line and the equilibrium austenite and ferrite phase regions is shown in Fig. 2.6b. Experimental data showing that the growth of bainite stops when carbon content of the retained austenite reaches the T_0' line has been demonstrated elsewhere [1, Fig. 5.5b].

The amount of austenite that transforms to bainite is gradually increased as the transformation temperature is reduced below B_S temperature [36, 37]. However, a threshold is reached during isothermal transformation beyond which austenite will no longer transforms to bainite, despite a substantial quantity of austenite that remains untransformed. The reaction is said to be *incomplete* since the transformation actually ceases before the austenite reaches its equilibrium composition. At a given temperature, the extent of the incomplete transformation for steel is composition-dependent; higher carbon contents will reduce the degree of transformation, however, this phenomenon cannot be easily detected in plain carbon steels where cementite precipitation allows the transformation to proceed to completion [38].

To place the bainite transformation into context, Table 2.1 lists the key transformation characteristics in steels [41, 42]. Consistency of a characteristic with the transformation concerned is indicated by ✓, inconsistency by ×, a bullet • identifies the case where the comment is only sometimes consistent with the transformation. The term *parent* γ implies the γ grain from which the product phase grows. In the context of bainite transformation, many of the characteristics presented in the table have already been discussed in the previous sections. The ability of the elements to re–arrange themselves into a new structure plays a significant role in both the nucleation and growth of the product phase. As can be seen in Table 2.1 many of the transformation products require diffusion and therefore the critical role of temperature in determining structure.

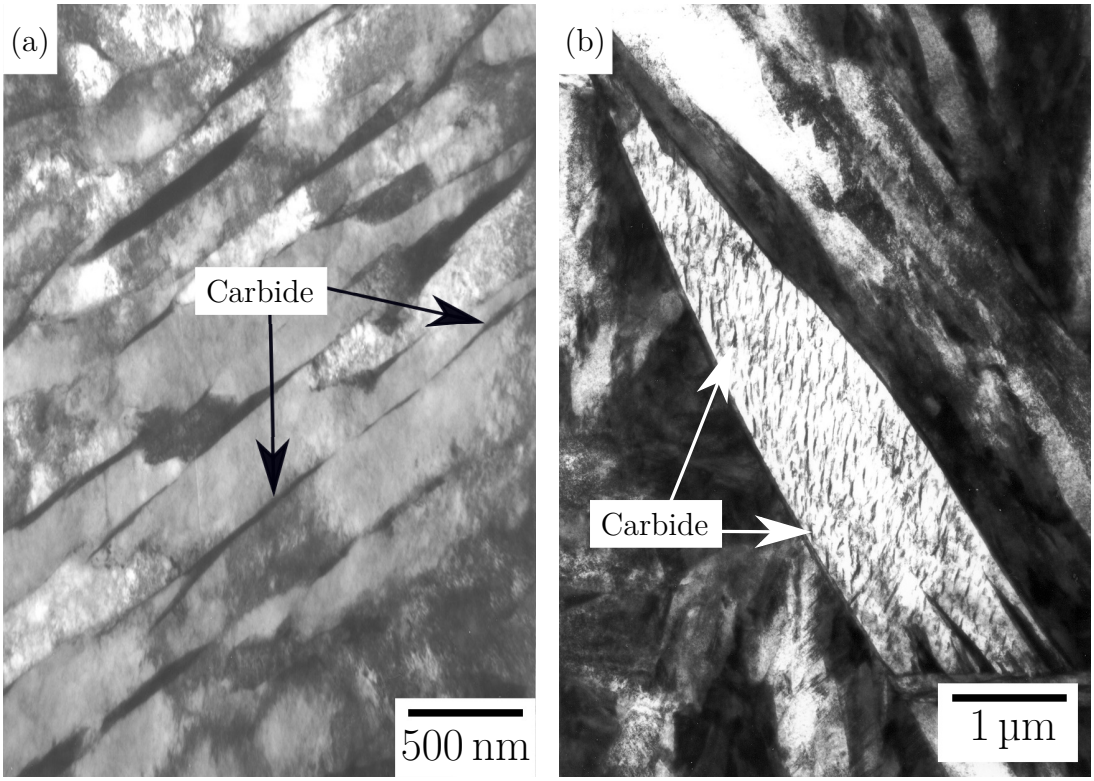


Figure 2.5: Transmission electron micrograph showing carbide precipitation in (a) upper and (b) lower bainite [39, adapted].

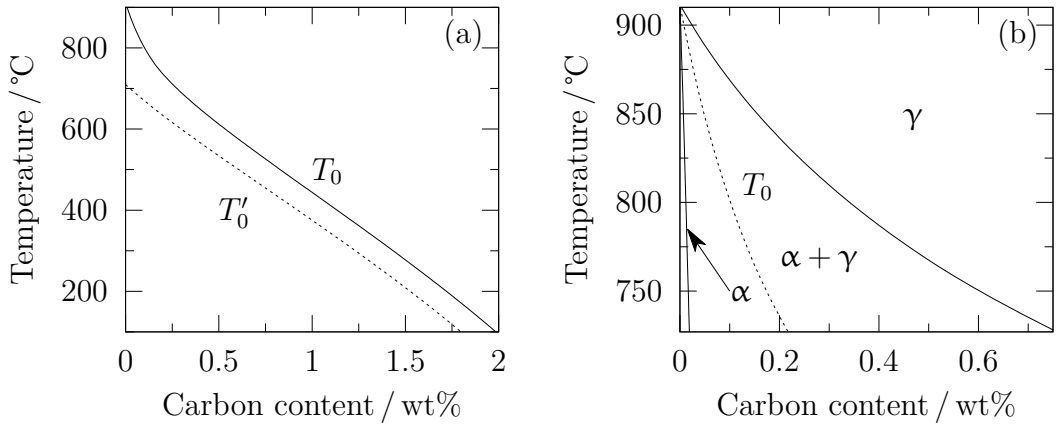


Figure 2.6: (a) T_0 and T_0' curves; (b) the T_0 curve in the equilibrium phase diagram for Fe–x C calculated using MatCalc software [40]

Comment	α'	α_{lb}	α_{ub}	α_{a}	α_{w}	α	α_{i}	P
Nucleation and growth reaction	✓	✓	✓	✓	✓	✓	✓	✓
Plate shape	✓	✓	✓	✓	✓	×	×	×
IPS shape change with large shear	✓	✓	✓	✓	✓	×	×	×
Lattice correspondence during growth	✓	✓	✓	✓	×	×	×	×
Co-operative growth of ferrite and cementite	×	×	×	×	×	×	×	✓
High dislocation density	✓	✓	✓	✓	•	×	×	×
Necessarily has a glissile interface	✓	✓	✓	✓	✓	×	×	×
Always has an orientation within the Bain region	✓	✓	✓	✓	✓	×	×	×
Grows across austenite grain boundaries	×	×	×	×	×	✓	✓	✓
High interface mobility at low temperatures	✓	✓	✓	✓	✓	×	×	×
Acoustic emissions during transformation	✓	✓	✓					
Reconstructive diffusion during growth	×	×	×	×	×	✓	✓	✓
Bulk redistribution of X atoms during growth	×	×	×	×	×	•	•	•
Displacive transformation mechanism	✓	✓	✓	✓	✓	×	×	×
Reconstructive transformation mechanism	×	×	×	×	×	✓	✓	✓
Diffusionless nucleation	✓	×	×	×	×	×	×	×
Only carbon diffuses during nucleation	×	✓	✓	✓	✓	×	×	×
Reconstructive diffusion during nucleation	×	×	×	×	×	✓	✓	✓
Often nucleates intragranularly on defects	✓	×	×	✓	×	×	✓	×
Diffusionless growth	✓	✓	✓	✓	×	×	×	×
Local equilibrium at interface during growth	×	×	×	×	×	•	•	•
Local paraequilibrium at interface during growth	×	×	×	×	✓	•	•	×
Diffusion of carbon during transformation	×	×	×	×	✓	✓	✓	✓
Carbon diffusion-controlled growth	×	×	×	×	✓	•	•	•
Incomplete reaction phenomenon	×	✓	✓	✓	×	×	×	×

Table 2.1: Characteristics transformation for decomposition of austenite in steels. Martensite α', lower bainite α_{lb}, upper bainite α_{ub}, acicular ferrite α_{a}, Widmanstätten ferrite α_{w}, allotriomorphic ferrite α, idiomorphic ferrite α_{i}, pearlite P, substitutional solutes X. After [41].

2.1.6 Shape change

The similarity between martensitic and bainitic transformations has been established for a long time [43], with much attention when it was demonstrated that both transformations display surface relief [44]. Hull [45], and later Christian [46], suggested that martensitic transformations could be differentiated experimentally by changing the shape of the transformed regions. Christian also commented that surface relief is not necessarily an indication of non-diffusional transformation [47], and may also result in cases where the solvent atoms can spread faster and order of magnitude than the solvent. Therefore, surface relief cannot give indication whether a displacive transformation occurs with or without carbon diffusion, but due to the lattice correspondence between the parent and the product phases it is a necessary characteristic of martensitic transformation. Martensite, bainite, and Widmanstätten ferrite all display a surface relief with no carbon diffusion in martensite while carbon diffusion control of the Widmanstätten transformation. Note that the relief here refers specifically to an invariant–plane strain with a large share component, not simply rumpling caused by a disorderly volume change.

The shape change due to bainite creates a large shear strain of about 0.22–0.28 [48–50]. The measurement of twin boundary displacement after transformation observed in the transmission electron microscope confirmed this value [51]. The austenite is relatively weak at this temperature and this large deformation causes plastic relaxation in the parent austenite in the vicinity [52]. The resulting dislocation tangles in the austenite [33] hinders the continued growth of the bainite plates, giving the sub-unit and sheaf hierarchies in the microstructure of bainite. The relaxation due to the displacements significantly also decreases the overall stored strain energy relative to an elastically accommodated shape deformation. Sustained transformation leads to further deformation and accumulation of dislocation density in both the parent and product phases. Thus, the parent austenite around the bainitic ferrite is work hardened and this is what stifles the growth of bainitic ferrite by an effect known as mechanical stabilisation.

Therefore, the sheaf as a whole grows by the stimulation of new sub-units, mainly near the tips of the stifled platelet, where the amount of carbon is minimum due to the small volume of the adjacent ferrite and where the elastic strains favour the formation of a new sub-units in the same orientation.

2.1.7 Mechanical properties of bainite

In simple terms, in strong steels, toughness and ductility have their origin in the retained austenite while ferrite provides the strength [1, page 303]. The number of carbide particles per unit volume naturally increases with the carbon content [53], but in strong steel they initiate voids during plastic deformation and hence limit ductility. At low testing temperatures, the carbides can assist cleavage crack initiation [34, 54].

Normally, the strength of steels can be improved by reducing the austenite to ferrite transformation temperature [55]. It usually is true that reduced temperature results in a finer plate size of the transformation product, higher dislocation density and refined precipitated phases. Pickering's results [55] demonstrate a linear relation between the transformation temperature and strength over a broad spectrum of bainite transformation temperatures; Davenport and Bain reported similar results following isothermal transformation at a variety of temperatures [56]. It is notable that fully martensitic steels can be stronger than their bainitic counterparts after continuous cooling, although they usually need to be tempered in order to achieve a balance of properties. Due to the large size of the carbides and the additional difficulty in applying isothermal transformation, early bainitic steels did not perform relative to the quenched and tempered martensitic steels. Irvine and Pickering therfore introduced low-carbon steels alloyed with boron and molybdenum [57] which delayed pearlite without significantly delaying the rate of the bainite transformation. In the latter case, following initiation at the austenite grain boundaries, the subsequent nucleation rate is dominated by autocatalysis [1].

When steels fail to transform fully to bainite, ductile void formation initiates at the hard regions of untempered martensite resulting from the carbon-enriched residual austenite transformation [58]. The brittle fracture of martensite initiates void or cleavage growth. This is the reason the elongation of completely bainitic low-carbon steels is consistently superior to that of tempered martensite of the same strength, though the circumstance switches on the case of high-carbon steels [59]. When the carbon content is large, it is harder to get fully bainitic microstructures free from untempered martensite.

Later, a laminar water jet system [60] was used to introduce greater cooling rates, and leaner alloys with greater strengths could be produced, result in the development of high–strength–low–alloy steels [61]. Important steel classes were produced to use retained austenite as additional plasticity enhancement. ***Tr****ansformation* ***i****nduced* ***p****lasticity* (TRIP) and TRIP–assisted steels [62–64] and dual–phase steels are now common jargon. The principle has recently been promoted with the ***tw****inning* ***i****nduced* ***p****lasticity* (TWIP) aided steels [65].

TRIP was first observed in fully austenitic steels where large quantities of austenite-stabilising solutes were used, during deformation above their martensite-start temperature. The potential of TRIP–aided carbide–free steels was reported by Matsumura and co-workers [64], where carbon in the austenite resulting from transformation was used to stabilise the austenite. The transformation of bainite has been used to obtain adequate carbon enrichment austenite regions that are stable enough to be retained in the microstructure, but are accessible for transformation upon deformation. Martensitic transformation induced by local stress has the effect of relieving stress concentrations, increasing the work-hardening rate, and stimulating homogeneous deformation, resulting in enhanced steel strength, ductility and toughness. However, the existence of retained austenite enables the strain-hardening rate to be maintained to greater elongations in the TRIP-assisted steels. Having retained austenite in the final bainitic steel microstructure allows a better controll of the resultant mechanical properties.

2.2 Nanostructured bainitic steels

Nanostructured bainitic steel is achieved by suppressing the bainite transformation to temperatures lower than those generally associated with bainite while at the same time avoiding martensitic transformation. Indeed, the bainite transformation has been achieved for temperatures as low as 125 °C [66–68]. The purpose of course is to refine the scale of the structure, leading to bainitic ferrite plates with widths of the order of 50 nm, separated by films of retained austenite [66, 69–71]. These dimensions are an order of magnitude smaller than bainite in conventional steels.

The low transformation temperature is achieved by the addition of austenite stabilisers, such as carbon, manganese and nickel. The carbon is critical both to ensure retained austenite and to suppress the transformation temperature while avoiding the merging of the B_S and M_S temperatures [66]. The carbon typically is around 1 wt% [66, 69, 72]. This suppresses martensitic transformation to below 200 °C, permitting the bainite to form at temperatures are not accessible.

In spite of the fact that there are numerous combinations of alloying additions that might be used to form nanostructured bainitic steel, the alloys described in the literature mostly contain 0.8–1 wt% carbon, 1.5–2 wt% silicon, and at least one of: up to 1.5 wt% chromium, up to 2.5 wt% manganese, up to 4 wt% nickel, and up to 0.2 wt% vanadium. There are some outside these parameters [66, 69, 73–77]; a comprehensive listing is available in [1].

2.2.1 Alloy design

It has been shown that the structure can be refined by decreasing the transformation temperature [78]. It is thus important to find the minimum temperature at which bainite can form, while avoiding martensitic transformation. The theory determining B_S and M_S temperatures is well-established [79–82]. Fig. 2.7a illustrates how the B_S and M_S temperatures vary as a function of the carbon concentration. There is in principle no minimum B_S temperature but the rate at which bainite

forms diminishes drastically at low temperatures, Fig. 2.7b. To generate bainite at room temperature may require many years. For useful purposes, a transformation time of many days is reasonable, equivalent to a carbon concentration of around 1 wt%, in which case bainite can be created at a temperature as low as 125 °C, which is so low that the diffusion distance of an iron atoms is an unfathomable 10^{-17} m over the time scale of the experiment.

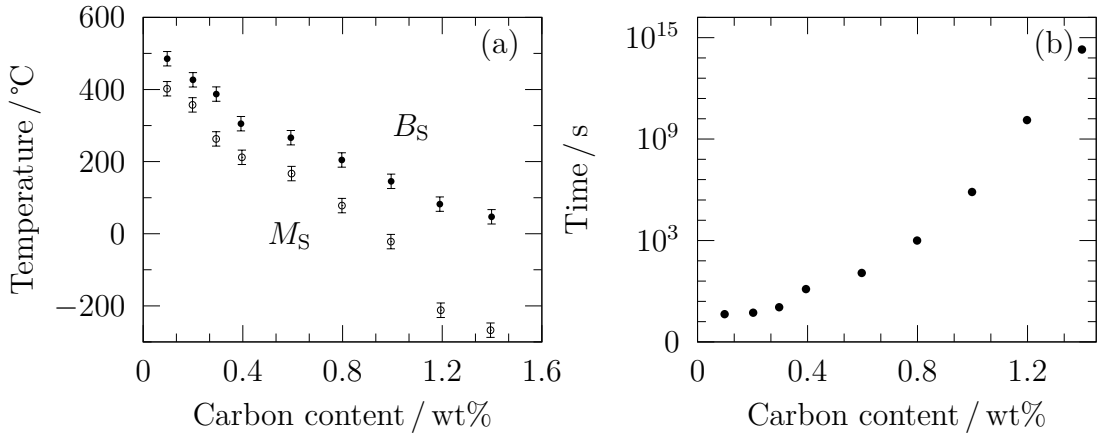


Figure 2.7: (a) Shows the determined transformation start temperature in Fe-2Si-3Mn-C wt%, steel as a component of the carbon concentration. (b) The determined time necessary to initiate bainite at the start temperature [80].

A steel based on this premise was invented and documented [83–85]. Fig. 2.8 demonstrates the structure achieved after isothermal transformation at 200 °C and 250 °C, respectively, consisting of platelets of bainitic ferrite in the range of 20-40 nm thick, with interceding regions of austenite. The retained austenite is critical because during deformation–induced transformation it increases the work-hardening rate, thus preventing an early plastic instability, the lack of which has compromised many nanocrystalline alloy concepts in the past [86, 87].

Following the initial work, numerous varieties of the alloy have been characterised; the structure has been described down to atomic resolution. Consistent with the mechanism of displacive transformation leads to a change in crystal structure by deformation, with no rearrangement of substitutional atoms on the smallest pos-

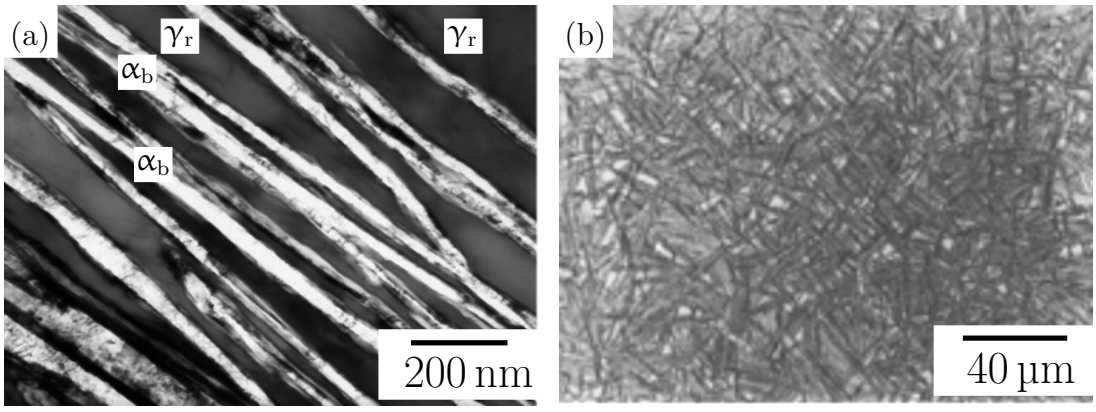


Figure 2.8: (a) Transformation at 200 °C over 5 days to obtain bainite; the image shows electron micrograph. (b) Optical micrograph of bainite attained at 250 °C for 15 days [84, 85].

sible scale [88, 89]. Subject to transformation conditions, the carbon content in the retained austenite has been seen as high as 5-7 at.% [90]. Low transformation temperature leads not only to a larger volume fraction of bainitic ferrite, but also results in high strength by incorporating a large number of defects (i.e., interfaces and dislocations) into the structure.

The first transformations of high-carbon, high-silicon steels at low temperatures that could lead to nanoscale microstructures and highly strong steels were reported by Caballero and co-workers [83]. The finding led studies of the design of mixed of bainite and martensite structures to be produced in medium carbon steels during continuous cooling [91, 92]. The steels mainly have a bainitic structure consisting of fine plates of upper bainite, which are separated by stable austenite films. Thermodynamics was used to then design alloys to maximize the volume fraction of fine structure of bainite and to ensure that the blocky retained austenite is avoided, by shifting the T_0 curve to a higher content of carbon and reducing the average carbon content of the steel [91]. The properties, are in some cases shown to be better than those of quenched and tempered martensitic steels, TRIP-assisted steels and dual-phase steels as shown in Fig. 2.9.

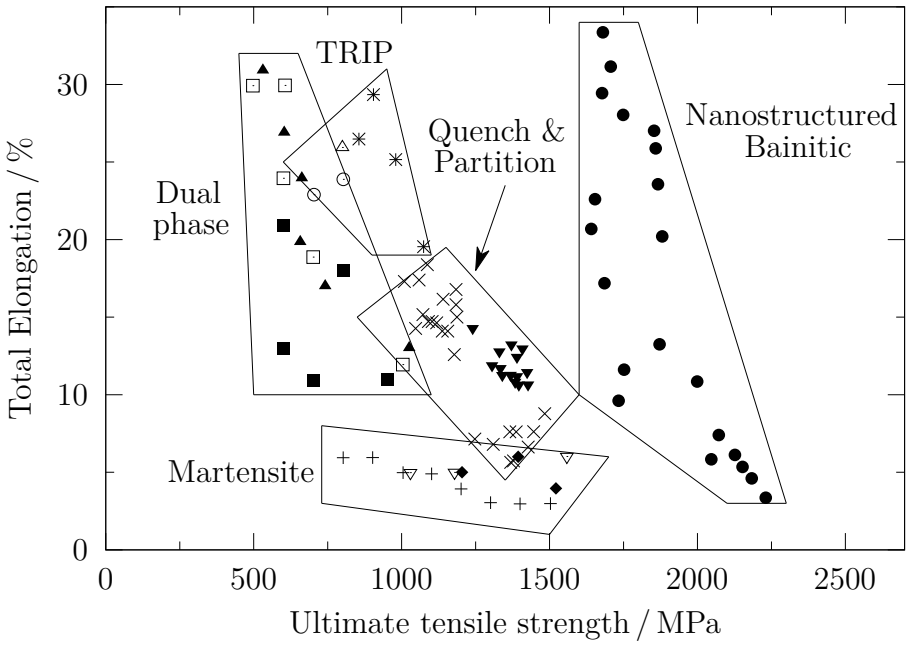


Figure 2.9: Mechanical properties of low–temperature bainite compared against other types of steel. Adapted from [93]; original data from [94, 95].

The rate of transformation is sufficiently sluggish to guarantee that a substantial component transforms consistently into a nanostructure, as demonstrated in Fig. 2.10. Isothermal transformation experiments were performed at 200, 250, 300 and 325 °C, using hardness and optical microscopy to monitor transformation progress, as well as using X-ray diffraction to measure transformed volume fractions. It was possible to produce bainitic microstructures with a hardness of around 600 HV by transforming them at temperatures of around 250 °C. These structures consist of $\approx$ 60-70% bainitic ferrite, with a plate size of $\approx$ 40 nm separated by thin retained austenite films [83]. On the TTT diagram, the bainite transformation had a distinct C–Curve with a well-defined B_S temperature, as shown in Fig. 2.10.

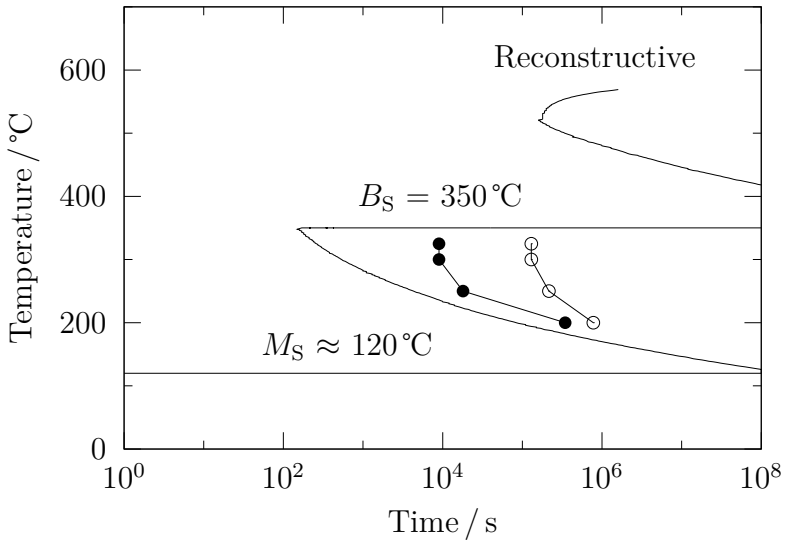


Figure 2.10: TTT diagram shows the start of isothermal reaction. The filled points signify the start of the bainite reaction where the other circles represent the end of the reaction [83–85].

Davenport and Bain had earlier recorded transformation to mostly bainitic microstructures at comparable temperatures [56], as low as 140 ℃. Although not recorded, it is likely that these microstructures contained large cementite particles compared to the Caballero and co-workers steels, owing to the reduced silicon content. However, it may be remarkable that Davenport and Bain noticed that in some steels austenite could be retained, after transformation at low temperatures (140 ℃). However, only trace amounts of austenite were noted after martensite transformation. Transformation at this temperature led in a hardness of (≈800 HV) with 20-25% retained austenite and (≈750 HV) at 180 ℃.

The bainite attained by transformation at a very low temperature is the strongest ever realised 2.5 GPa [80, 82] and has a significant toughness 30-40 MPa $m^{1/2}$ [70] and yet does not required rapid cooling or mechanical processing. Because of the slow transformation, the steel does not have quenching–induced stresses; it is extremely cheap to create and has consistent properties along all directions. Some of the properties like strength, ductility and toughness are shown in Fig. 2.11.

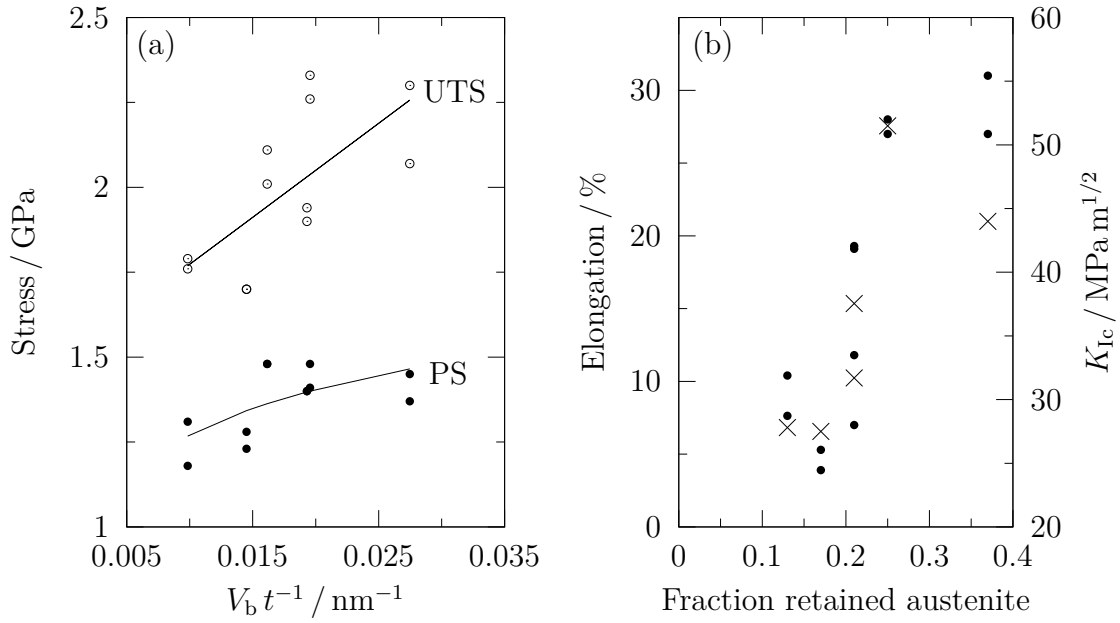


Figure 2.11: Shows some of the mechanical properties of super-bainite steel. (a) Ultimate tensile strength (UTS) and 0.2% proof strength (PS) as a function of the volume fraction of bainitic ferrite (V_b) divided by the thickness of the platelet (t). (b) Toughness K_{Ic} illustrated by crosses while ductility represented as percentage elongation by points [96] after [97].

2.2.2 Thermal stability of nanostructured bainitic steels

The bainite reaction does not lead to thermodynamic equilibrium, but occurs at low temperatures because of restricted atomic mobility. With sufficient time, a bainitic structure subjected to high temperatures may undergo changes that compromise properties, particularly carbide precipitation from the carbon-enriched austenite [98, 99]. Once carbides start to form, carbon will leave solid solution. Depending on the steel composition, this can occur at the tempering temperature or during the course of the bainite transformation. In the absence of graphite, cementite generally represents the most stable carbide in equilibrium with ferrite. Other transition carbides that precipitate before cementite can be identified under certain circumstances as they are easier to nucleate [100].

Carbides rich in substitutional solutes can also form during tempering, for example those containing chromium [101–103], molybdenum [104–106] and vanadium [101, 107, 108], if the tempering temperature where these solutes are able to diffuse [109, Table 1.4]. The substitutionally-alloyed carbides tend to be fine and therefore unlikely to fracture during deformation [99]. As the growth of these carbides requires the long-range diffusion of substitutional atoms, they grow extremely slowly. Saha Podder [110, Table 2.1] presents various products resulting from the tempering of martensitic steels.

2.3 Nanostructured bainite: some special effects

As already emphasised, retained austenite plays a vital role in controlling the ductility of strong bainite, because by undergoing deformation-induced martensitic transformation, it adds to the ability of the material to work harden. Ultra-fine grain structures otherwise undergo plastic instability immediately on yielding [111].

It is important therefore to delay the transformation of retained austenite to the late stages of deformation when significant damage accumulates in the steel. It

is at this point that the transformation effect can be most beneficial. It is useful therefore to examine further the transformation of austenite as a function of plastic strain.

Assuming that the change in the fraction of martensite ($\mathrm{d}V_V^{\alpha'}$) obtained for a given increment of plastic strain ($\mathrm{d}\varepsilon_\mathrm{p}$) should be proportional to the fraction of remaining austenite [112]:

$$\frac{\mathrm{d}V_V^{\alpha'}}{\mathrm{d}\epsilon} = k_\gamma V_V^\gamma, \tag{2.1}$$

where k_γ is a function of the steel composition and test temperature and V_V^γ is the fraction of austenite remaining untransformed. If the fraction of austenite at zero strain is $V_V^{\gamma\circ}$, then $V^{\alpha'} = V_V^{\gamma\circ} - V_V^\gamma$, and integration of Eq. 2.1 gives:

$$\ln\{V_V^{\gamma\circ}\} - \ln\{V_V^\gamma\} = k_\gamma \varepsilon_\mathrm{p}.$$

The form of this equation is illustrated in Fig. 2.12 and defines the behaviour of the austenite both as a function of the fraction of austenite, its thermodynamic stability via the parameter k_γ and plastic strain.

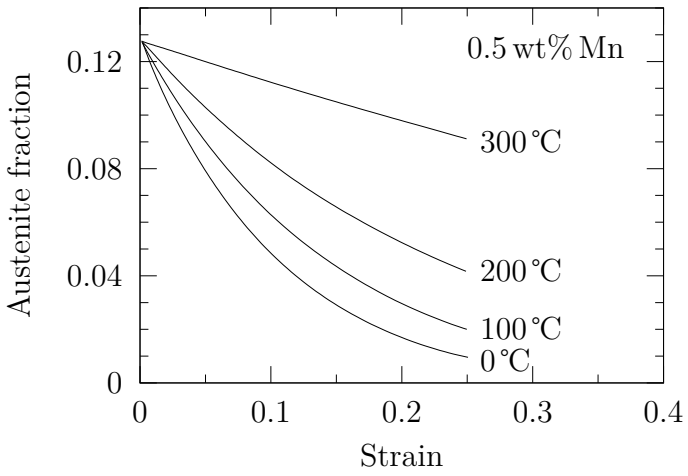


Figure 2.12: Martensitic transformation of retained austenite in a TRIP-assisted steel as a function of deformation temperature and plastic strain. After Sherif et al. [112].

It has been suggested that failure occurs when the austenite, which is the toughest of all the phases present, becomes geometrically isolated, i.e. it loses percolation [113]. The percolation threshold is when the austenite level has decreased to about 10% of the total microstructure. This of course may or may not be a complete explanation but is a useful working hypothesis for structures containing only α_b and γ. In industrial alloys, there may be for example, be an overwhelming role of non-metallic inclusions.

2.4 Steel with mixture of transformation products

Mixed microstructures consisting of bainite and martensite are generally the result of insufficient heat treatment or the use of steel with inadequate martensitic-hardenability. Early study proposed that bainite microstructure leads to a decrease in ductility, toughness and strength [114, 115]. As the bainite forms at lower transformation temperatures, the deficiency of properties becomes less severe and is associated to the difference in strength between martensite and bainite. As this difference decreases, so does the deterioration in properties [115]. Tempering homogenises the strength so that bainite has less influence on the overall properties in a tempered martensite microstructure [115, 116]. For the same reason, the properties of a mixture of martensite and lower bainite are in terms of strength, better than that of upper bainite and martensite.

However, there are situations where mixed microstructures are particularly advantageous. Edwards [117] noted that lower bainite and martensite mixtures were tougher than either martensite or bainite after tempering. The toughness can increase as the phase that first forms (α_b or α') partitions the austenite geometrically, thus refining the size of the subsequently produced microstructure [118]. In a mixed of bainite and tempered martensite microstructures, the strength is found to go through a maximum as a function of the martensite fraction Fig. 2.13. As

the amount of bainite increases, so does the carbon concentration of the austenite; therefore, the strength of any martensite that forms subsequently also increases resulting in the peak.

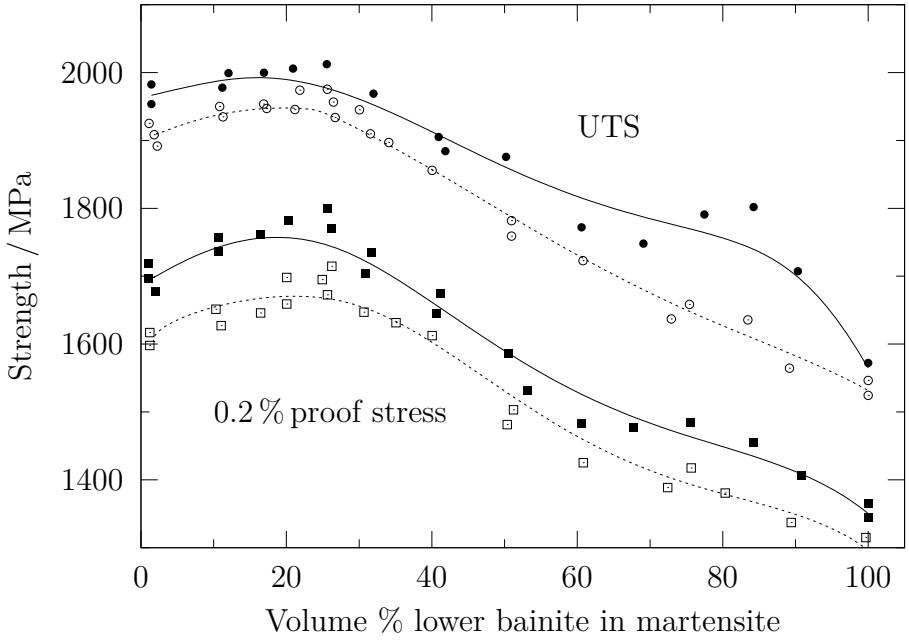


Figure 2.13: Comparison of calculations against experimental data of the mechanical properties as a function of the volume fraction of lower bainite in a mixed, tempered microstructure of lower bainite and martensite. The continuous lines represent tests done at 203 K and the dashed line for measurements at 287 k. After Tomita and Okabayashi [119].

2.5 Summary

It is obvious that greater levels of carbon cause a deterioration of ductility, mainly due to void nucleating tendency of cementite particles. The existence in the microstructure of large regions of untempered martensite also is detrimental, though finer retained austenite is always desirable.

The transformation of high-carbon, high-silicon steels leads to a carbide free mixture of bainitic ferrite and austenite. Low transformation temperature results in high strength due partitioning to the very fine scale of the bainitic ferrite plates. The hardness is then insensitive to tempering compared to similar martensitic steels that depend mainly on carbon in solution to deliver strengthening. The very high strengths attained do not require large deformations or rapid cooling, so large parts of material can be transformed into this nanostructure.

There already are fast transforming alloys. The limited work published on a nanostructure bainite that is stable at high temperatures has not been reviewed here, but is described in the context of the research chapters that follow in order to avoid repetition.

Chapter 3

Experimental Methods

This section gives an overview of the common experimental techniques used in this work, except where the use of a technique is exclusive to a particular chapter.

3.1 Materials

Two bulk nanocrystalline bainitic steels have recently been developed in which the austenite is exceptionally resistant to thermal decomposition [120]. Both are designed to generate a mixed nanostructure of bainitic ferrite plates embedded in a matrix of carbon - enriched austenite. The alloys have enough carbon to ensure the low transformation temperatures necessary to achieve the nanostructure. However, Alloy A, has more than the usual amount of silicon (1.5 Si wt%) added to suppress cementite precipitation, so that any carbon partitioned from the supersaturated bainitic ferrite ends up in the residual austenite that is then retained to further enhance the toughness. From elementary hardenability considerations, the reduced manganese concentration avoids the need for long transformation. Alloy B has enough carbon and nickel to guarantee a low transformation temperature which is conducive to the production of nanostructured bainite [70]. It also is rich in cobalt and aluminium, both of which accelerate the bainite transformation [121]. The chemical compositions of the alloys studied are listed in Table 3.1.

Alloy	C	Si	Ni	Al	Mo	Mn	Co	Cr
A	0.72	3.87	3.40	1.39	0.21	0.02	<0.01	<0.01
B	0.45	0.03	13.20	2.63	0.30	0.15	3.99	<.005

Table 3.1: Chemical compositions, wt%.

3.2 Sample preparation

Samples mounted in conductive bakelite were ground using silicon carbide emery papers (600 - grade to 2500 - grade), followed by polishing with 6 µm to 1 µm diamond paste. The polishing is finished with 0.25 µm diamond paste. The samples were cleaned with ethanol and rinsed between grinding stages, and using an optical microscope the surface quality was assessed between all stages. Etching was performed with a 2 % nitric acid, 98 % methanol mixture. The mounted sections were used for optical analysis, scanning electron microscopy and hardness testing while the unmounted sections were similarly prepared for orientation imaging and X - ray analysis but without etching, followed by electropolished using 5 % perchloric acid, 25 % glycerol and 70 % ethanol at 10 °C and 11 V for 8 min. For transmission electron microscope, samples were cut using spark erosion techniques as 3 mm diameter discs from the sample concerned, then thinned down to ≈ 50 µm at 8.5 – 10°, with final electropolishing into a thin foil set to a voltage of 22 – 25 V using the above electrolyte.

3.3 Microstructural observations

3.3.1 Optical microscopy

Optical microscopy, with magnification in the range 50 – 500 X, was performed using a Leica Microsystems DM2500M upright light microscope with attached DFC295 camera for recording the micrographs. Leica Application Suite software,

GIMP and ImageJ were used to make minor digital enhancements (e.g., brightness and contrast, adjustments cropping, addition of scale bars).

3.3.2 Scanning electron microscopy

Scanning electron microscopy (SEM) was conducted on a FEI Nova NanoSEM, fitted with a Everhart - Thornley Detector operating at 15 kV and a working distance of 5 mm was used for microstructural investigation as well as to study the fracture surface morphology of the mechanically tested (tensile, fracture toughness and impact test) samples in secondary electron mode. Energy-dispersive X-ray (EDX) analysis was used to characterise the aluminium nitride precipitates in the back-scatter electron mode.

3.3.3 Electron back-scatter diffraction

Electron back-scatter diffraction (EBSD) was carried out using a ZEISS GeminiSEM 300 field emission gun scanning electron microscope at a magnification of $\times$1500 with a step size of 0.06 µm, a voltage of 15 kV and a working distance of 15 mm were used. Data analysis was carried out using "Channel 5" software.

3.3.4 Focused ion-beam milling of samples

A dual-beam FEI Helios Nanolab equipped with a FEG-SEM and a focused ion-beam (FIB) system was used to cut out samples from explicit regions of a specimens for further examinations in the transmission electron microscopy.

3.3.5 Transmission electron microscopy

A FEI Tecnai Osiris operated at 200 keV, fitted with an energy dispersive spectroscopy (EDS) detector, was used for scanning transmission microscopy (STEM) in bright field, dark field, high-angle annular dark field (HAADF) imaging and selected area diffraction (SAD).

3.3.6 X-ray diffraction

X-ray diffraction analysis (Bruker D8 DaVinci, Cu Kα radiation) was used to determine phase fractions. The detector was scanned through a range of $35° < 2\theta < 130°$, a step size 0.050°, dwell time of 0.5 s, 2.5° primary slit, a divergence slit 8 mm wide and 18 mm antiscatter slit at 40 kV and 40 mA and a rotational speed was $30° \, \text{min}^{-1}$. HighScore Plus analysis software was used to identify peak positions and peak fitting. The X-ray spectra were subjected to Rietveld refinement [122]. The weighted profile R-factor (R_{wp}) and goodness-of-fit were used to assess the quality of fitting, which also was checked graphically [123]. The Dyson and Holmes [124] relationship between the austenite composition and its lattice parameter was used to estimate its carbon content.

3.4 Metallurgical experiments

3.4.1 Thermodynamic calculations

The National Physical Laboratory's Metallurgical and Thermodynamic Data Bank (MTDATA) program written by the National Physical Laboratory, Teddington, U.K. [125] with TCFE version 1.0 database (equivalent to version 5.0 for *ThermoCalc*) [126], were used to conduct thermodynamic software simulation for both alloys. Various thermodynamic quantities can be predicted, including Gibbs energy of phases or mixture of phases, chemical potential, equilibrium compositions

and fractions of phases in material of a system defined by the user. Composition and temperature can both be specified by the user and using a variance of one quantity over a certain range can be used to observe its effect on the thermodynamic quantities in question. The program allows constraints to be specified and allows a selection of phases, such as preequilibrium of specific components to reflect particular physical processes. *ThermoCalc* software with the thermodynamic database TCFE8 was also used to perform thermodynamic calculations [127, 128]. *MatCalc* software with the Fe database version 5.62 was also used for all *MatCalc* calculations.

3.4.2 Dilatometry

Dilatometry is an important tool in the analysis of phase transformations. Both temperature and phase changes as well as the precipitation or the partition of alloying elements and their compounds all result into a change in the lattice parameter of iron. These effects prompt a macroscopic visible volume change in the sample.

The TA Instruments DIL805A/D dilatometer, was used with a 4 mm diameter and 10 mm length samples, machined from the hot - rolled plate. Samples with 5 mm diameter and 10 mm length, were used in the deformation mode to control the deformation strain, and strain rate. Any surface oxide was removed using silicon carbide paper. The samples were then heated under vacuum and the temperature was recorded using a 0.1 mm S - type thermocouple spot - welded onto the sample surface. Temperature in the deformation mode was calibrated using 0.2 mm S - type thermocouple. Cooling was achieved using argon gas. Temperature, load, strain, diameter and change in length were monitored simultaneously.

3.4.3 MTTTData

MTTT Data is a FORTRAN program which utilises MTData to generate thermodynamic data which then are used to find M_S, B_S, W_s and kinetic data. The National Physical Laboratory's "PLUS" database, version 3.02 is used [129]. MTTT-Data was used by Yang and Bhadeshia [130] to aid the design process of low carbon bulk nanostructured bainitic steels. Thermodynamic data are retrieved from a database to facilitate kinetic predictions [131].

3.5 Mechanical testing

3.5.1 Hardness measurement

Vickers hardness was measured with a 10 kg load on an ATM Qness 30+ automatic indenter. This load ensures that the hardness value is independent both of the size of the indenter and the test force used (for loads > 0.2 kg) [132]. The test is suitable for virtually all metallic materials due to a wide range of test forces being available. A pyramidal indenter is pressed into the surface of the material with a constant test force. A hardness value is calculated using diagonal lengths of the square indent made which are optically and determined and converted into the formula:

$$HV \simeq \frac{0.1891F}{d^2} \tag{3.1}$$

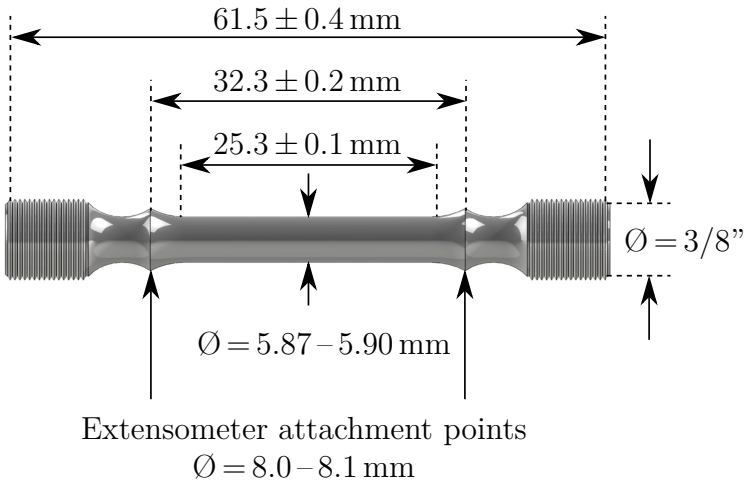
where F is the test load in N and d is the diagonal measurement in mm. As with all indenter hardness tests, work hardening occurs in the immediate area around an indentation thus it is desirable to maintain a suitable distance between indents when carrying out multiple measurements on a sample. A distance of at least $2.5\,d$ is advised.

An average of at least ten indents were measured in each sample. The standard

deviation ($STDEV$) of the measurement was taken to calculate the statistical standard error ($STDEV/\sqrt{N}$), where, N is the total number of indentations made.

3.5.2 Tensile tests

Tensile tests were performed in accordance with ASTM E8/E8M - 15a and E21 - 09, using industry-standard test pieces with the dimensions illustrated in Fig. 3.1. Tests were carried out at ambient temperature, 200 ℃ and 450 ℃. A constant crosshead speed of $0.002\,\mathrm{mm\,min^{-1}}$ was maintained with samples instrumented with an extensometer that allowed the load-displacement data to be tracked.



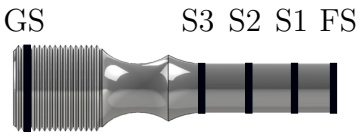


Figure 3.1: Sample geometry for tensile testing. All testpieces were machined from the centre of each blank after heat treatment. The lower diagram shows the shaded regions from which samples were extracted for X - ray diffraction analysis, where “FS” represents the fracture surface and “GS” is the undeformed area.

3.5.3 Toughness tests

Toughness was measured using crack-tip opening displacement (CTOD) fracture toughness (K_{IC}) and Charpy impact tests. Both tests were performed in accordance with ASTM E399-09 and ASTM E23-12c respectively. Test piece geometries are shown in Figs. 3.2 and 3.3.

For CTOD test, following Dieter [133], the samples dimensions were: $a = 10.5\,\mathrm{mm}$, $W = 26$ mm and $B = 13$ mm, (Fig. 3.2 and Eq. 3.2). At the point when a pre-cracked sample is tested, load and crack opening displacement are essential. Load was applied with a ratio of $\mathrm{R} = \sigma_{\mathrm{min}}/\sigma_{\mathrm{max}} = 0.1$, where σ_{min} and σ_{max} are the minimum and maximum stress respectively. The load applied at failure is determine by the 5% secant method which was believed to have occurred when the crack - tip opening displacement is equal to 95% of the initial elastic region of the tangent line.

To form a substantial measurement of K_{IC}, conditions must be fulfilled as described in the standard ASTM E399-12E3, to ensure plane strain at the crack tip during failure. In the event that these conditions are not met, the measured toughness is assigned K_{Q}, although K_{Q} is not a material property, it allows comparison between tests. The expression for K_{Q} is given in Eq. (3.2), where P_{Q} is the load applied at failure and a, W and B are sample dimensions, as shown in Fig. 3.2.

$$\begin{aligned} K_{\mathrm{Q}} = \frac{P_{\mathrm{Q}}}{BW^{1/2}} \Bigg[& 29.6 \left(\frac{a}{W}\right)^{1/2} - 185.8 \left(\frac{a}{W}\right)^{3/2} \\ & + 655.7 \left(\frac{a}{W}\right)^{5/2} - 1017.0 \left(\frac{a}{W}\right)^{7/2} \\ & + 638.9 \left(\frac{a}{W}\right)^{9/2} \Bigg] \,\mathrm{MPa\,m^{1/2}} \end{aligned} \tag{3.2}$$

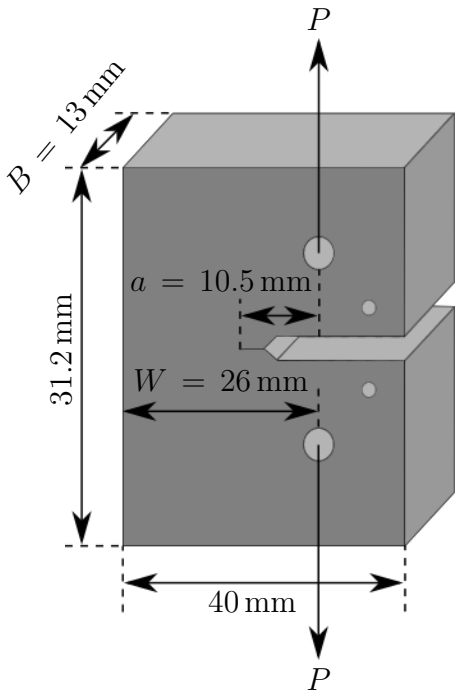


Figure 3.2: Sample geometry for fracture toughness (compact tension) testing. Where P is the load and a, B and W refer to the measurements used in (Eq. 3.2).

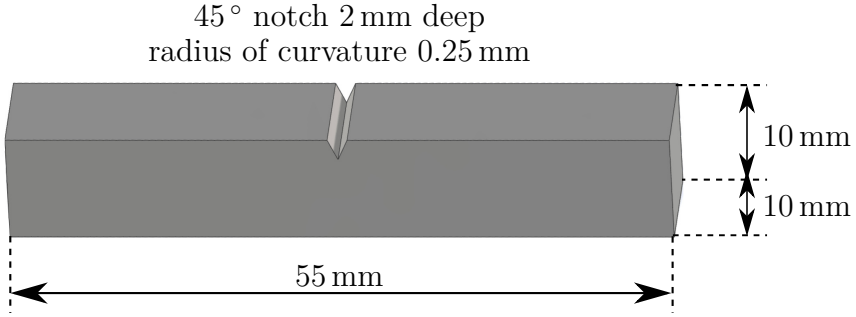


Figure 3.3: Sample geometry for Charpy impact testing performed on as-transformed and tempered conditions.

Chapter 4

Phase transformations

Experiments were initiated to assess the transformation characteristics of each alloy. Introductory investigations were directed to evaluate the cooling method required to form nanostructured bainitic steels and comprehensive dilatometric experiments were performed to study the transformation kinetics.

4.1 Initial microstructures

Alloy A in its as-received state has a microstructure that is a mixture of allotriomorphic ferrite and pearlite (Fig. 4.1a), with a Vickers hardness of 461 ± 3 HV10.

The as-received microstructure of Alloy B is martensitic (Fig. 4.1b) with a hardness 600 ± 5 HV10. EDX for five points showed that the bright areas were slightly enriched in nickel (table 4.1), compared to the darker regions most likely formed first during casting, rejecting solute into the rest of the melt.

4.2 Initial experiments

Thermodynamic modelling using MTTTData [125, 129, 134] indicated that the reconstructive transformations can be avoided in Alloy A if cooled to $\approx 600\,^{\circ}\mathrm{C}$

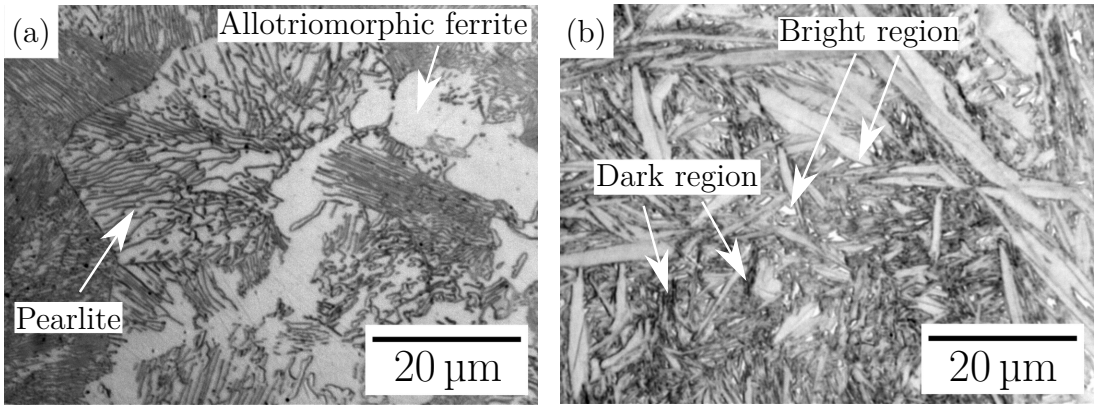


Figure 4.1: Optical micrographs in as - received condition (a) Alloy A, the bright areas are allotriomorphic ferrite, which formed first, followed by pearlite. (b) Alloy B, the structure is martensitic but with some retained austenite.

	Al	Co	Ni
Bulk	2.63	3.99	13.20
Bright	2.71 ± 0.15	4.60 ± 0.16	13.5 ± 0.4
Dark	2.40 ± 0.15	4.67 ± 0.15	11.7 ± 0.4

Table 4.1: Compositions in wt% of bright and dark regions of Alloy B in the as - received condition, observed by optical microscopy.

in roughly thirty minutes (Fig. 4.2a). This shows the high hardenability which is necessary in the production of large components. Similar calculation apply to Alloy B, Fig. 4.2b.

However, as Alloy B is richly alloyed, MTTTData was not be able to predict a practical isothermal transformation time, instead it shows that the transformation should take a long period of time as shown in Fig. 4.2b. This has been proven experimentally incorrect as shown in section 4.5.2. It should be pointed out that MTTTData was made based on a low - alloy steel [131]. Although in a different scenario MTTTData could be used to predict isothermal transformation time in nickel alloys with less than 5.5 wt% [135]. It is to be noted that the thermodynamic calculations in this work take into account cobalt, which was omitted in previous work [120].

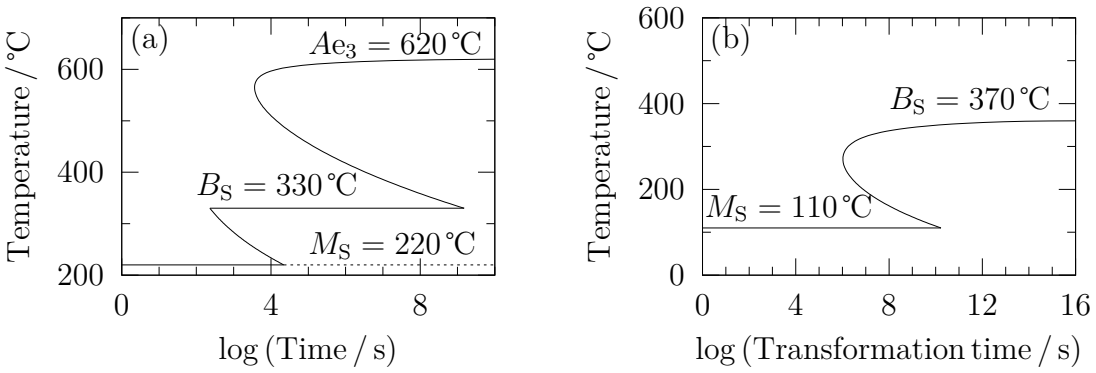


Figure 4.2: TTT curve calculated using MTTTData [125, 129, 134], for the composition of as-received conditions. The calculations predict that bainite will form in the temperature range of (a) 220 °C – 330 °C Alloy A, (b) 110 °C – 370 °C Alloy B, during isothermal transformation.

4.2.1 M_S temperature

A test wherein alloys A and B were austenitised and air cooled to ambient temperature revealed a change in gradient of the temperature profile at around 240 °C and 140 °C respectively (Fig. 4.3), corresponding to the martensitic transformation (Fig. 4.4), consistent with $M_S = 220\,℃$, Alloy A and $M_S = 110\,℃$, Alloy B using MTTTData.

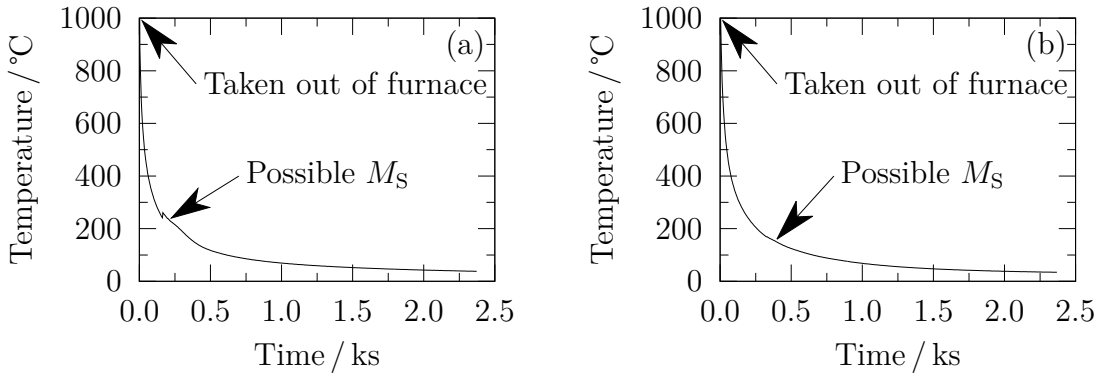


Figure 4.3: Temperature-time profiles for samples cooled in air after austenitisation, showing a change in gradient at (a) ≈ 240 °C Alloy A. (b) ≈ 140 °C Alloy B.

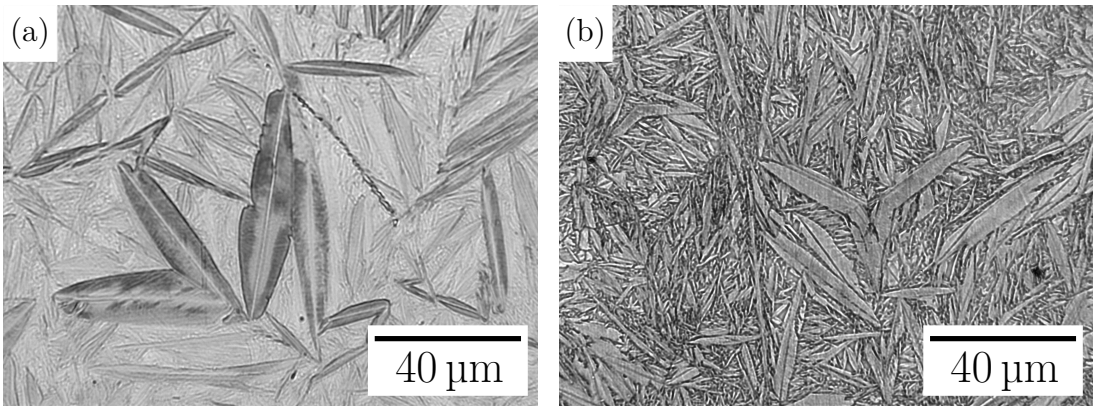


Figure 4.4: Martensitic microstructure formed in (a) Alloy A and (b) Alloy B, cooled in air from 1000 ℃ to ambient temperature.

4.2.2 Transformation kinetics of Alloy A

Samples were austenitised at 1000 ℃ for 30 min, freely cooled and transformed isothermally at 200 ℃, 260 ℃ and 300 ℃ for different times, giving the hardness values shown in Fig. 4.5. The hardness becomes steady after 1 d at all temperatures, suggesting that the subsequent microstructural changes are small. Lower transformation temperatures achieve higher hardness, consistent with the expected finer bainitic microstructure [78].

The samples transformed at 200 ℃ consisted of a mixture of bainite and large martensite plates. The martensite plates are a lot bigger than the bainite and have formed in typical self-accommodating zig-zag chains (Fig. 4.6a). Lots of martensite plates expand to the prior austenite grain boundaries, indicating that they formed first to be followed by bainite (Fig. 4.6b). Therefore M_S must be above 200 ℃ consistent with the recalescence detected during cooling (Figs. 4.3a and 4.4a). The samples transformed at 260 ℃ and 300 ℃, however, showed the expected combination of bainitic ferrite and retained austenite (Figs. 4.6c and 4.6d). These results will be explained later (Section 4.5).

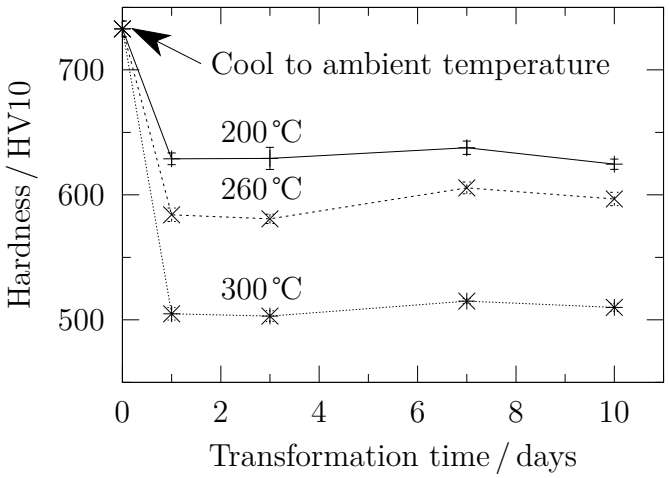


Figure 4.5: Hardness of Alloy A after austenitisation at 1000 °C for 30 min then transformed isothermally at 200 °C, 260 °C and 300 °C for different times as indicated.

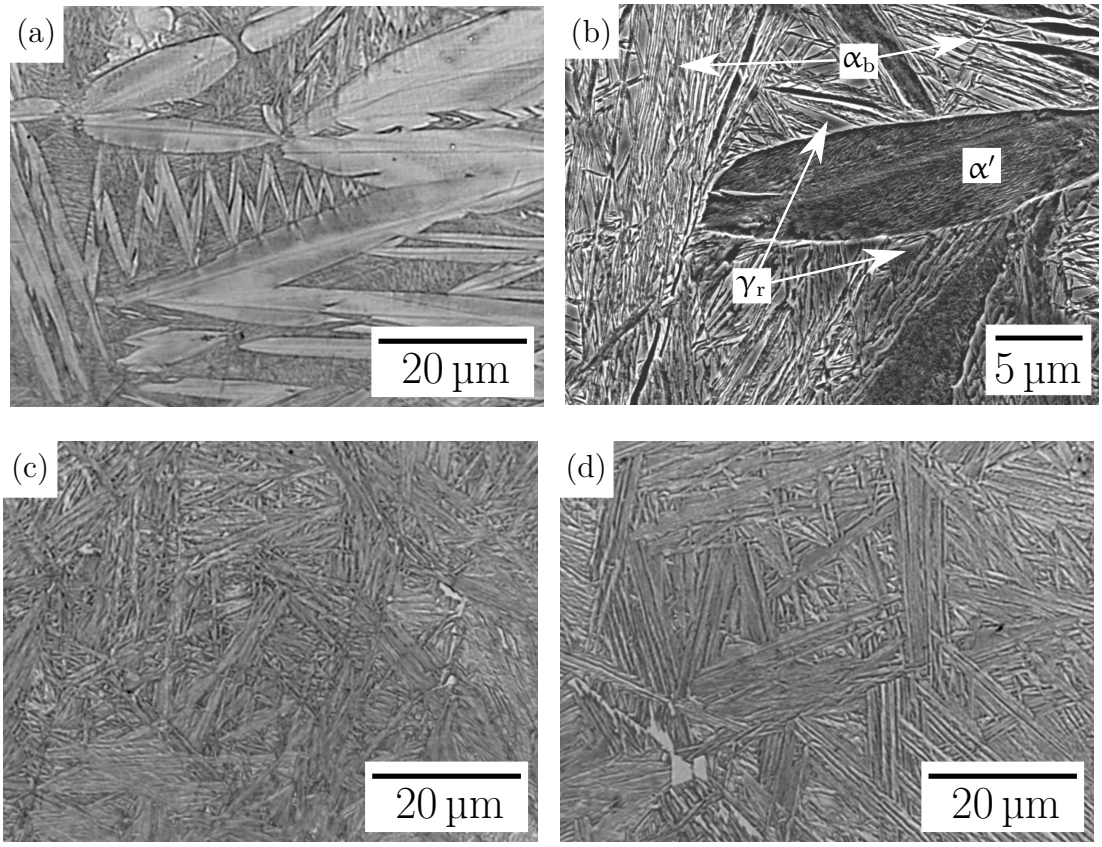


Figure 4.6: Optical microstructures in Alloy A after austenitisation at 1000 ℃ for 30 min and isothermally transformed for 24 h at (a) and (b) 200 ℃, bainite structure between large martensite plates. (c) 260 ℃ and (d) 300 ℃, both temperatures result in substantial quantities of bainite.

4.3 Dilatometric study of phase transformations

All dilatometry samples were similarly heated at 5 °C s^{-1} under vacuum to 1000 °C where they were held for 30 min. Samples then were either transformed isothermally or cooled continuously to ambient temperature, as detailed in table 4.2.

Alloy A							
Temperature / °C	800	750	700	650	600	550	500
Hold time / h	5.0	5.0	5.0	5.0	6.0	6.5	6.5
Temperature / °C	450	400	350	325	300	275	260
Hold time / h	12.0	12.0	12.0	12.0	12.0	12.0	12.0
Temperature / °C	30	30	30	30			
Cooling rate / °C s^{-1}	20	10	5	2			
Alloy B							
Temperature / °C	600	450	350	300	250		
Hold time / h	10.0	18	20	20	145		
Temperature / °C	30	30					
Cooling rate / °C s^{-1}	10	5					

Table 4.2: Heat - treatment conditions applied in dilatometry experiments.

4.3.1 Experimental determination of martensite start temperature

Transformation temperatures were determined by slope changes in the dilatometric curve, using the offset method [136]. Alloy A was austenitised at 1000 °C for 30 min and then quenched to ambient temperature to determine, $M_S = 238$ °C for cooling at 5 °C s^{-1} (Fig. 4.7) to ensure the austenite is untransformed before reaching M_S. Cooling at lower rates (i.e. ≤ 2 °C s^{-1}) permits some allotriomorphic and

Widmanstätten ferrite to form (Fig. 4.8). Alloy B was similarly established to have a martensite - start temperature of 169 °C using the offset method (Fig. 4.9). Optical microscopy confirmed that no reconstructive transformations occurred and the structures were martensitic Fig. 4.10.

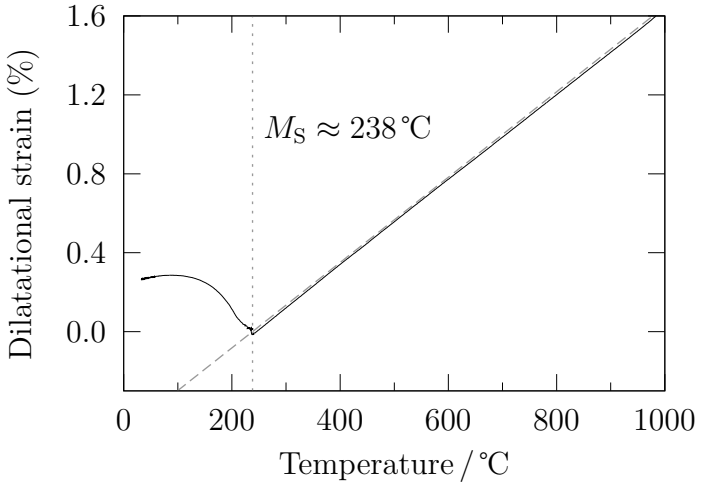


Figure 4.7: Dilatometric curve in Alloy A cooled at $5\,°C\,s^{-1}$, showing the M_S temperaturer according to the offset method with 1 vol.% transformation [136].

4.4 Transformation kinetics

Samples were heated in the dilatometer at $5\,°C\,s^{-1}$ to 1000 °C for 30 min, then cooled at $5\,°C\,s^{-1}$ to a variety of isothermal transformation temperatures (table 4.2), show that reconstructive transformations are avoided. Zero time is defined when the isothermal temperature is reached, and the onset of. Transformation was then taken to begin when the strain had increased by 1% of the net change during the isothermal hold (Fig. 4.11).

Transformations measured in Alloy A are rapid (Fig. 4.12): an order of magnitude shorter time than earlier bulk nanostructured bainitic steels [e.g., 69–71]. This is because of the absence of manganese, which decreases transformation driving force.

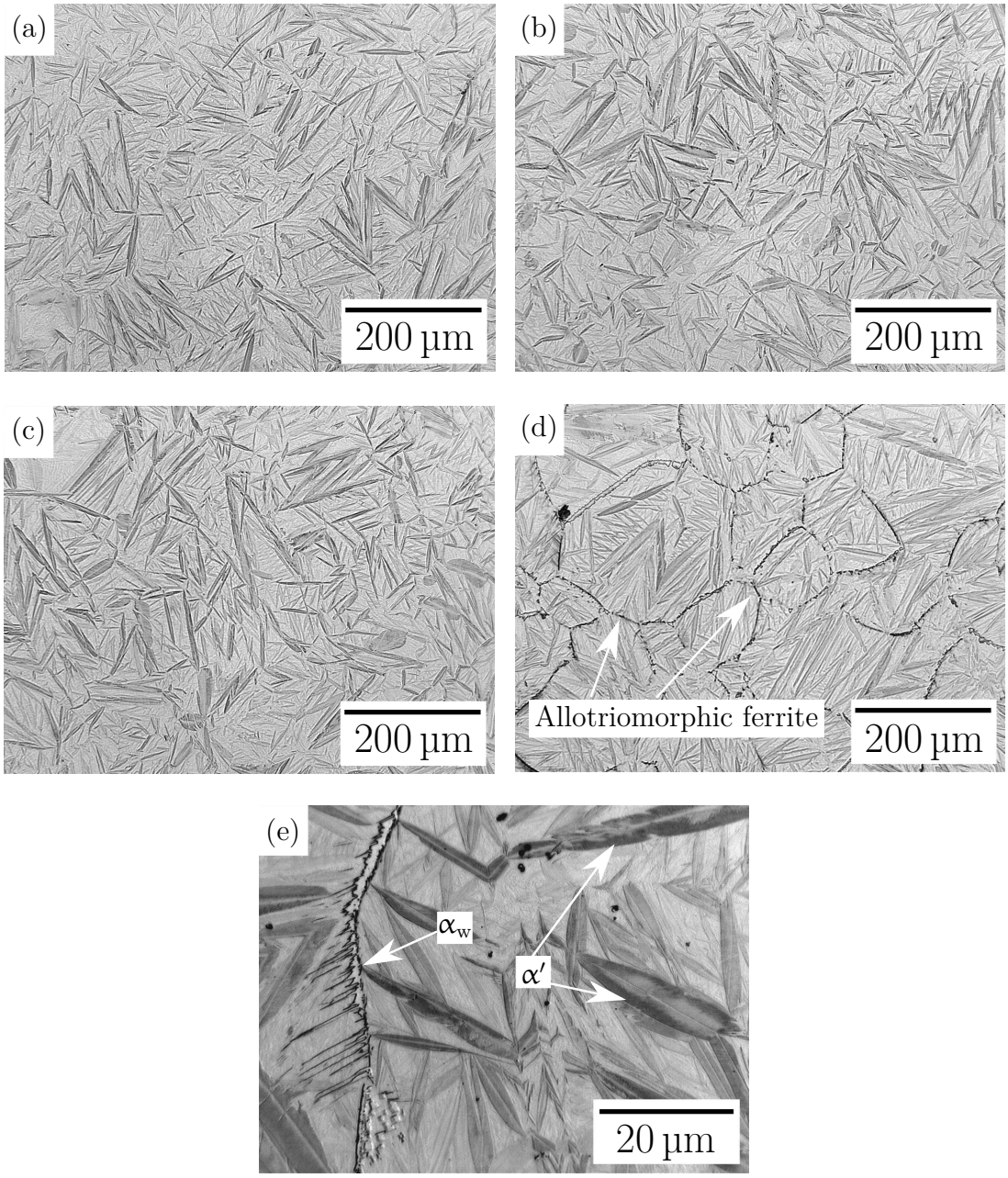


Figure 4.8: Optical micrographs of martensitic structure formed in Alloy A cooled to ambient temperature at (a) $20\,^{\circ}\mathrm{C\,s^{-1}}$, (b) $10\,^{\circ}\mathrm{C\,s^{-1}}$, (c) $5\,^{\circ}\mathrm{C\,s^{-1}}$ and (d) and (e) $2\,^{\circ}\mathrm{C\,s^{-1}}$. Cooling at $2\,^{\circ}\mathrm{C\,s^{-1}}$ results in a small quantity of allotriomorphic and Widmanstätten ferrite.

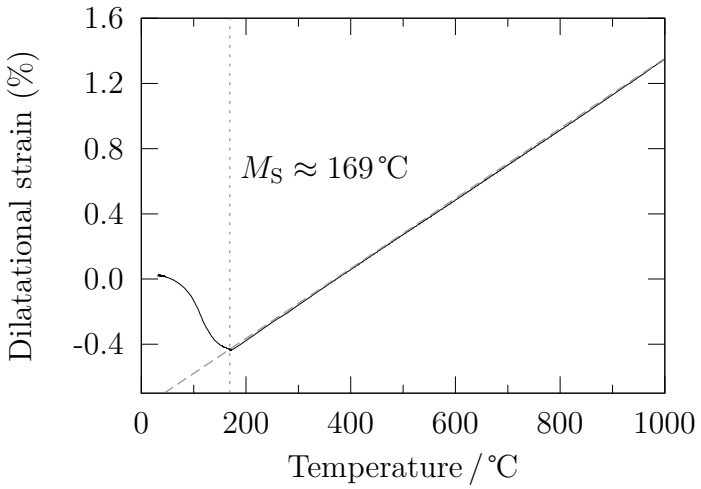


Figure 4.9: Dilatometric curve in Alloy B cooled at $5\,°C\,s^{-1}$, showing the M_S according to the offset method with 1 vol.% transformation [136].

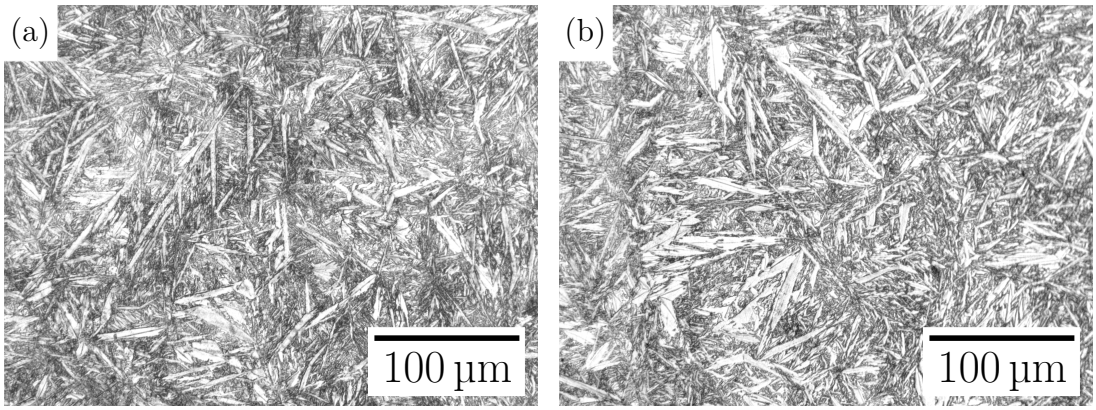


Figure 4.10: Optical micrographs of martensitic structure formed in Alloy B cooled to ambient temperature at (a) $10\,°C\,s^{-1}$, (b) $5\,°C\,s^{-1}$. Reconstructive transformations are avoided at both cooling rates.

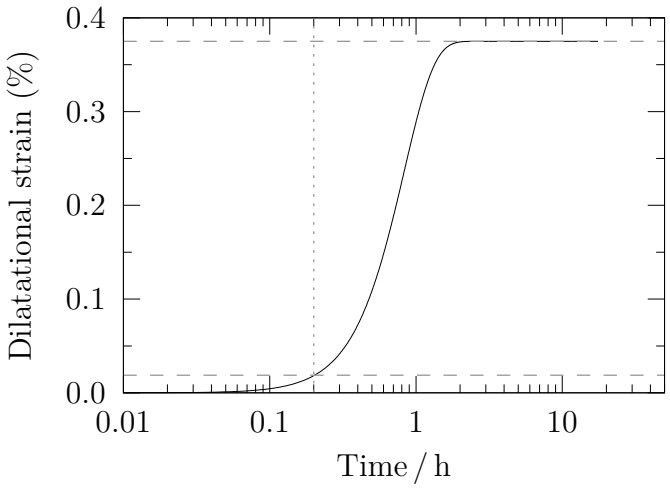


Figure 4.11: Alloy A transformed at 260 ℃. Horizontal lines are fitted to the "start" and "end" of the transformation.

Fig. 4.13 indicates that MTTTData predicts the correct bainite transformation times, Fig. 4.13a and few orders of magnitude longer than are measured in Alloy B, Fig. 4.13b.

Alloy B was discovered to have slower transformation kinetics than Alloy A, consistent with calculations (Fig. 4.2b cf. Fig. 4.12). Fewer isothermal transformation temperatures were considered, due to the slower kinetics.

4.5 Transformation microstructures

4.5.1 Alloy A

The transformation products in Alloy A of the experimental isothermal transformations were assessed dilatometrically, optical and scanning electron microscopy, hardness measurement Fig. 4.14 and X – ray diffractometry Fig. 4.15. The isothermal transformation temperatures will be studied individually in the following sections.

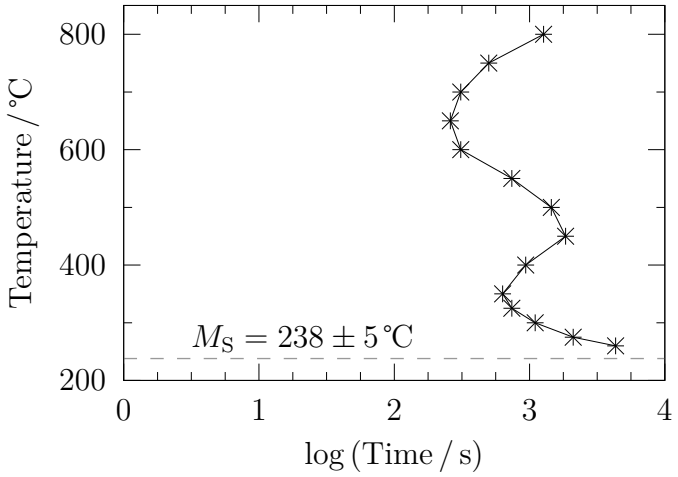


Figure 4.12: Measured TTT diagram for Alloy A based on the times required for the transformation at every temperature.

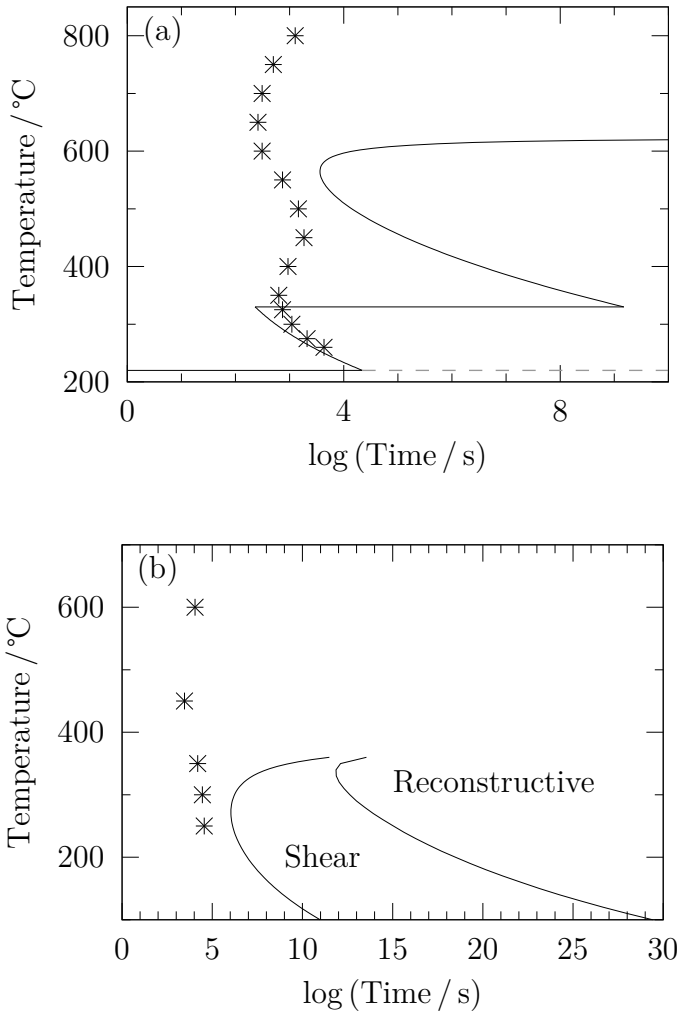


Figure 4.13: Comparison of experimental and measured transformation start times (points) and those calculated (lines) using MTTTData [125, 129, 134] for (a) Alloy A and (b) Alloy B.

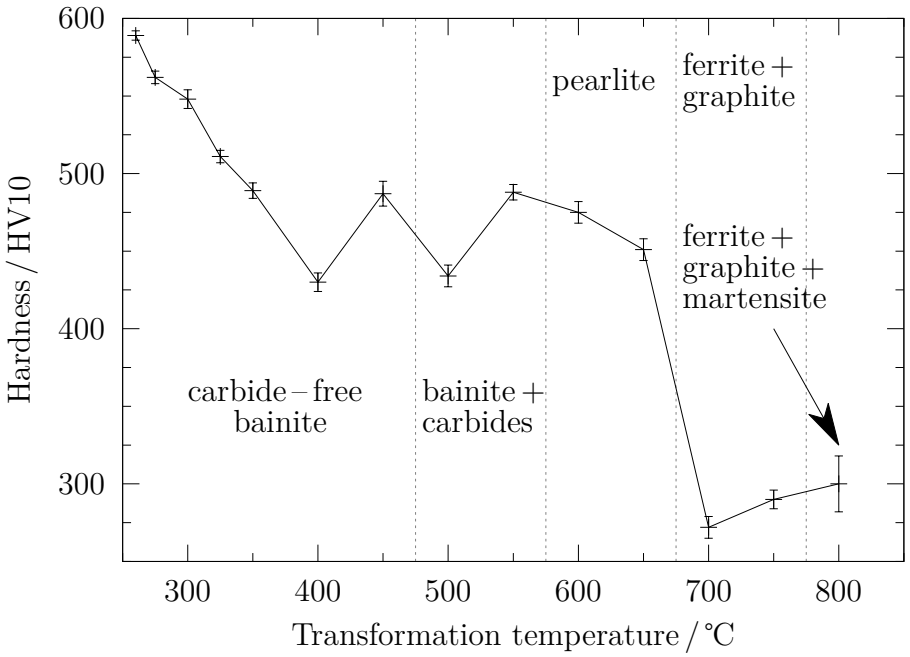


Figure 4.14: Hardness and evaluated microstructure for isothermally transformed Alloy A.

Temperature / ℃	Transformation Start Time / s	Microstructure	Hardness HV10
800	1270	Ferrite, graphite, martensite	300 ± 18
750	500	Ferrite, graphite	290 ± 6
700	310	Ferrite, graphite	272 ± 7
650	260	Ferrite, cementite	451 ± 7
600	310	Ferrite, cementite	475 ± 7
550	740	Bainite, cementite, ε	488 ± 5
500	1450	Bainite, austenite, cementite, ε	434 ± 7
450	1849	Bainite, austenite, cementite, ε	487 ± 8
400	936	Bainite, retained austenite	430 ± 6
350	632	Bainite, retained austenite	489 ± 5
325	740	Bainite, retained austenite	511 ± 4
300	1100	Bainite, retained austenite	548 ± 6
275	2100	Bainite, retained austenite	562 ± 4
260	4328	Bainite, retained austenite	589 ± 3
$2\,℃\,s^{-1}$	N/A	Martensite, allotriomorphic ferrite	717 ± 11
$5\,℃\,s^{-1}$	N/A	Martensite	721 ± 8
$10\,℃\,s^{-1}$	N/A	Martensite	737 ± 6
$20\,℃\,s^{-1}$	N/A	Martensite	753 ± 9

Table 4.3: Structures formed in Alloy A and associated hardness data.

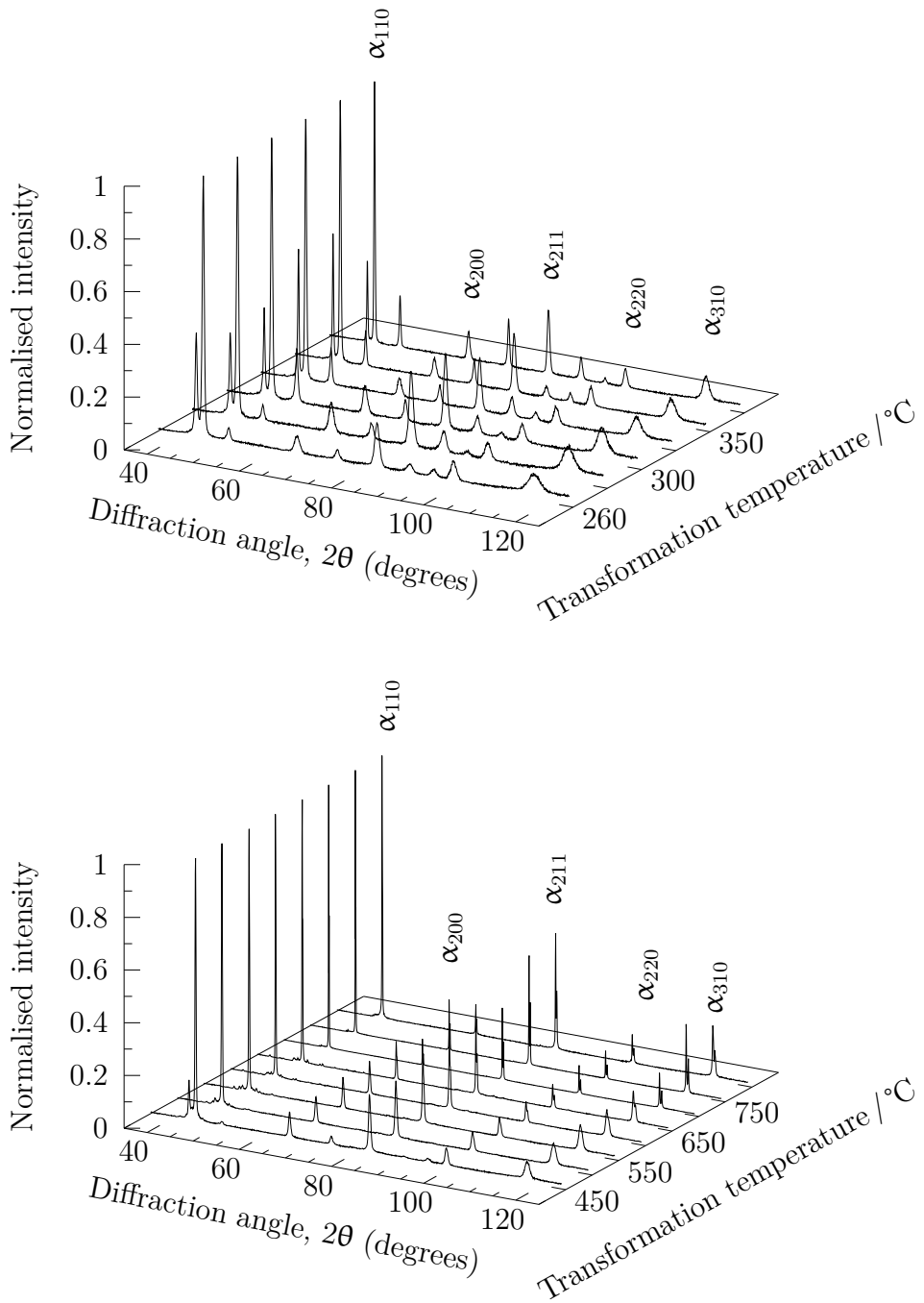


Figure 4.15: X - ray diffractograms of Alloy A after isothermal transformation. For the sake of clarity only ferrite peaks are labelled, other peaks may be seen in Fig. 4.26.

800 °C

The microstructure consisted of large ferrite grains containing irregular nodules of graphite together with some martensite, Fig. 4.16, due to the decomposition of the austenite which remains untransformed at 800 °C. Rietveld analysis (not including graphite) shows (79 ± 3) vol.% ferrite and (21 ± 5) vol.% martensite, consistent with equilibrium calculations of 75 vol.% ferrite, 22 vol.% austenite and 3 vol.% graphite. It was not possible to identify graphite using X-ray diffraction, however the microstructural appearance (Fig. 4.16a[1]) is typical of graphite seen in "black-heart cast-iron" (Fig. 4.17a). The graphite is a consequence of the well-known effect of a large silicon concentration in making cementite less stable. This is the basis for example of grey cast - iron as opposed to white cast-iron which has a low silicon concentration.

750 °C and 700 °C

The microstructures contained a mixture of ferrite and a small amount of graphite (Fig. 4.18a) following transformation at either 750 °C and 700 °C, alongside pearlite close to the edges of the sample (Figs. 4.18b and 4.18c). Thermodynamic calculations predict that cementite can form at temperatures up to 800 °C (Fig. 4.17b). Nonetheless when graphite is allowed to exist, the calculations suggest 3 vol.% [125, 137] graphite and cementite is excluded as a stable phase.

[1]The structure looks like that of blackheart cast-ion which requires many days to remove the cementite and converted into graphite however, this take a very short time to produce a similar structure, albeit for much lower carbon concentration.

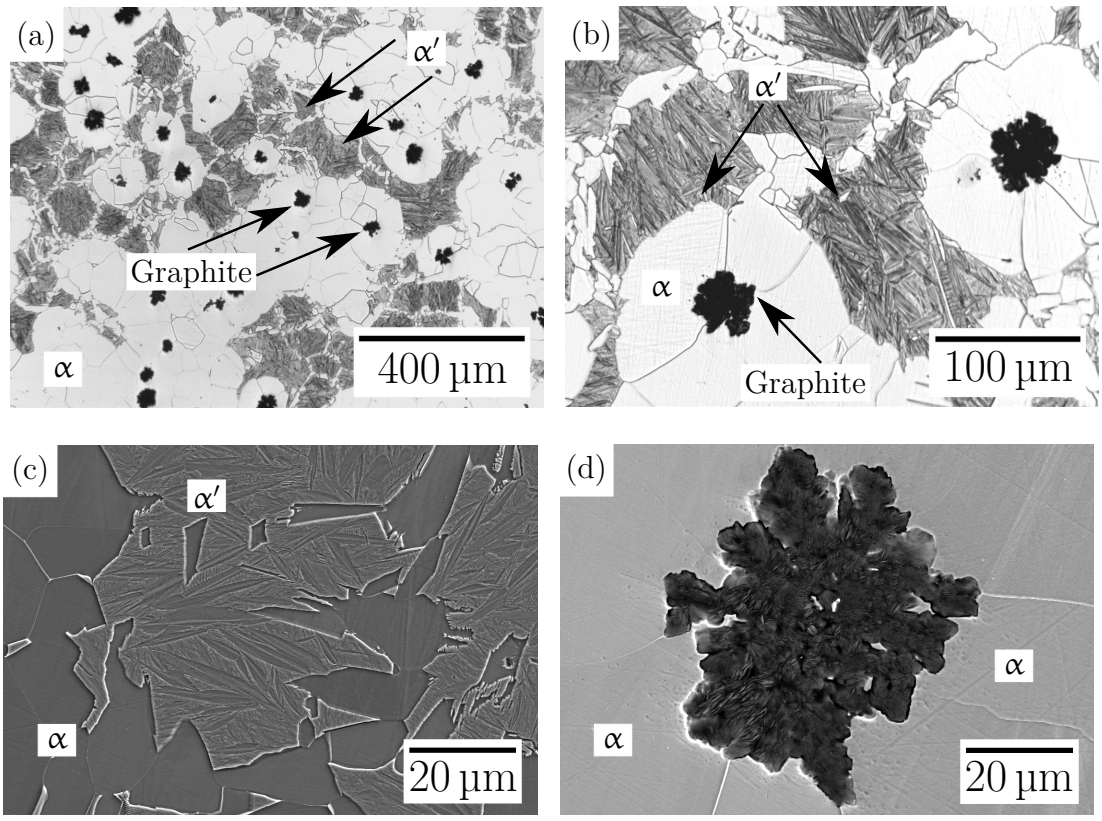


Figure 4.16: Alloy A after isothermal transformation at 800 °C for 5 h. (a) and (b) optical micrographs. Scanning electron micrograph of (c) martensite plates in ferrite and (d) graphite nodules in a ferritic matrix.

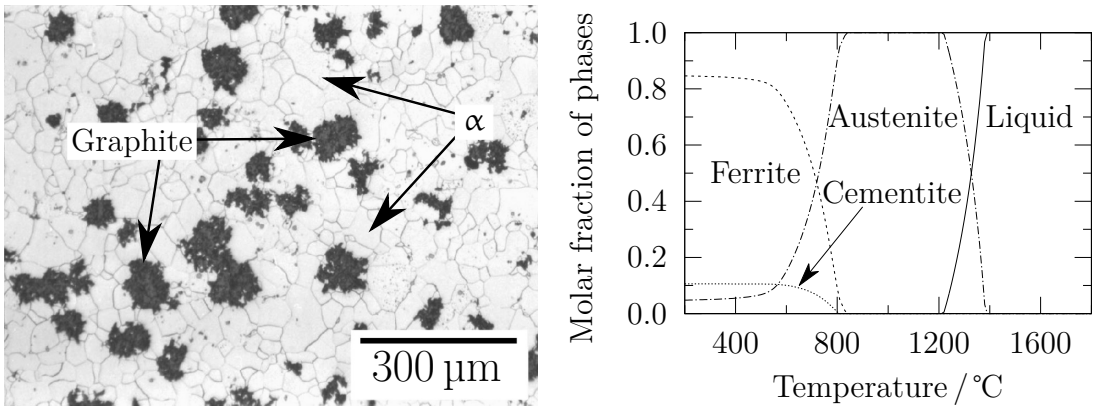


Figure 4.17: (a) Graphite in a ferritic matrix in "blackheart cast iron" held at 900 ℃ for many days before cooling slowly to grow graphite nodules [19, micrograph 795]. (b) Equilibrium phase fractions were calculated over a range of temperatures using MTData [125, 137] for the composition of Alloy A. Liquid, austenite, ferrite and cementite phases are allowed to exist in the calculations.

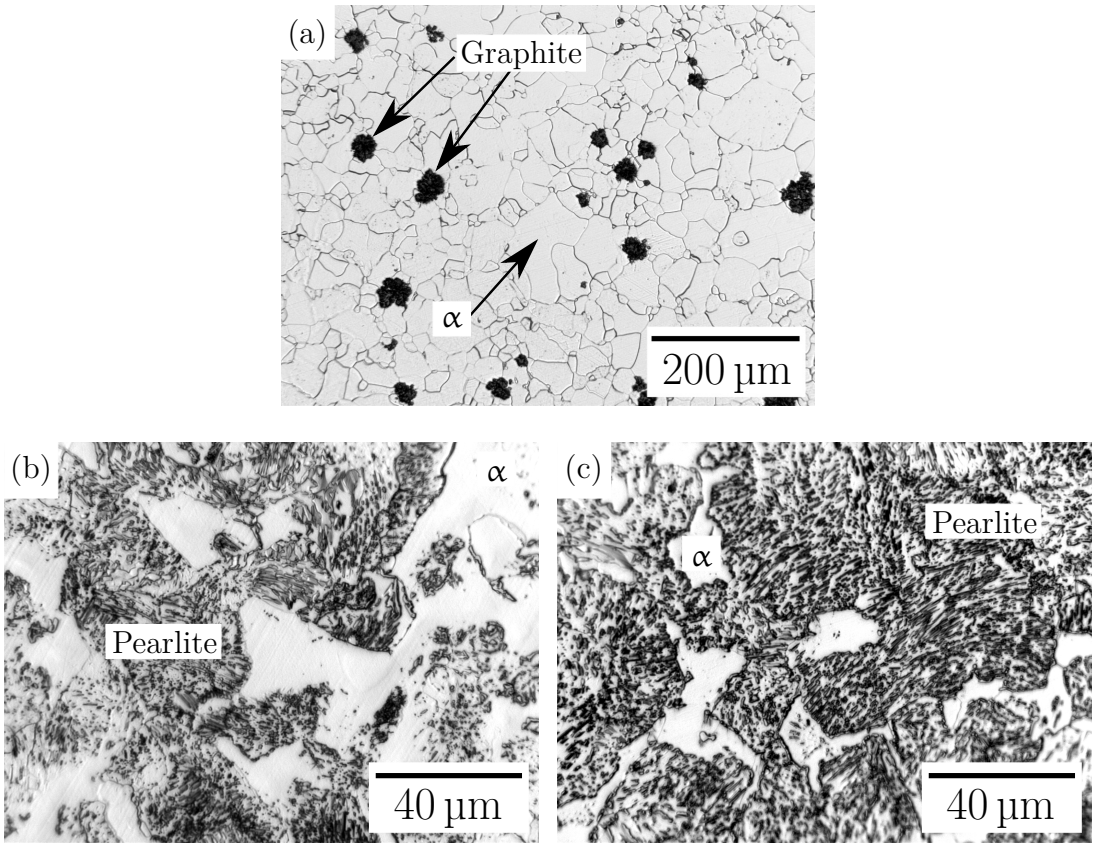


Figure 4.18: Microstructure of Alloy A isothermally transformed for 5 h at (a) 750 ℃, near the centre of the samples containing graphite and ferrite, when the cooling rate is slower. (b) 700 ℃ and (c) 750 ℃, the structure near the surface edges, showing pearlite and allotriomorphic ferrite.

650 °C

Transformation at 650 °C resulting in a mixture of pearlite with a small amount of allotriomorphic ferrite (Fig. 4.19). If graphite is excluded from the calculations, the only phases predicted from thermodynamic modelling are 87 vol.% ferrite, 13 vol.% cementite and 0.15 vol.% molybdenum carbide, Mo_2C. However, Mo_2C was not identified by X - ray diffraction, perhaps because the precipitate fraction is small. However, cementite particles do not form a lamellar structure except in a very small region highlighted in Fig. 4.19c, the reason is that large cementite plates breaks down after prolonged heating; small spherical segments of cementite, or spheroidite are formed.

To test this, sample that were held at 650 °C for only 5 min or 90 s before cooling to ambient temperature, showed the classical pearlite lamellar Fig. 4.19f, with progressive spheroidisation as the time spent at 650 °C increased 4.19d.

Fig. 4.20 shows an expansion at the beginning of the hold due to the ferrite transformation Fig. 4.21, followed by a contraction due to pearlite formation. However, there is a significant increase in the strain at longer times. The reasons for this are not clear but one possibility is that the pearlite does not initially form with its equilibrium composition because of the speed of transformation. Subsequent changes towards equilibrium may occur during prolonged holding at the transformation temperature. In particular, the trade - off between the rejection of (Ni, Al, Si) and enrichment of Mo. As Mo has a bigger atomic size as compared to Ni, Al and Si we can observe an initial drop and subsequent increase in strain value while isothermally holding for longer time. This hypothesis has been partially confirmed using EDX points scanning and the comparison of equilibrium and para-equilibrium[2] calculations Fig. 4.22.

[2]Substitutional alloying elements are unable to partition during the time scale of the experiment compares with equilibrium where substitutional alloying elements diffuses at higher temperature.

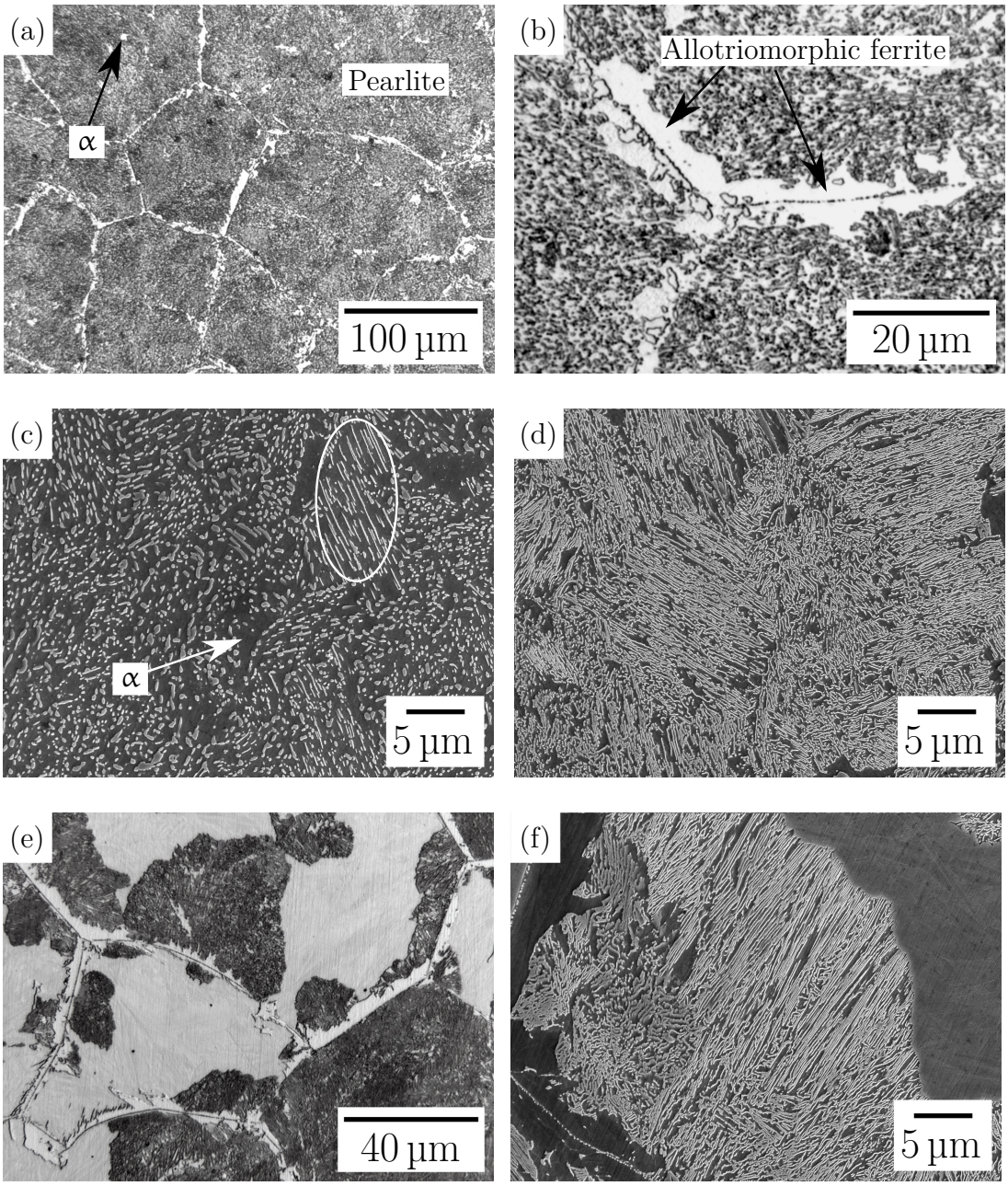


Figure 4.19: Microstructure of Alloy A after isothermal transformation at 650 °C for 5 h, (a) and (b) showing mostly pearlite with allotriomorphic ferrite at prior austenite grain boundaries. (c) Classical pearlite highlighted, the cementite particles in the other regions do not form a lamellar structure. (d) held for 5 min, shows structure of short lamellae. (e) and (f) held for 90 seconds, shows cooperative growth of pearlite.

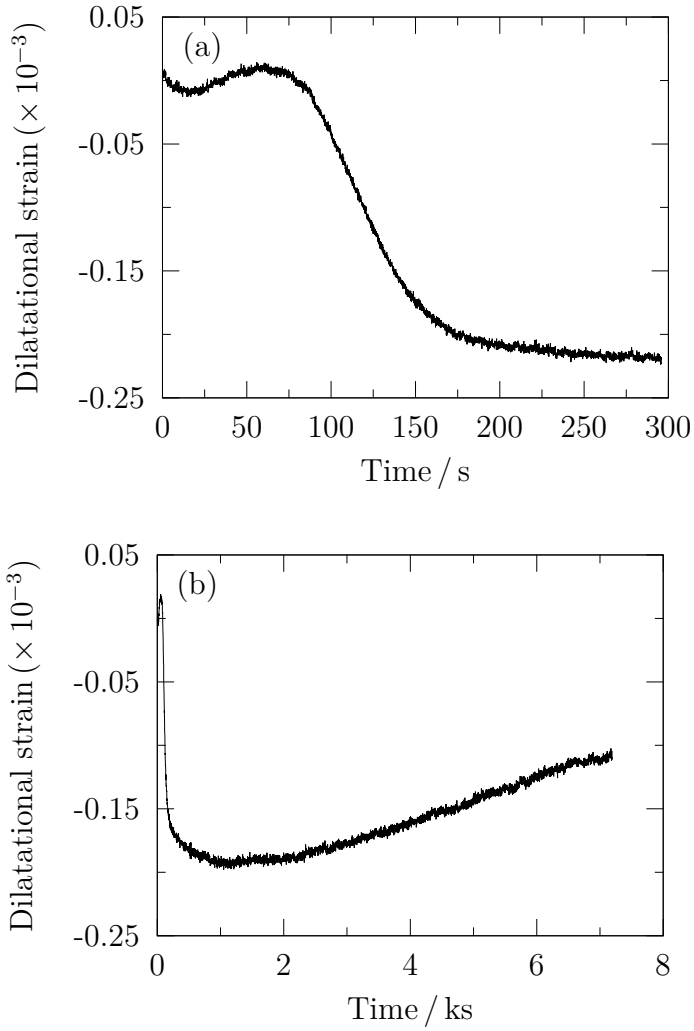


Figure 4.20: Dilatational strain measured during isothermal holding of Alloy A at 650 ℃ for (a) 5 min; (b) 2 h, the strain does not become horizontal due to trade-off of elements.

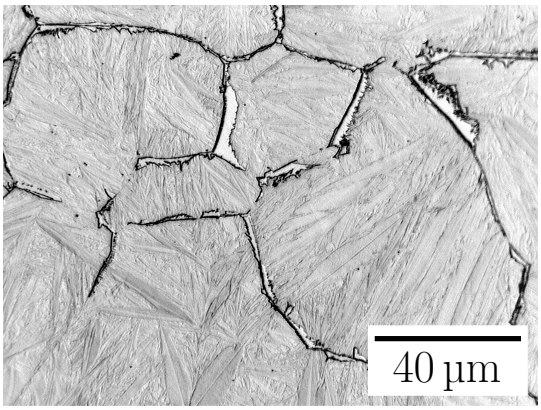


Figure 4.21: Microstructure of Alloy A after isothermal transformation at 650 °C for 30 s, showing mostly martensite with allotriomorphic ferrite at prior austenite grain boundaries.

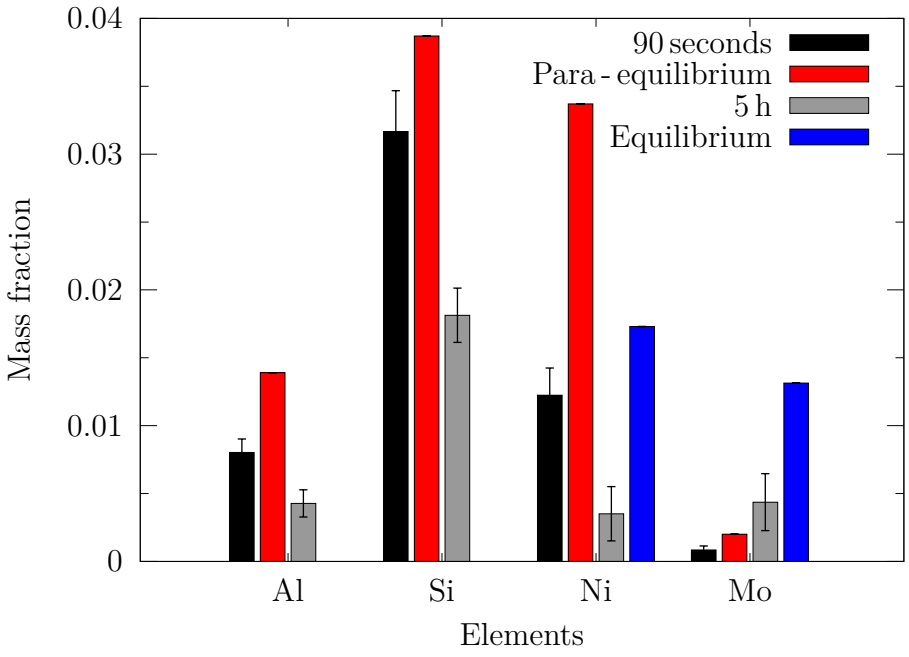


Figure 4.22: Calculated and measured mass fraction of components in cementite phase of Alloy A after isothermal transformation at 650 °C at the time indicated.

600 °C and 550 °C

A significant change happens when the transformation temperature is decreased below 600 °C (Fig. 4.23). Both transformed samples show structure consisting of a martensite and spherodised cementite particles in ferrite. The ferrite has fully recrystallised into equiaxed grains. Thermodynamic calculations suggest that a small amount of austenite ought to remain untransformed at both 600 °C and 550 °C, yet this was not detected using XRD. Cementite and ε carbide peaks are highlighted in the sample transformed at 550 °C (Fig. 4.24). Furthermore, the phase fractions of cementite and ferrite following Rietveld analysis of XRD data are in excellent agreement with thermodynamic calculations in Fig. 4.17b with ≈ 85 vol.% ferrite and ≈ 15.0 vol.% cementite, in the two cases.

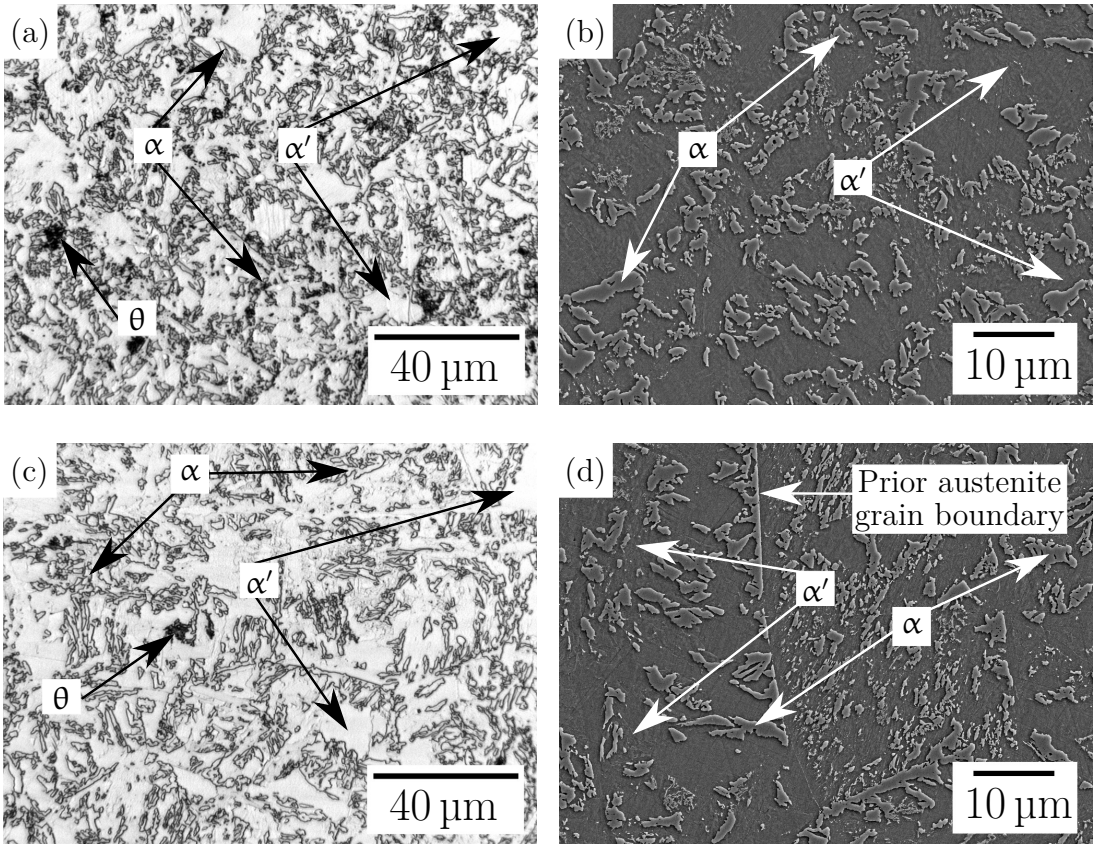


Figure 4.23: Microstructure of Alloy A transformed at (a) and (b) 600 ℃ for 6 h; (c) and (d) 550 ℃ for 6.5 h. Ferrite grains formed on prior austenite grain boundaries scattered with areas of martensite and smaller dark regions of cementite.

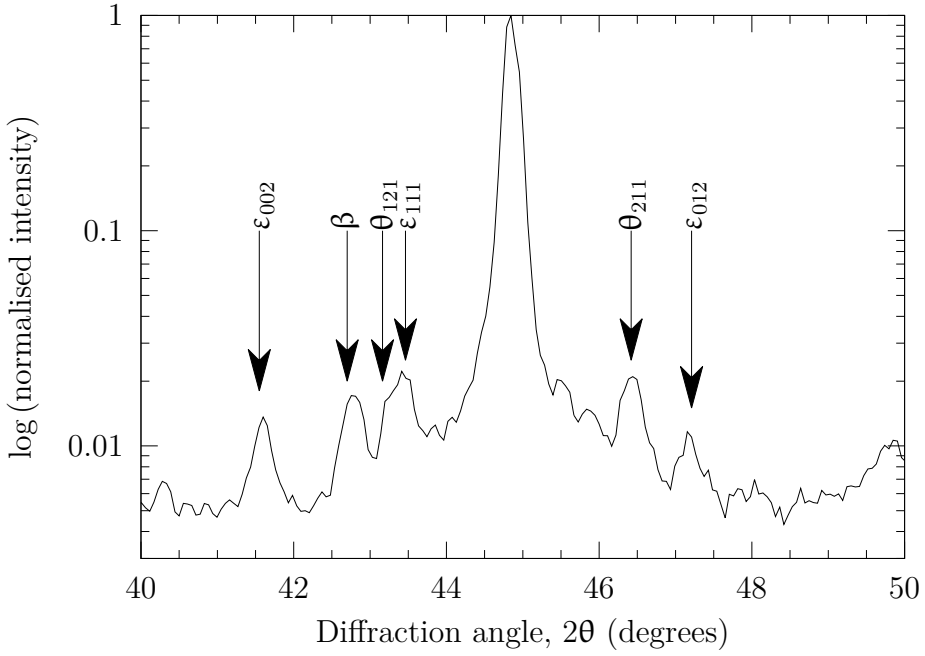


Figure 4.24: XRD data for Alloy A transformed at 550°C, shows ε carbide and cementite peaks, with peak due to CuK_β radiation.

500 °C – 400 °C

Plate-shaped ferrite consistent with displacive transformation (Fig. 4.25) occurs when Alloy A is transformed between 500 °C and 400 °C. Cementite precipitation is restrained because of the existence of silicon and aluminium that are unable to partition at relatively low transformation temperature [e.g., 40, 138–140]. The partitioning of carbon into austenite allows it to be retained to ambient temperature (Fig. 4.26).

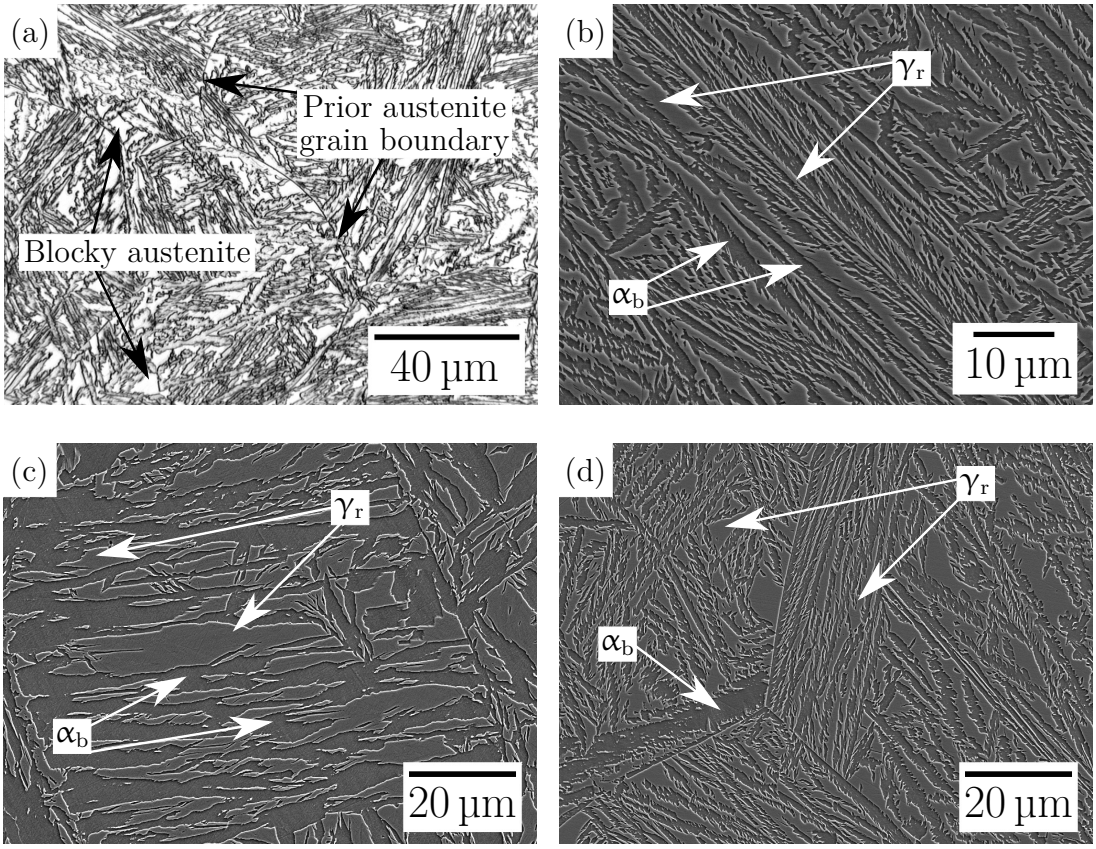


Figure 4.25: Alloy A transformed at (a) and (b) 500 °C, (c) 450 °C and (d) 400 °C. The microstructure consists of films of bainitic ferrite, and retained austenite with regions of blocky austenite.

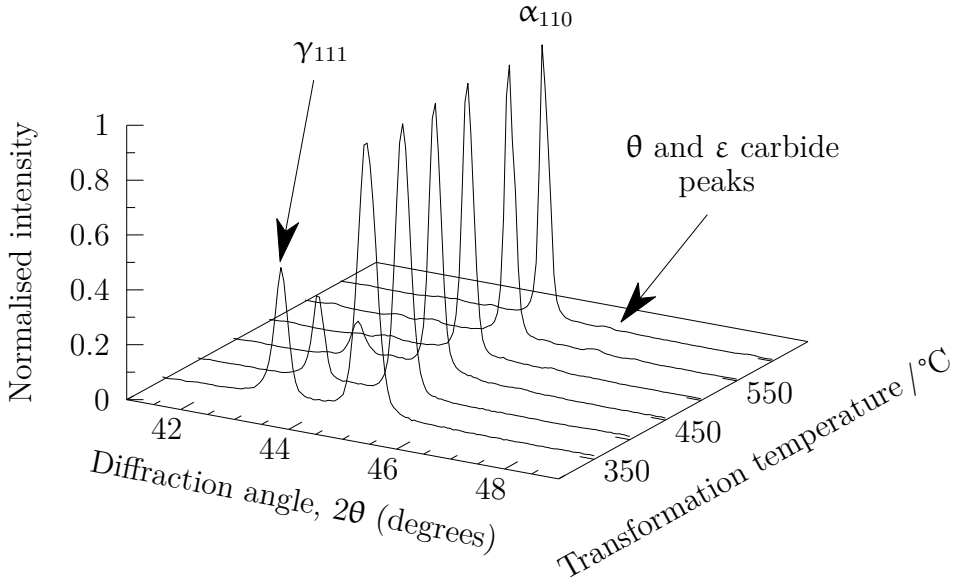


Figure 4.26: Isothermal transformation X - ray diffraction peaks in Alloy A at the temperatures indicated. Retained austenite peaks increases in height as transformation temperature decreases, whereas carbide peaks become smaller and then vanish for transformation at or below 400 ℃.

Below 400 °C

Isothermal transformation at less than 400 °C, prompts fine plates of bainitic ferrite separated by films or blocks of retained austenite (Figs. 4.27, 4.28 and 4.29). No other phases were present as confirmed by XRD (Fig. 4.26). The amount of retained austenite for all of the isothermal transformation temperatures is shown in Fig. 4.30. A microstructure such as this, where fine plates of bainitic ferrite are separated by films of austenite, is in many respects desirable from the perspective of mechanical properties [93, 141–147].

Decreasing the isothermal transformation temperature leads to more refined structure. Using calibrated scanning electron micrographs, the intercepts perpendicular to the long axis of the plates were measured and stereologically corrected [148] to obtain the true widths (Fig. 4.31).

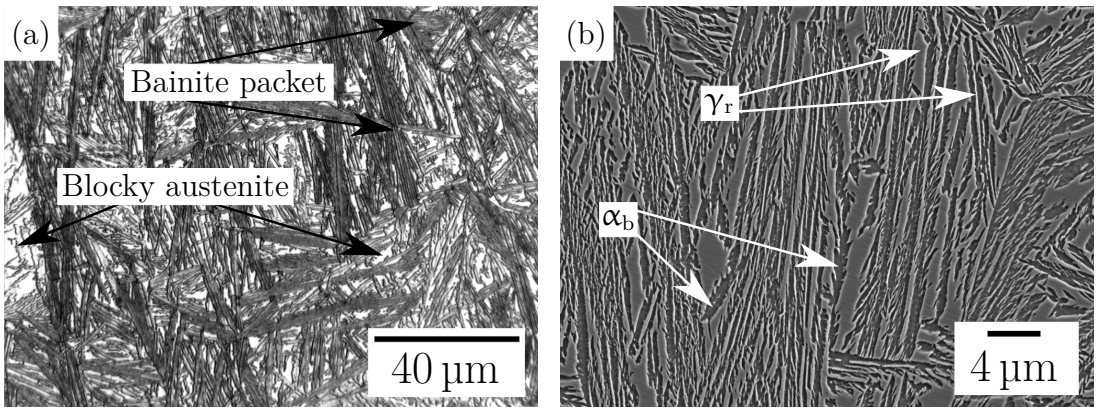


Figure 4.27: Alloy A isothermally transformed at 350 °C for 12 h, blocks of austenite between parallel sheaves of bainite, which also contain films of austenite.

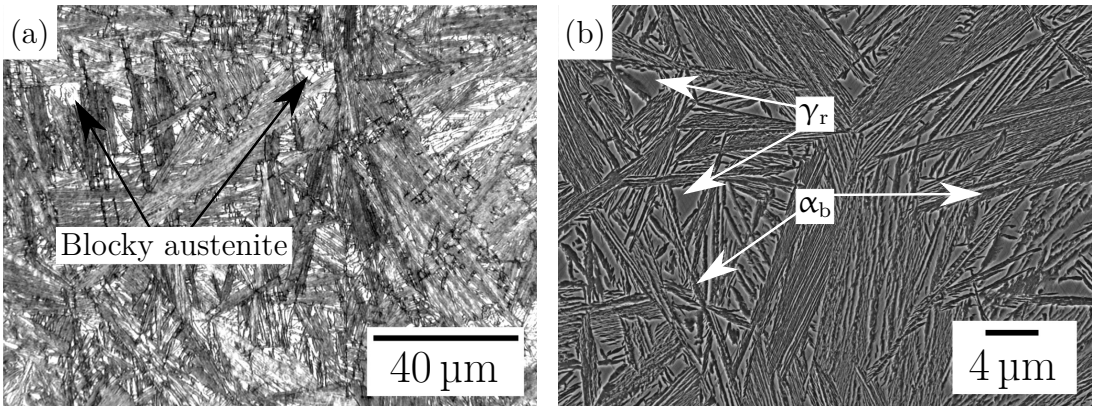


Figure 4.28: Alloy A isothermally transformed at 300 °C for 12 h. The microstructure is profoundly the same as that formed by transformation at 350 °C (Fig. 4.27), but with finer microstructure.

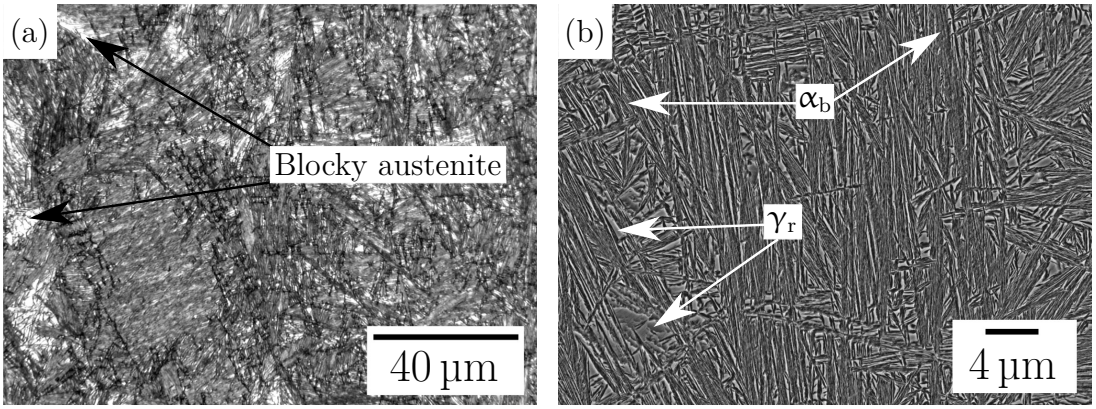


Figure 4.29: Alloy A isothermally transformed at 260 °C for 12 h. Blocks of austenite become finer, consistent with the isothermal transformation at lower transformation temperature.

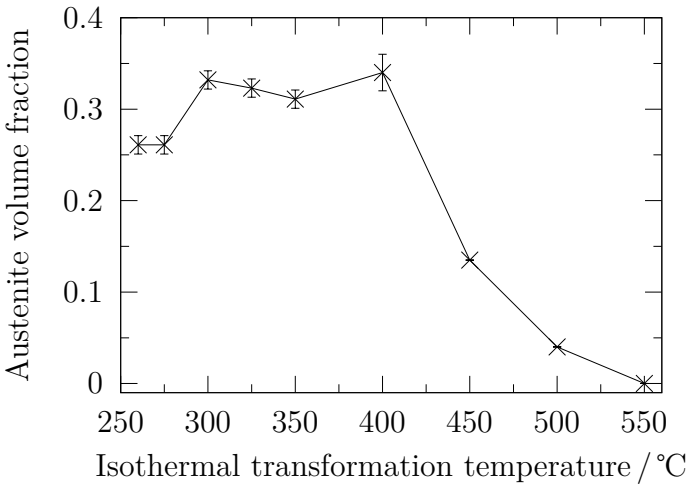


Figure 4.30: Volume fraction of retained austenite obtained via Rietveld analysis of XRD data. As the transformation temperature decreases below 550 ℃, the volume fraction of retained austenite increases. Because of the suppression of cementite by the presence of aluminium and silicon. Carbon in this way stays in solution and stabilises austenite.

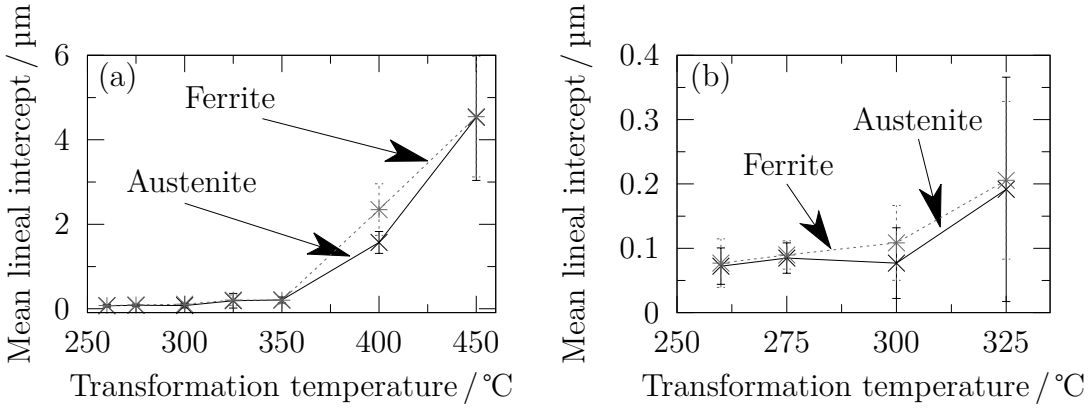


Figure 4.31: Alloy A mean lineal intercept plate width of bainitic ferrite and film austenite after isothermal transformation at the temperatures indicated, stereologically - corrected "$\frac{1}{2}\,\pi\,P_{\mathrm{W}}$", where P_{W} is the plate width [148]. (a) Larger plate widths at higher transformation temperaturer and (b) almost identical finer scale at 325 ℃ and below. The error bars represent one standard deviation over at least ten values.

4.5.2 Alloy B

600 °C and 450 °C

During isothermal holding at 600 °C, there was no visible dilatation even after few hours. This is consistent with predictions that austenite is stable with respect to ferrite at 600 °C. The structure at ambient temperature was therefore martensitic but the grain boundaries were decorated with a strange transformation product (Fig. 4.32). TEM was used to identify these products after lifting out the sample from FIB, confirmed that the transformation products are Mo_2C + α enriched of aluminium and nickel, Fig. 4.33. However, this was not predicted by thermodynamic modelling. Isothermal holding at 450 °C results in a similar structure, although the austenite grain boundaries were clean (Fig. 4.34).

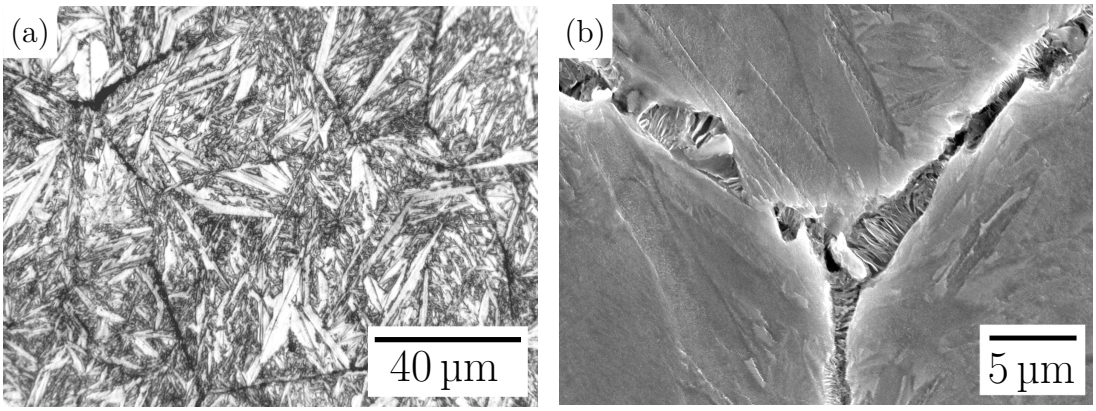


Figure 4.32: Alloy B transformed at 600 °C for 10 h, (a) austenite grain boundaries appear to be decorated with a dark - etching phase mixture and (b) large martensite plates intercept the grain boundaries and the transformation products.

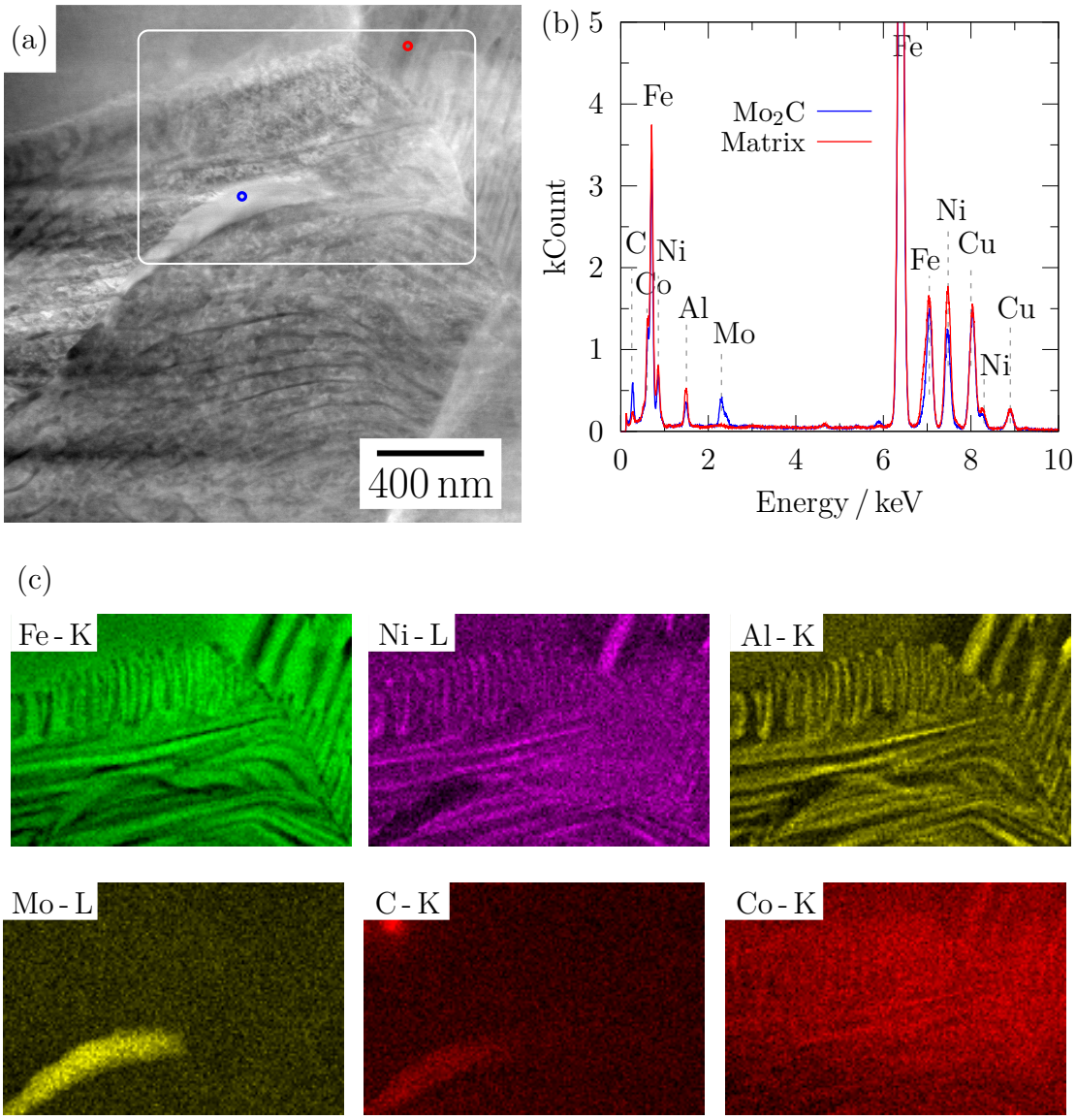


Figure 4.33: (a) STEM bright field image of Alloy B transformed isothermally at 600 °C for 10 h followed by cooling to ambient temperature, highlighted area used for EDS point scanning and elements maping. (b) EDS from the marked region showing enriched regions of Mo_2C in areas containing precipitates and enriched area of aluminium and nickel. (c) STEM - EDX elements maps showing qualitatively the distribution of major constituent elements in the rectangular selection shown in (a).

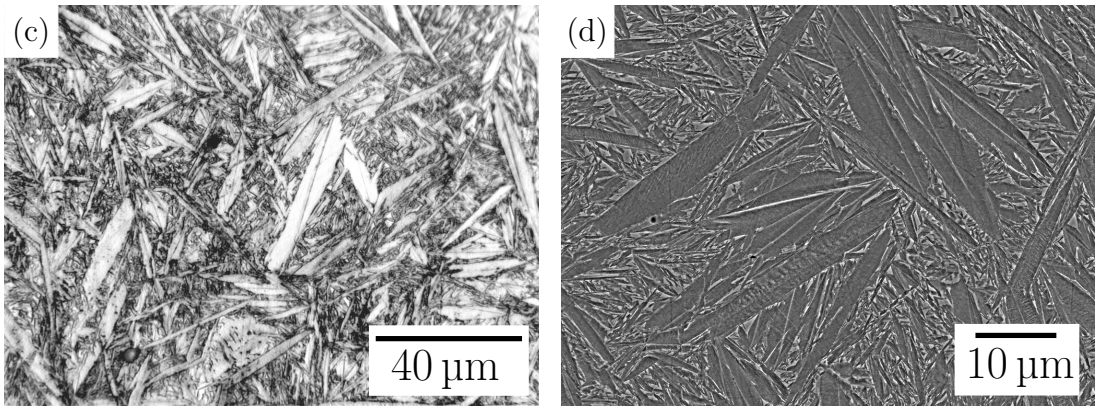


Figure 4.34: (a) and (b) Alloy B transformed at 450 ℃ for 18 h, the structure is the same as that formed by transformation at 600 ℃ but with no dark - etching features at prior austenite grain boundaries.

350 ℃ and 300 ℃

Isothermal transformation at 350 ℃ for 20 h leads to a mixture of fine bainite plates, large areas of martensite and smaller regions of retained austenite (Fig. 4.35). The large austenite blocks will be less enriched with carbon and subsequently transform to martensite after cooling. Smaller austenite regions are known to be more stable [149] and so can be retained to ambient temperature.

Isothermal transformation at 300 ℃ for 20 h revealed similar results to transformation at 350 ℃ with remaining large blocks of austenite transform to martensite upon cooling. However, the bainite plates are finer than after transformation at 350 ℃ (Fig. 4.35d cf. 4.35c). This is not out of the ordinary since a lower temperature requires the plastic deformation of stronger parent austenite and progressively fast work hardening, stifling the bainitic sub-units earlier.

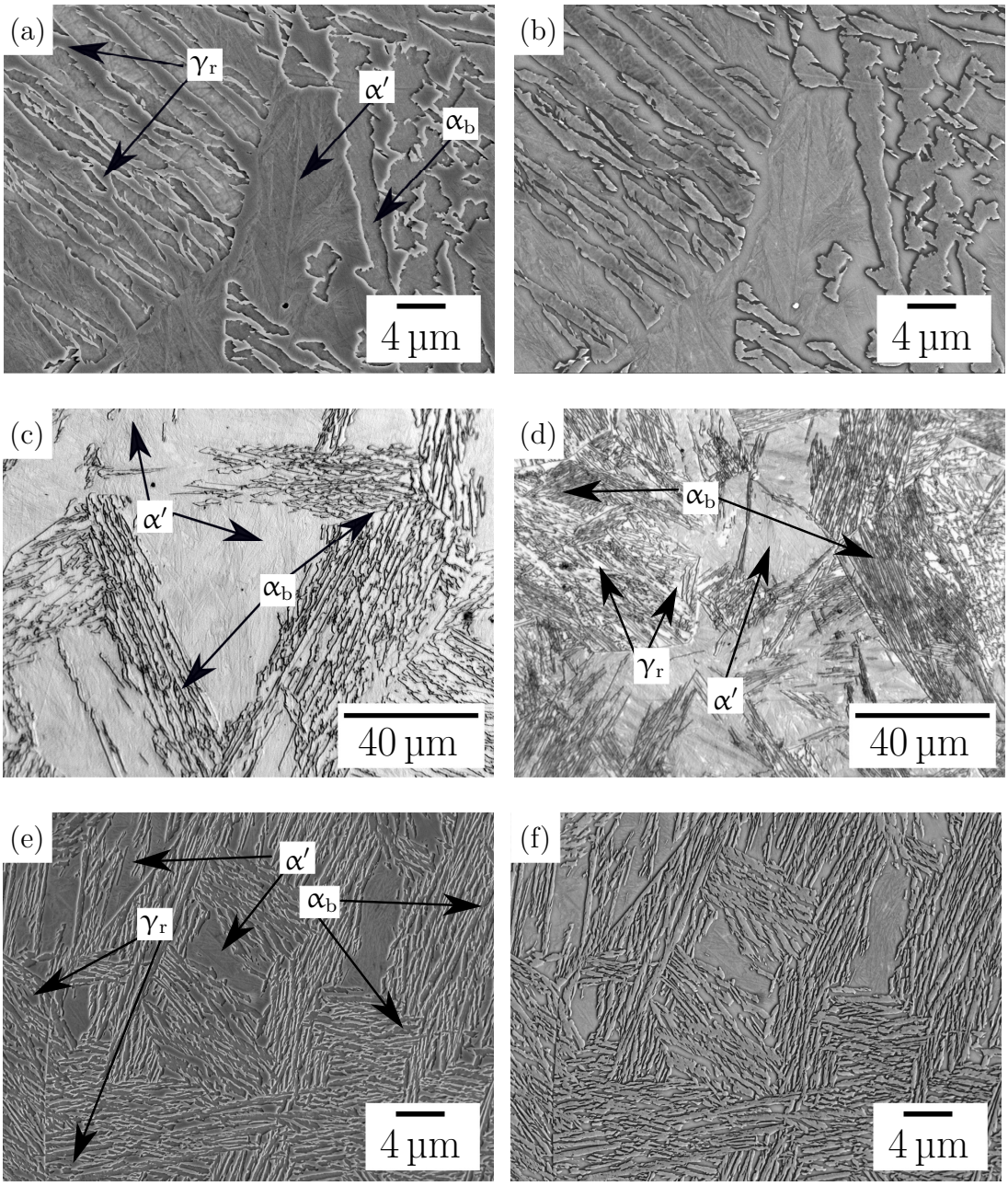


Figure 4.35: Alloy B held at (a), inverted structure (b) and (c) 350 °C for 20 h. The microstructure consists of fine bainite platelets and larger regions of martensite and retained austenite. (d), (e) and inverted structure (e) 300 °C for 20 h, the bainite platelets are finer than those formed during isothermal transformation at 350 °C.

250 °C

After Isothermal transformation at 250 °C for 145 h, the microstructure is mainly a fine mixture of bainitic ferrite and retained austenite (Fig. 4.36). The packets are finer than those formed in Alloy B transformed at higher temperatures. The austenite blocks are ≈ 10 µm in size, much larger than those formed at almost similar transformation temperature in Alloy A (c.f. Fig. 4.29), but are smaller than those that form in Alloy B succeeding isothermal transformation at higher temperatures.

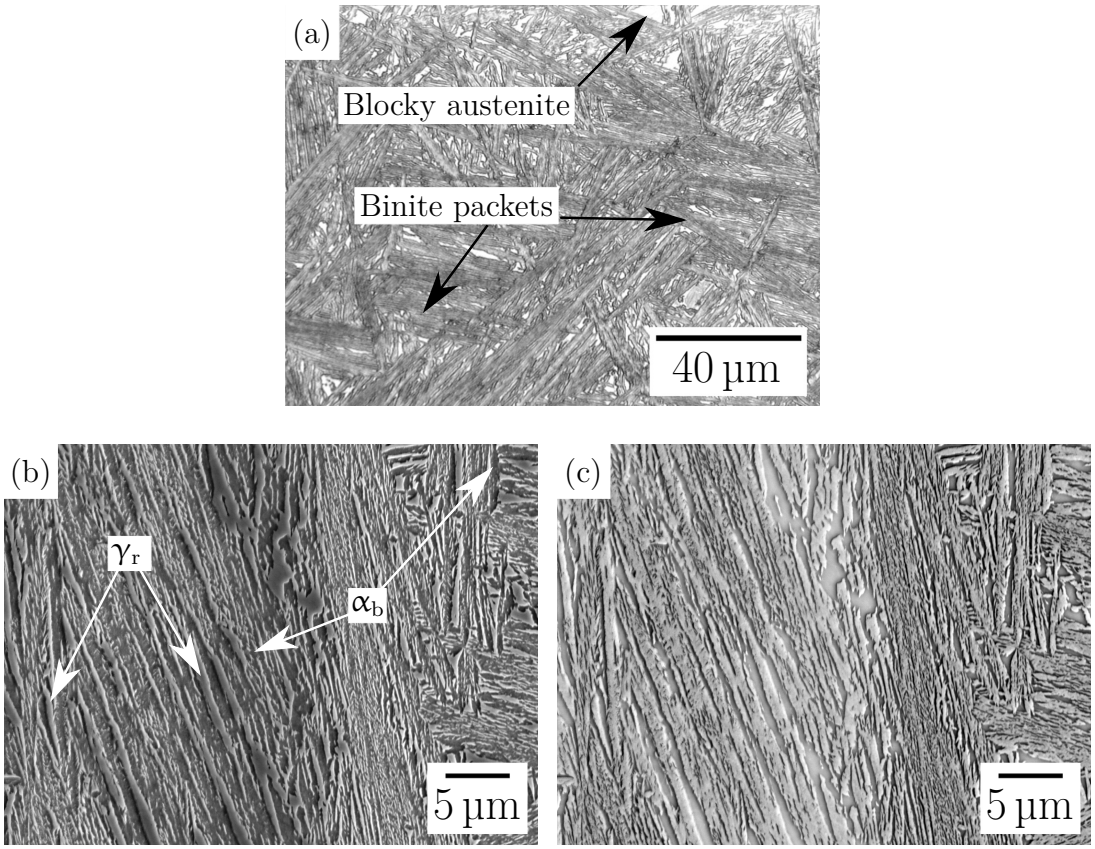


Figure 4.36: Alloy B isothermally transformed at 250 °C for 145 h. Blocks of austenite become smaller and fine platelets of bainite, consistent with the isothermal transformation at lower transformation temperature.

4.6 Conclusions

The presence of austenite in nanostructured bainitic steels is mostly responsible for the toughness. However, the austenite is metastable and previous work has demonstrated that it decomposes into cementite and ferrite upon heating. This decomposition makes the material brittle and weak. Likewise the strength of the microstructure relies upon its scale – the plates of bainite get finer as the transformation temperature is decreased and the strength of the austenite increased [78, 150]. Alloy A and Alloy B were able to form a finer bainitic structure following transformation at 260 ℃ and 250 ℃ respectively and produced the desired microstructure. Consequently these heat treatments were precisely selected for further investigation. In the course of the investigations to find the optimum heat treatments, a number of other phenomena were discovered. It has not been possible to investigate these thoroughly, but they could form the basis of some studies in the future.

- The pearlite obtained during rapid transformation at 650 ℃ does not form with its equilibrium chemical composition, and yet, all models of pearlite growth, without exception, assume the existence of local equilibrium at the common front with the austenite.
- The high-silicon steel has a tendency to form graphite during heat treatment at temperatures in excess of 650 ℃. This in itself is not surprising but it would be useful to do extremely long heat treatments at lower temperatures to study the long-term stability of the alloy system.
- A peculiar reaction is observed in the high aluminium/nickel-containing alloy, where a mixture of molybdenum carbide and ferrite forms austenite. This may be like a fibrous “alloy-pearlite” and bears further investigation.

Chapter 5

Tensile deformation of stable bainite

The purpose of the work presented in this chapter was to examine the behaviour of the two richly alloyed carbide free bainitic steels during tensile deformation. Although there are numerous similar studies in the literature, the alloys considered here unique in that that contain large concentrations of solutes that dramatically alter the relative stabilities of the austenite and ferrite. As will be seen later this has very interesting consequences on the tensile properties as a function of the test temperature.

5.1 Heat treatment

The heat treatment of the alloys studied are listed in Table 5.1. Both are designed to generate a mixed nanostructure of bainitic ferrite plates embedded in a matrix of carbon-enriched austenite. Each sample was transformed as a blank ≈12 mm diameter, 70 mm length with mechanical test specimens machined subsequently from the centre of each blank to avoid any decarburised regions. Heat treatment consisted of austenitisation at 1000 °C for 30 min in a box furnace, followed by isothermal transformation in a fluidised bed, Table 5.1.

Alloy	T_{α_b} / °C	t_{α_b} / h
A	260	24
B	250	120

Table 5.1: Isothermal transformation (T_{α_b}) and time (t_{α_b}).

Tensile tests on samples with the dimensions illustrated in Fig. 3.1, were carried out at ambient temperature, 200 °C and 450 °C. The incremental work hardening exponent was calculated as $n = \mathrm{d}(\ln \sigma)/\mathrm{d}(\ln \varepsilon_p)$, where σ is the stress and ε_p the plastic strain.

5.2 As-transformed microstructures

Representative scanning transmission electron micrographs of the two alloys following the heat treatments listed in Table 5.1 are presented in Fig. 5.1, showing the expected two-phase mixtures of bainitic ferrite and retained austenite.

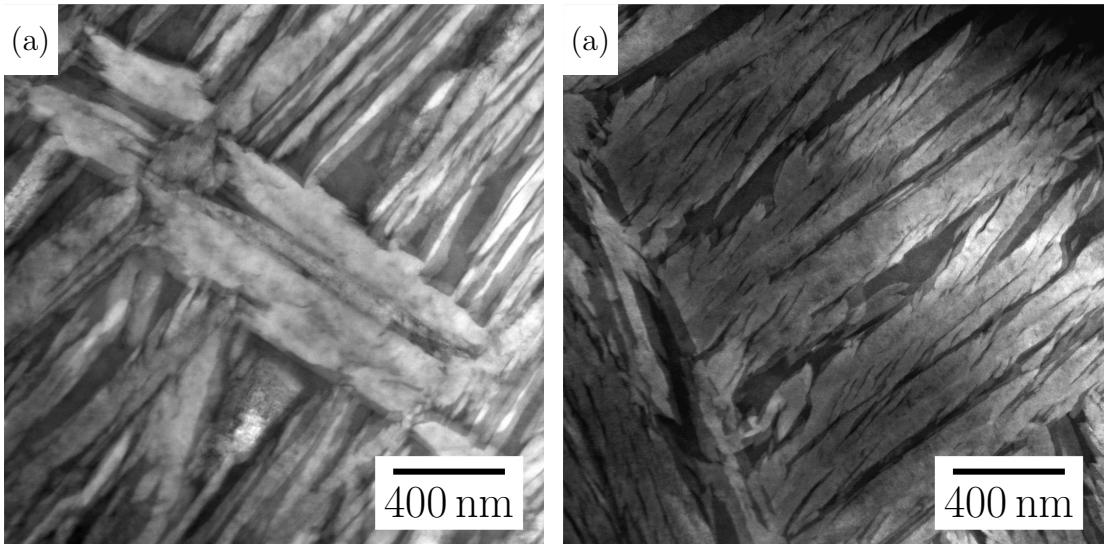


Figure 5.1: STEM bright field images for the as-transformed condition, showing mixtures of bainitic ferrite and retained austenite. (a) Alloy A. (b) Alloy B.

5.3 Mechanical behaviour

The raw tensile test data are presented in Figs. 5.2 and 5.3, with derived parameters listed in Table 5.2. Consistent with expectations, the higher carbon Alloy A is stronger and its performance compares well with other nanocrystalline steels rich in silicon [67].

Linear regression analysis indicates that about 60-66 % of the variation in ductility can be understood in terms of the strength (Fig. 5.4), because stronger steels in general strain harden more rapidly, causing the ultimate tensile strength to be reached at a smaller uniform strain. To understand the residue of the elongation, the mechanical and thermal stability of the retained austenite was examined in detail.

Alloy	Test temperature	0.2% σ_{PS}	σ_{UTS}	ε_U	ε_T	ε_A
	℃	MPa	MPa	%	%	%
A	ambient	1516	1888	3.1	8.0	25.3
	200	1262	2024	12.7	12.2	16.5
	450	886	1169	4.1	28.1	79.9
B	ambient	1036	1396	4.8	12.6	48.6
	200	889	1423	18.7	25.3	40.4
	450	695	888	3.3	25.1	84.4

Table 5.2: Mechanical properties for Alloy A and hs. σ_{PS} and σ_{UTS} are the proof and ultimate tensile strengths respectively, ε_U & ε_T are the uniform and total elongations respectively, and ε_A is the reduction of area.

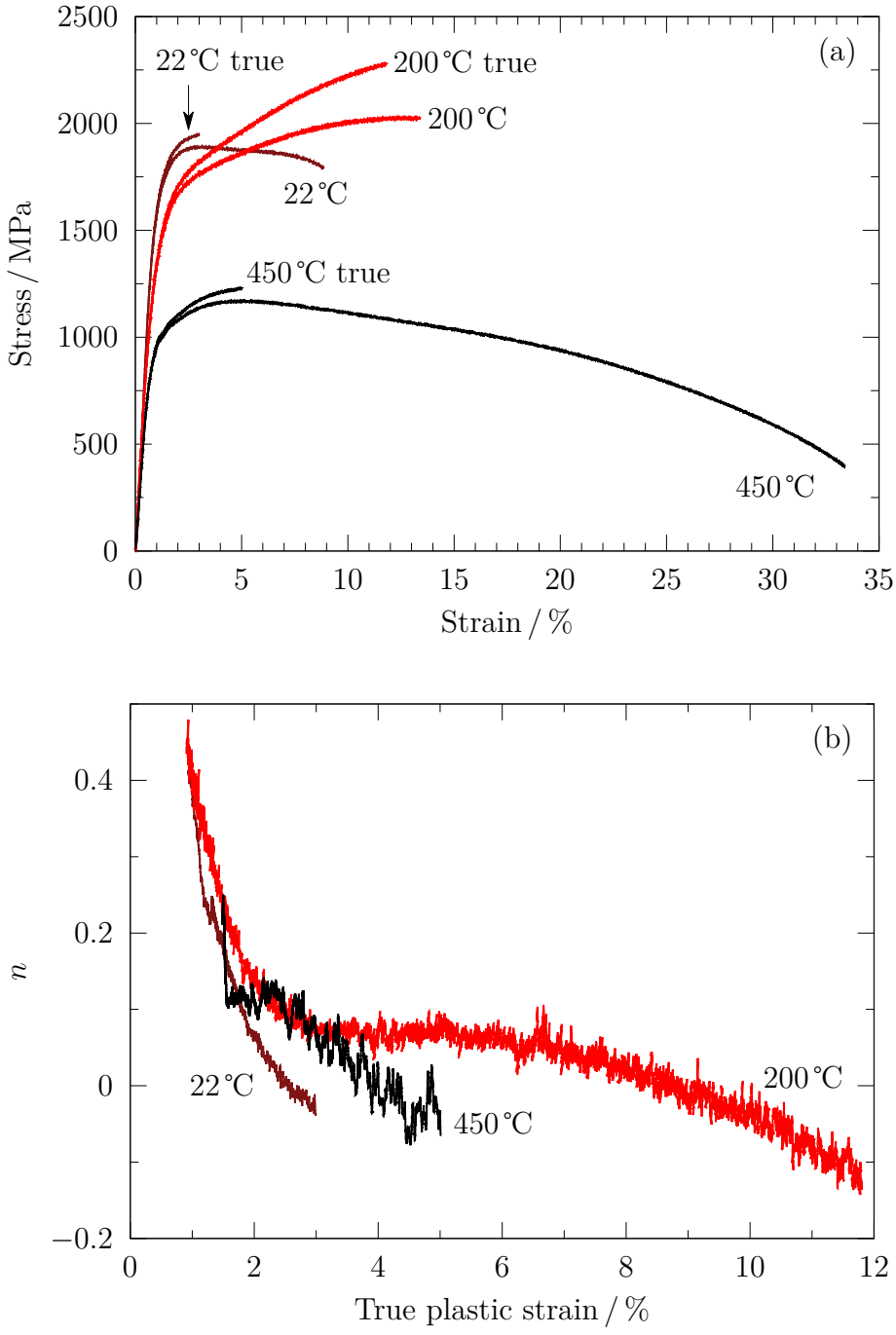


Figure 5.2: (a) True and engineering stress-strain curves as a function of test temperature, (b) derived strain hardening characteristics for Alloy A.

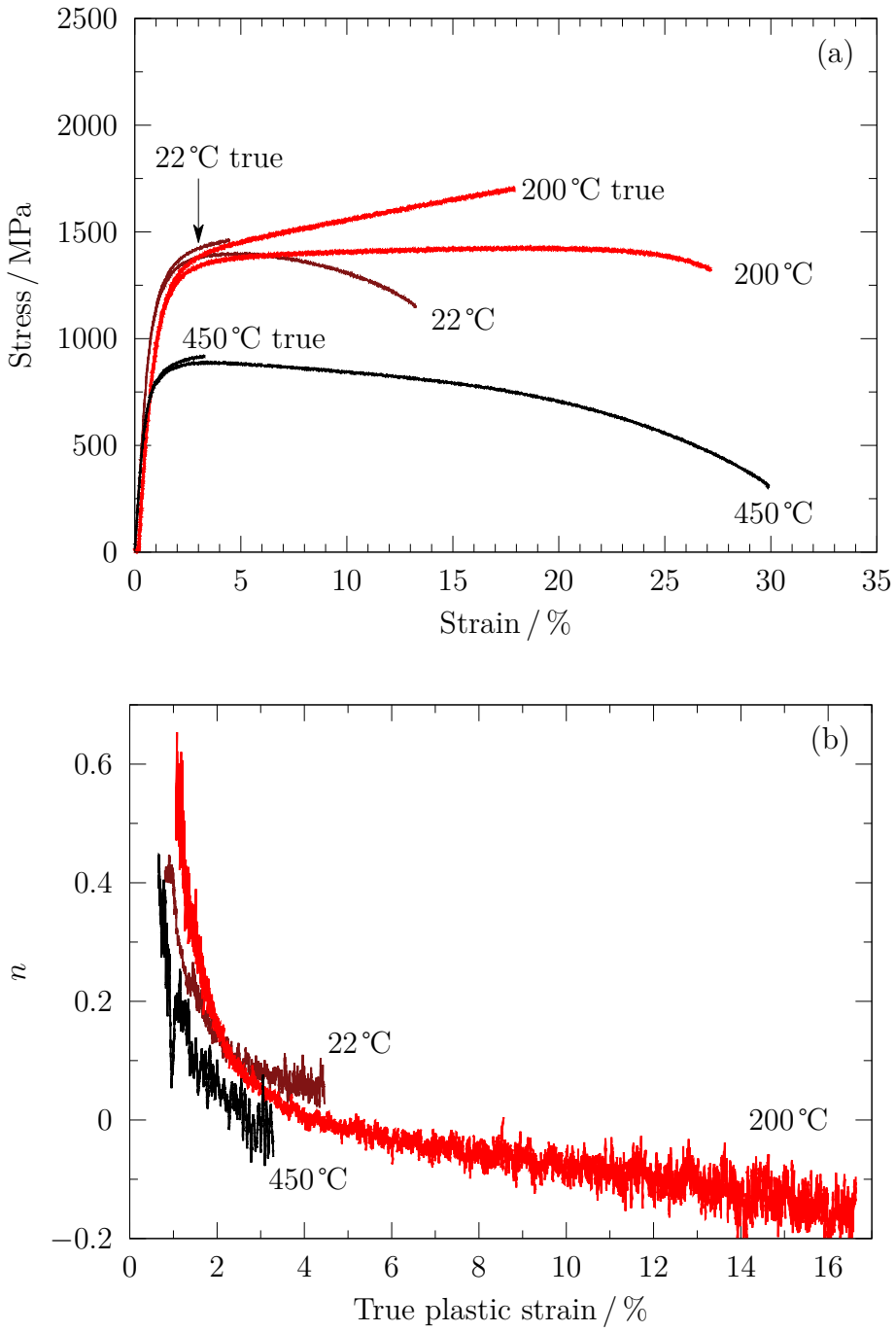


Figure 5.3: (a) True and engineering stress-strain curves as a function of test temperature, (b) derived strain hardeningcharacteristics for Alloy B.

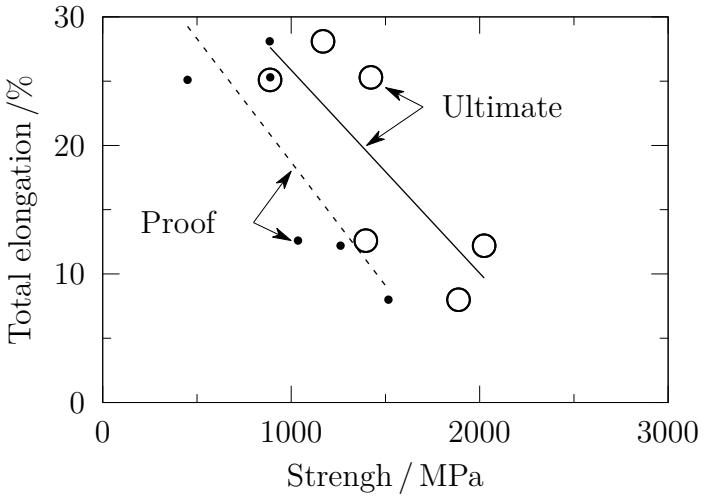


Figure 5.4: Ductility of all six tensile tests plotted together as a function of strength.

5.4 Retained austenite

The ductility of TRIP-assisted steels is, often justifiably, correlated to its retained austenite content. In essence, the deformation-induced transformation of austenite into hard martensite leads to work hardening that delays the onset of plastic instability. However, the data presented in Table 5.3 do not lend themselves to a simple interpretation.

For example, with δ-TRIP steel, tensile tests conducted at ambient temperature exhibited greater ductility than when tested at 100 ℃ [151]. The thermodynamic stability of austenite increases at higher temperatures, so when tested at 100 ℃, the austenite did not transform, leading to a reduced work-hardening rate and hence a smaller uniform ductility. Contrary to those observations, the ductility in the present case actually increases when the tensile tests are conducted at 200 ℃ even though the ultimate strength is greater than those tested at ambient temperature.

The greater uniform elongation in the 200 ℃ sample could be due to the more gradual transformation of retained austenite. This was confirmed by interrupting

a test at 200 °C when the plastic strain reached the failure elongation of the ambient temperature sample, at which point almost half of the austenite remained untransformed (Table 5.3), whereas little austenite remained in the ambient temperature sample.

Before commenting on the elevated temperature tests, it is important to appreciate that the austenite contents listed in Table 5.3 were measured at ambient temperature rather than at the test temperature. As will become obvious shortly, there are strong indications that some of the austenite, *during cooling* from the deformation temperature, transforms into martensite. Furthermore, the 450 °C data indicate that there is a significant *decrease* in the carbon concentration of the retained austenite in the unstressed gauge section of the tensile specimen. This indicates structural changes other than martensitic transformation. Assuming that the thermal activation available at 450 °C is adequate, the calculated equilibrium phase diagrams (Fig. 5.5) indicate that it is possible for carbides to precipitate during the course of the test in the case of Alloy A, and that additional austenite may form in Alloy B. Both of these phenomena could lead to a reduction in the carbon concentration of the austenite. Experiments were conducted to investigate this further.

Alloy	Test temperature / ℃	Section	V_γ	a_γ / Å	C_γ / wt%
A	ambient	FS	0.03 ± 0.01	–	–
		GS	0.28 ± 0.01	3.6332 ± 0.0052	1.44 ± 0.03
	200 ℃	FS	0	–	–
		GS	0.26 ± 0.02	3.6360 ± 0.0031	1.52 ± 0.01
	450 ℃	FS	0	–	–
		GS	0.22 ± 0.01	3.6246 ± 0.0042	1.18 ± 0.04
B	ambient	FS	0.04 ± 0.02	–	–
		GS	0.27 ± 0.02	3.6457 ± 0.0016	1.65 ± 0.02
	200 ℃	FS	0.01 ± 0.02	–	–
		GS	0.25 ± 0.02	3.6360 ± 0.0018	1.36 ± 0.02
	200 ℃[†]	FS	0.13 ± 0.01	3.6309 ± 0.0050	1.20 ± 0.04
	450 ℃	FS	0.02	–	–
		GS	0.28 ± 0.01	3.6299 ± 0.015	1.18 ± 0.03

Table 5.3: Diffraction data for both alloys tested at the temperature as indicated. [†] tensile test at 200 ℃ was stopped when the plastic strain reaches the failure elongation of the ambient temperature sample.

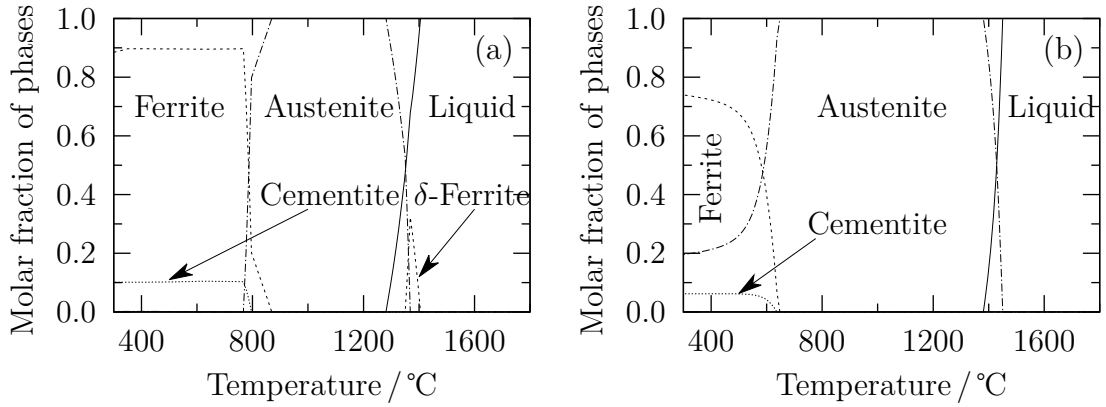


Figure 5.5: Phase fractions were calculated using the commercial software *Thermo-Calc* and the thermodynamic database TCFE8 [127, 128]. (a) Alloy A is predicted to be completely austenitic between 870 ℃ and 1270 ℃. (b) Alloy B is predicted to be completely austenitic between 650 ℃ and 1390 ℃.

5.5 Austenite reversion in Alloy B

The experiments here were done on the bainitic samples generated using the heat treatments described in Table 5.1. The aim was to study whether additional austenite would form at 450 ℃; only the results for Alloy B are reported because austenite growth was not detected in the case of Alloy A, consistent with the calculated equilibrium phase diagrams.

Fig. 5.6a showing that a significant amount of austenite forms during treatment at 450 and 500 ℃, as revealed by the isothermal contraction strains. An approximate measure of how much additional austenite forms is given by comparing the total transformation strain when all of the microstructure converts into austenite at any given temperature (Fig. 5.6b), with the observed contraction strain in Fig. 5.6a.

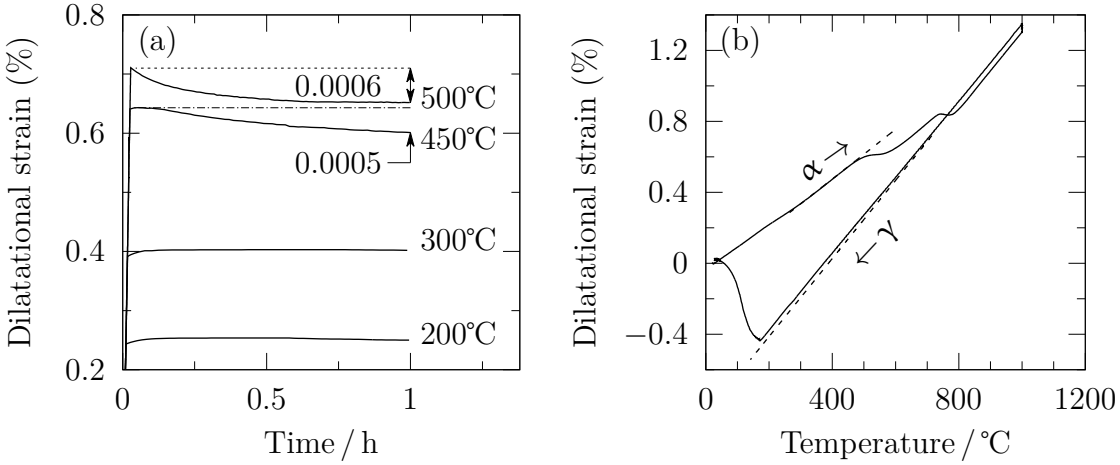


Figure 5.6: Alloy B. (a) Isothermal experiments to show austenite formation as indicated by a contraction as a function of time. (b) A typical heating and cooling curve showing the linear transformation strain, i.e. the vertical distance at 450 ℃ between the dashed lines, as a function of temperature. From Figs. 5.6a and 5.6b the amount of the austenite is expected to form during the tensile test at 450 ℃ is $\approx 10\%$.

The importance of these observations is that some austenite is expected to form during the 450 ℃ tensile tests for Alloy B, consistent with the observed reduction in the carbon concentration (Table 5.3) due to dilution. The dilution should make the austenite less stable to martensitic transformation. To prove this, experiments were conducted on the bainitic samples using a deformation dilatometer. The samples were heated to the temperature at which tensile tests had been conducted, deformed plastically by 5% in compression, and allowed to cool to ambient temperature at a rate of $5\,^{\circ}\mathrm{C\,s^{-1}}$. The strain monitored could then be used to assess whether the deformed austenite transformed during cooling to ambient temperature. Fig. 5.12 shows, as predicted, that a significant amount of martensitic transformation occurs during the cooling of the samples deformed at 450 ℃. This is not the case for the samples deformed at 200 ℃. Furthermore, the martensite-start temperatures $M_{\mathrm{S}}^{\gamma\mathrm{r}}$ of the *retained austenite* in the 450 ℃ deformed samples are close to or greater than when the alloy is fully austenitic (M_{S}^{γ}), Fig. 5.12.

Hardness measurements presented in Table 5.4 confirm the dilatometric data. A comparison of the the grip and fracture regions, shows that Alloy B samples tested at 450 ℃ hardened significantly when compared with the same test for Alloy A Fig. 5.8. It is the martensite that forms during cooling from the tensile test temperature that is responsible for this. The main conclusion is that during testing at 450 ℃, the austenite in Alloy B will not undergo deformation-induced transformation, but rather, will increase in volume fraction, the resulting dilution leading to martensitic transformation during cooling. This explains the minimal work hardening in the 450 ℃ tensile curve illustrated in Fig. 5.3a.

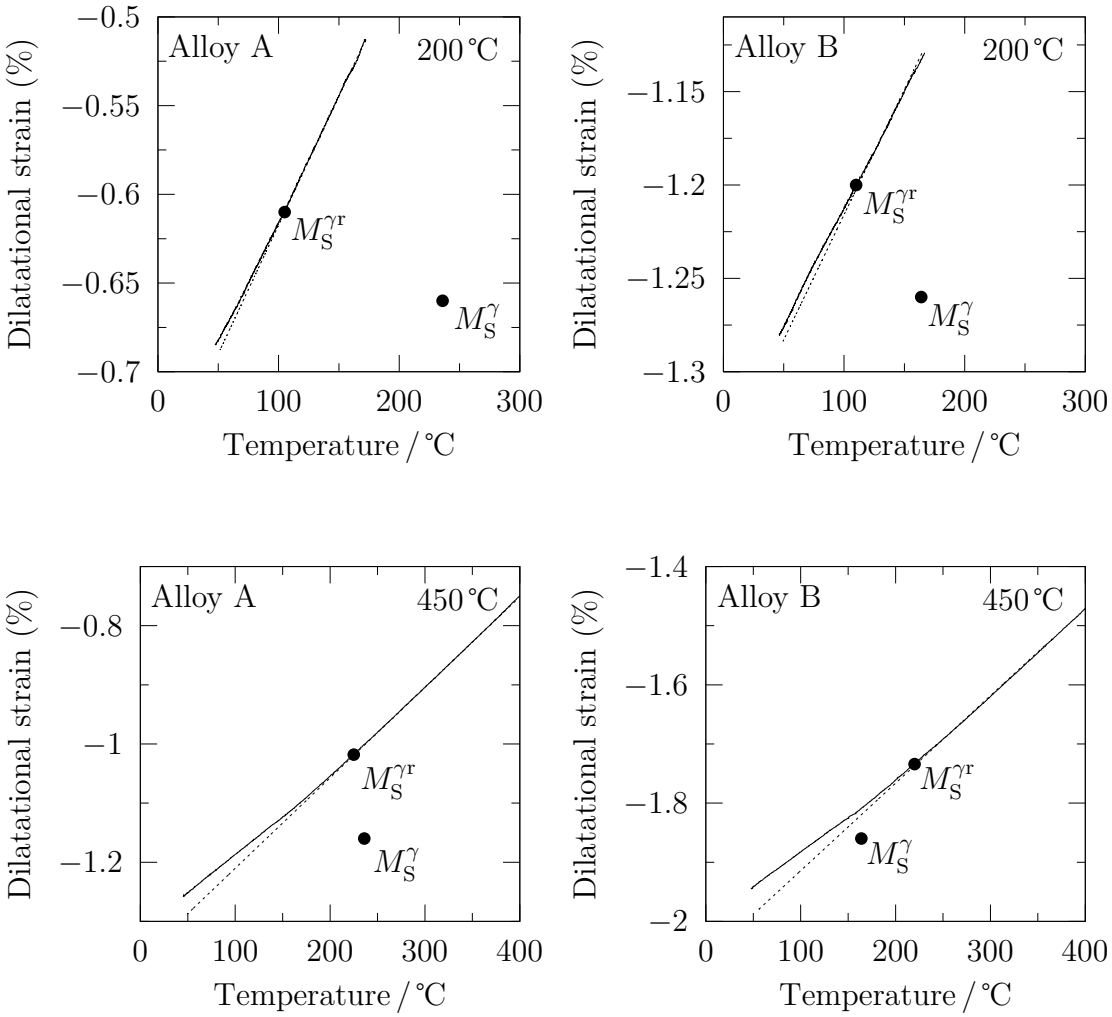


Figure 5.7: The dilatation curves for the bainitic samples with deformation of 5% at the temperature indicated. $M_S^{\gamma r}$ is martensite start temperature for the retained austenite structure and M_S^{γ} is martensite start temperature for the case where the alloy is fully austenitic.

Alloy	Tensile test temperature	Fracture surface	Grip section	Change
A	ambient	626 ± 18	577 ± 10	49±28
	200 °C	656 ± 16	581 ± 13	75±29
	450 °C	597 ± 9	590 ± 16	7±25
B	ambient	543 ± 9	460 ± 11	83±20
	200 °C	602 ± 20	435 ± 13	167±33
	450 °C	610 ± 20	496 ± 12	113±32

Table 5.4: Measured Vickers hardness of tensile test samples, using a 10 kg load. "Change" refers to the difference in hardness between the fracture and grip regions.

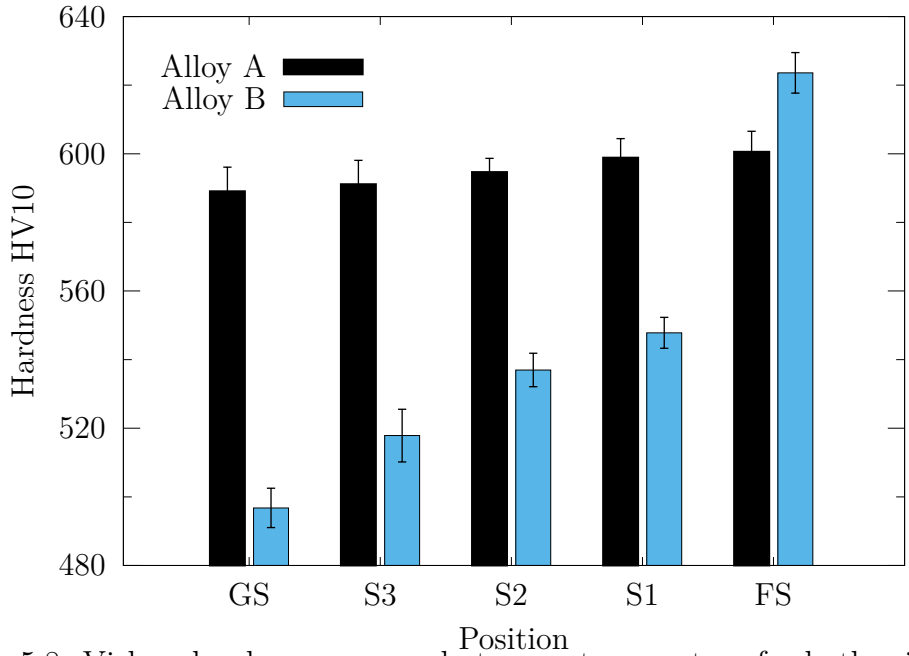


Figure 5.8: Vickers hardness measured at room temperature for both microstructure tested at 450 °C at different cross sections of the tensile test samples. From S1 to FS the hardness increased dramatically in Alloy B compared to Alloy A due to the amount of retained austenite in the regions.

5.6 Cementite precipitation

Transmission electron micrographs are presented in Fig. 5.9 of samples extracted from the hot tensile tests. They show that there was no detectable carbide formation when Alloy B was tested at either 200 or 450 ℃. Alloy A on the other hand, revealed precipitation in the sample tested at 450 ℃, explaining the reduction in the carbon concentration of the austenite following testing (Table 5.3). Diffraction patterns and dark-field images are presented in (Figs. 5.10 and 5.11).

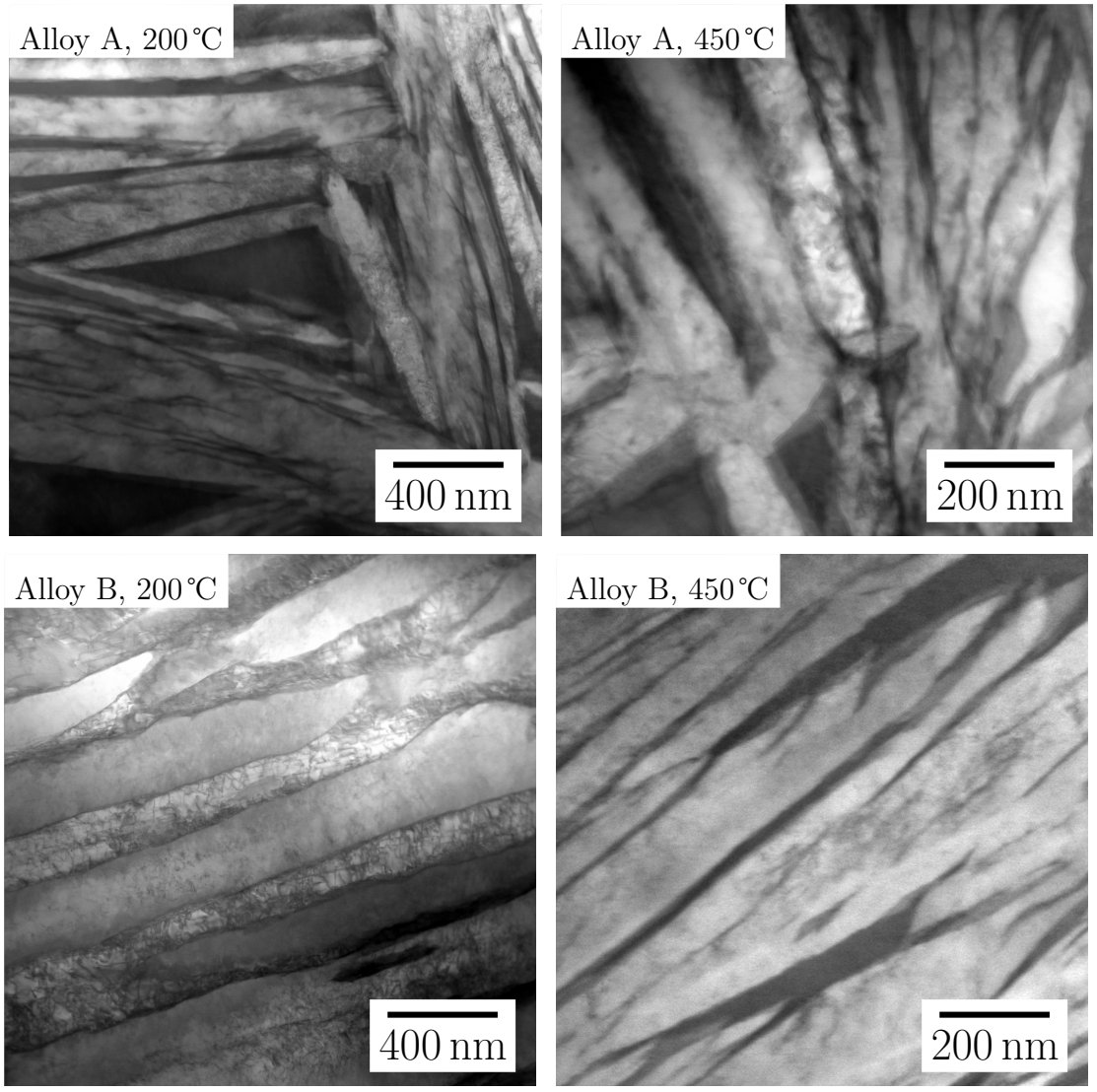


Figure 5.9: TEM following tensile testing at the temperatures indicated.

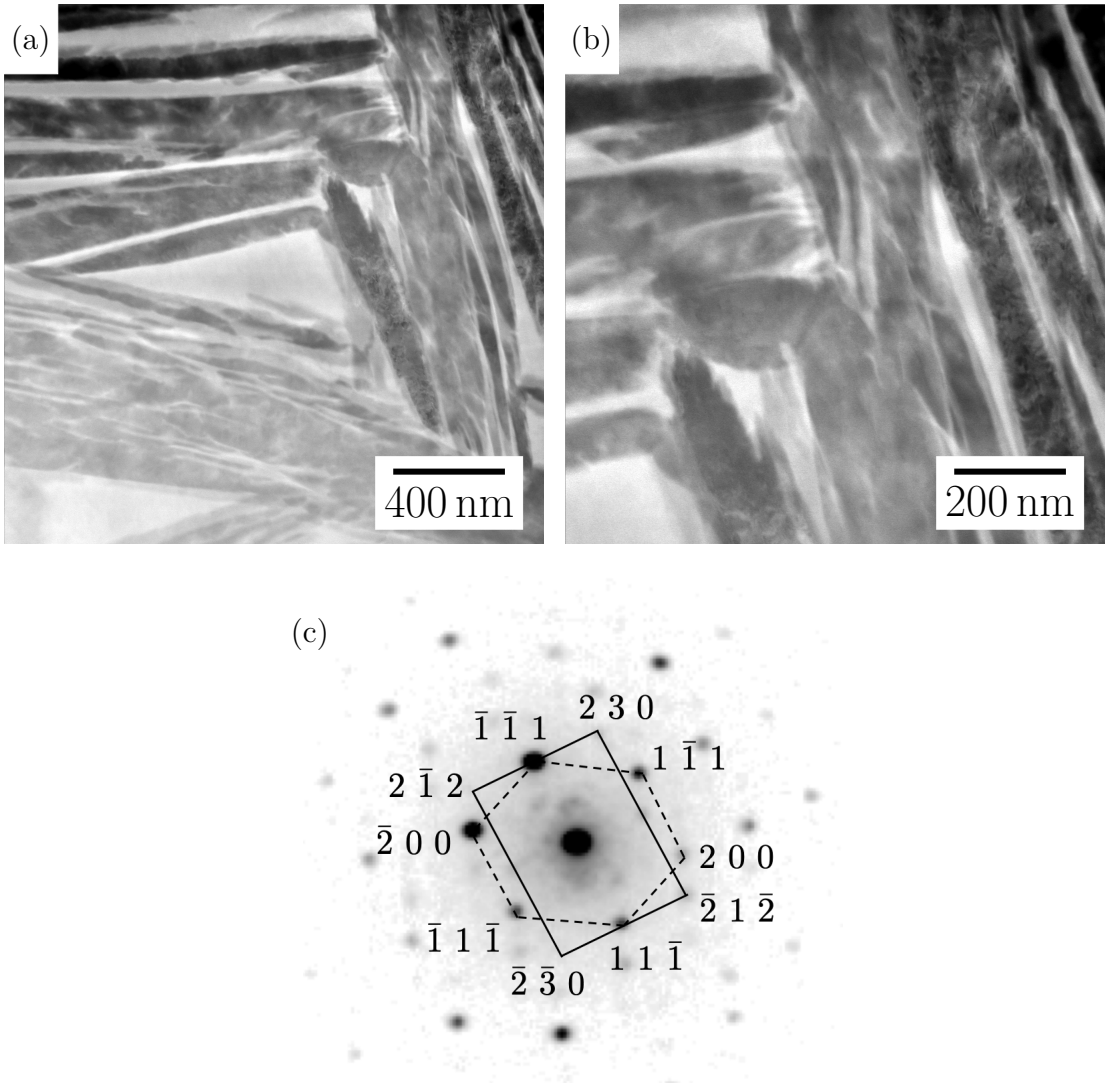


Figure 5.10: STEM dark-field image of Alloy A as transformed. (a) Showing the film and blocky austenite following testing at 200 °C. (b) dark field high resolution STEM image. It should be noticed that testing at 200 °C causing particles of cementite to form within the austenite films. (c) Corresponding diffraction pattern.

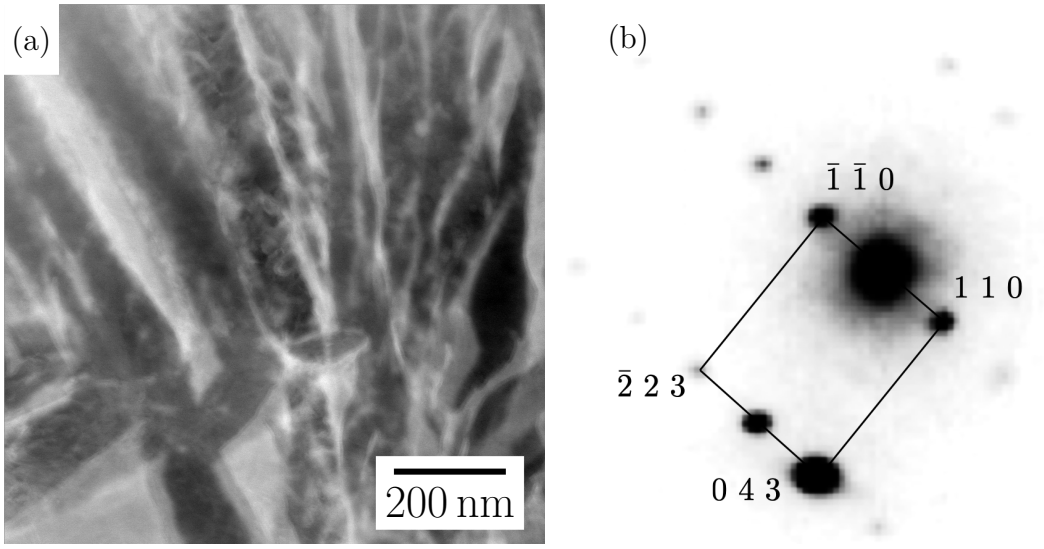


Figure 5.11: STEM dark-field image of Alloy A as transformed. (a) Showing the film and blocky austenite following testing at 450 ℃. (b) Corresponding diffraction pattern of cementite particles .

5.7 Mechanical stability of retained austenite

Martensite is triggered when the chemical free energy change $\Delta G^{\gamma\alpha'} = G^{\alpha'} - G^{\gamma}$ reaches a critical value accompanying the $\Delta G^{\gamma\alpha'}_{M_S}$, in the context of transformation without any composition change [e.g., 152]. The martensite-start temperatures were measured using dilatometery (Figs. 4.7 and 4.9) to be 238 °C and 169 °C, for Alloy A and Alloy B respectively. On combining these measurements with free energy calculations, the critical values of $\Delta G^{\gamma\alpha'}_{M_S}$ are found to be -2511 and -800 J mol^{-1} for Alloys A and B respectively; these will be of use later when analysing the combined effects of undercooling and stress on the evolution of martensite. The simplest way to achieve this given the M_S temperature is to use the Koistinen and Marburger equation [153]:

$$V_V^{\alpha'} = V_r^{\gamma}(1 - \exp\{\beta[M_S - T_Q]\}) \tag{5.1}$$

where $V_V^{\alpha'}$ is the volume fraction of martensite, V_r^{γ} is the volume fraction of retained austenite prior to cooling to a temperature $T_Q \leq M_S$. The coefficient β is empirical and was obtained approximately by fitting the equation to experimental dilatometric-data as shown in Figs. 5.12a and 5.12b.

We now have all the tools in place to estimate the stimulation of martensite by applied stress, which would in the present case increase the martensite-start temperature via the contribution of an additional term $U \approx -0.86 \times \sigma$ to the free energy of transformation, where the stress is expressed in MPa [154, 155]. However, the coefficient 0.86 is for the case where the stress induces the formation of martensite plates that are optimally oriented with respect to the tensile axis. This cannot happen in practice for polycrystalline austenite because the transformation crystallography determines the plate orientation which can only approximately match the optimal orientation. The actual coefficient is expected therefore to be less than 0.86, and was established by fitting to be ≈ 0.75, a value used in subsequent calculations. The net driving force for transformation that accounts for stress at the temperature at which the tensile test is conducted, is therefore given by:

$$\Delta G^{\gamma\alpha'}_{\sigma} = \Delta G^{\gamma\alpha'}_{T} + U \tag{5.2}$$

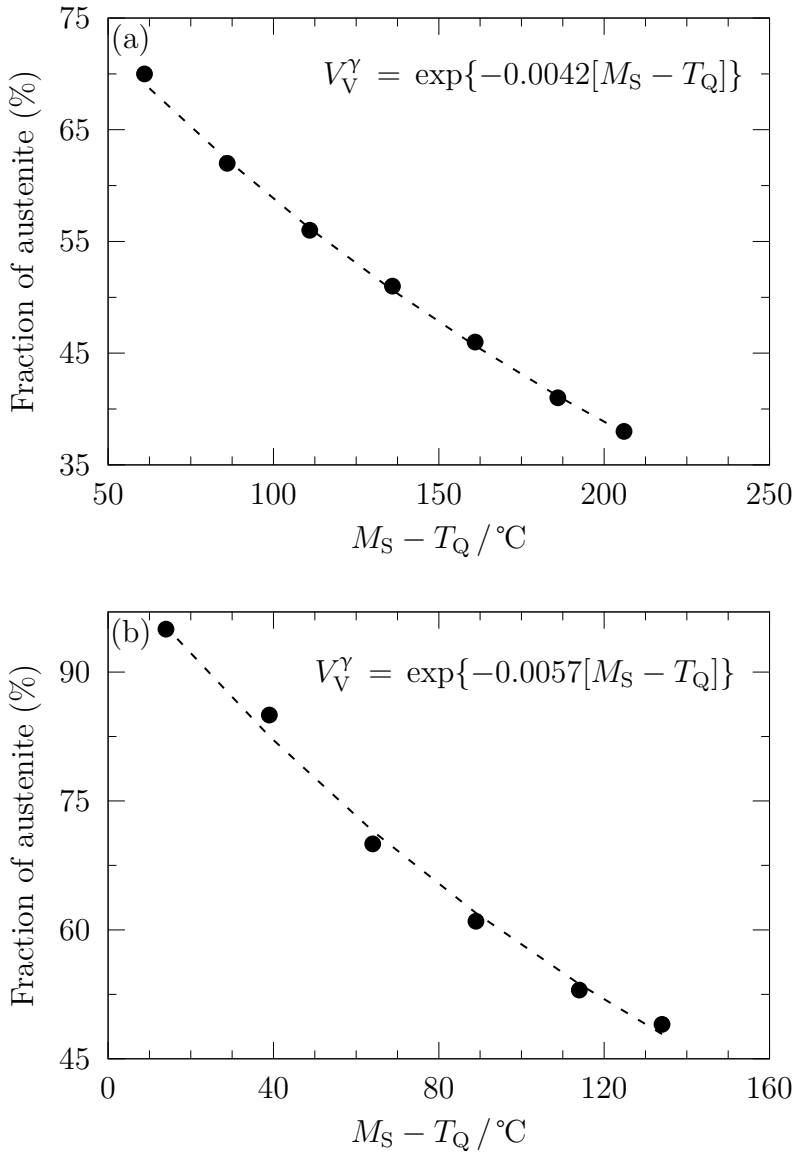


Figure 5.12: Derivation of the Koistinen-Marburger coefficient for (a) Alloy A, (b) Alloy B.

with martensite being triggered when this reaches the critical value $\Delta G_{M_S}^{\gamma\alpha'}$ – this stress-affected M_S temperature can then be used with Eq. 5.1 to calculate the volume fraction of induced martensite.

The results of these calculations are listed in Tables 5.5. Fig. 5.13 illustrates the data, with the curves representing calculated values. In some cases, the amount of martensite that forms at the test temperature is supplemented by that which forms during cooling from that temperature. Note that the strains plotted represent local strains measured on the cross-section of the tensile specimen at that location, where the retained austenite content was also determined. The necked regions therefore are identified with greater strains than recorded over the gauge length of the tensile test specimen.

	Alloy A				Alloy B			
	ϵ	M_S^σ/°C	$V_V^{\alpha'}$ calculated	$V_V^{\alpha'}$ measured	ϵ	M_S^σ/°C	$V_V^{\alpha'}$ calculated	$V_V^{\alpha'}$ measured
	0.000	0	0.000	0.000 ± 0.01	0.000	0	0.000	0.000 ± 0.01
	0.031	73	0.051	0.040 ± 0.01	0.047	188	0.140	0.064 ± 0.02
25°C	0.067	81	0.059	0.045 ± 0.01	0.074	197	0.146	0.067 ± 0.02
	0.150	118	0.092	0.095 ± 0.01	0.161	205	0.150	0.096 ± 0.02
	0.253	274	0.184	0.184 ± 0.04	0.486	323	0.191	0.232 ± 0.03
	0.000	0	0.000	0.000 ± 0.01	0.000	0	0.000	0.000 ± 0.01
	0.074	237	0.167	0.179 ± 0.01	0.233	212	0.153	0.136 ± 0.02
200°C	0.112	274	0.181	0.195 ± 0.01	0.257	231	0.160	0.155 ± 0.02
	0.131	301	0.194	0.200 ± 0.01	0.314	307	0.187	0.214 ± 0.02
	0.165	329	0.204	0.257 ± 0.03	0.404	326	0.192	0.238 ± 0.03
	0.000	0	0.000	0.000 ± 0.01	0.000	0	0.000	0.000 ± 0.01
	0.186	227	0.162	0.190 ± 0.01	0.086	177	0.135	0.085 ± 0.02
450°C	0.318	261	0.178	0.205 ± 0.01	0.179	207	0.151	0.123 ± 0.02
	0.609	302	0.195	0.210 ± 0.01	0.450	282	0.179	0.161 ± 0.02
	0.799	352	0.212	0.215 ± 0.03	0.844	590	0.224	0.259 ± 0.04

Table 5.5: Calculated and measured fractions of martensite following deformation at the temperatures indicated. Note that ϵ refers to the *local* plastic strain at which the retained austenite content was determined in order to deduce $V_V^{\alpha'}$.

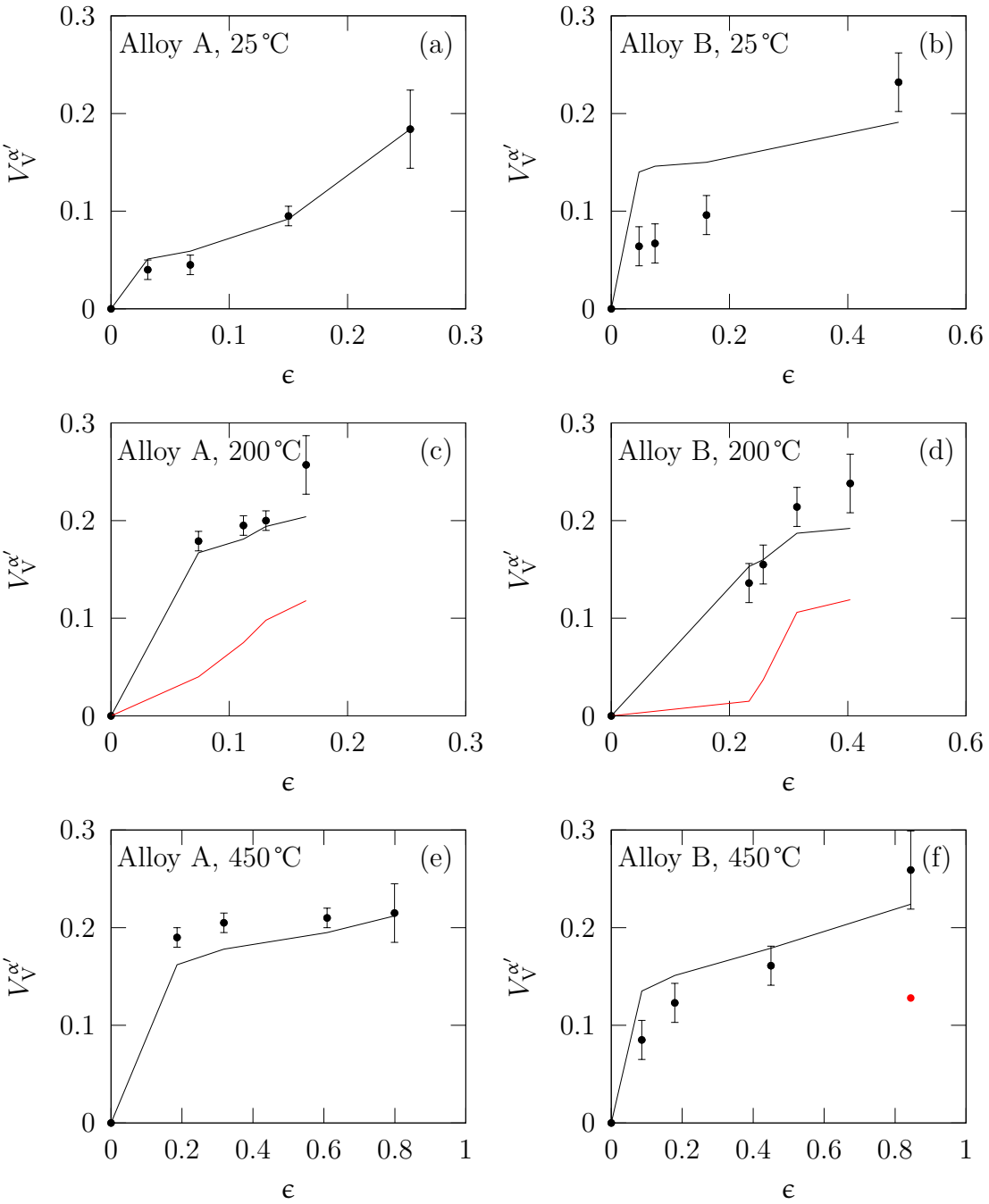


Figure 5.13: Calculated volume fraction of martensite. In (c and d), the red curves represent the amount of martensite that forms at the test temperature and the darker curves include that which also forms during cooling from the test temperature. In (f) there is only one circumstance (red point) where martensite forms at the tensile test temperature, when the strain is greatest.

5.8 Conclusions

The steels studied here were designed originally for thermal stability, i.e., any austenite retained following partial transformation to bainitic ferrite should be maintained at reasonably high temperature. Whereas there are many studies on the deformation-induced transformation of austenite into martensite, the alloys studied here have revealed some unusual behaviour, partly because of their rich chemical compositions but also because tensile tests were conducted at a variety of temperatures.

- Testing at ambient temperature resulted in tensile curves that are typical of very strong materials. There was, however, limited ductility, given the strength levels observed which are well in excess of 1.5 GPa.

- Surprisingly, tensile testing at 200 °C led not only to an increase in strength but at the same time, a remarkable increase in ductility for both alloys.

  When the temperature is raised, the thermodynamic stability of the austenite increases, which should make it more difficult to obtain martensite. Previous work on δ – TRIP steel [151], which is designed for low-strength applications (about 70% allotriomorphic ferrite, 15% bainitic ferrite and the residue retained austenite) has demonstrated that the ductility decreases by testing at 100 °C because the austenite then does not transform, in which case the work hardening capacity due to the TRIP effect is lost. The present work demonstrates the opposite tendency, albeit for completely different steels, that an increase in the test temperature has led to an increase in strength and an increase in ductility, especially, uniform ductility.

  The explanation for the present observation is that although the thermodynamic stability of the austenite in the microstructure has definitely been increased at 200 °C, it still transforms into martensite during deformation. However, the marginal stability allows it to transform in a more gradual manner so that plastic instability is delayed, leading to the simultaneous in-

crease in strength and ductility. It is well known [1], that the austenite must have an optimum stability to martensitic transformation if necking is to be delayed. It seems that at room temperature, in both the alloys studied, it transforms too rapidly.

- When testing the structure at 450 ℃, there is a dramatic collapse in the uniform ductility due to the rapid onset of plastic instability. This is because the austenite no longer is able to transform into martensite during the course of the testing at 450 ℃. In Alloy B, an additional austenite formed at 450 ℃, as proven by dilatometric and hardness data. The austenite then becomes unstable to transformation during cooling to ambient temperature, leading to hardening in the deformed region. It is important to note that this hardening is not due to transformation during deformation. The results are quite exciting because the alloy systems studied have been proven to be ideal for examining the tensile behaviour as a function of the stability of the austenite.

  The results presented here may be the first demonstration that if the austenite is unable to transform at all as in Alloy B then there is a dramatic drop in the ductility and strength of the material of the microstructure which is a mixture of bainitic ferrite and austenite.

Chapter 6

Bainite with intermetallic-compound

The driving force for the bainite transformation is affected by the solute content of the parent austenite. Elements in solid solution, such as manganese, chromium, molybdenum and vanadium [156, 157] reduce the difference in free energy between the austenite and ferrite, and hence delay its transformation. The effect of elements that are in solid solution is essentially on the relative thermodynamic stabilities of the austenite and ferrite. However, precipitates in a variety of scenarios, can alter the kinetics by providing heterogeneous nucleation sites or by depleting the matrix [156, 158–165].

In steels where there is a substantial concentration of nickel and aluminium, it is possible during heat treatments at temperatures above 500 ℃ to precipitate NiAl in the austenite [166–168]. Past investigations have dealt primarily with its precipitation in martensite or ferrite, as methods for enhancing strength [167–171]. Such a steel has recently been developed for elevated temperature service, in which bainite is generated at a sufficiently high temperature where NiAl may also precipitate ([168], Section 5). Stability at high temperatures is achieved by alloying with a large concentration of nickel which has the well-known austenite stabilising effect, and indeed, allows reversion to austenite if the temperature is

sufficiently high (Section 5.7). The aluminium addition not only is essential for NiAl precipitation, but also greatly retards the precipitation of cementite [172–175], which would in turn cause the austenite to decompose. The purpose of the work presented in this chapter is to study the effect of the NiAl precipitation in austenite on the bainite transformation itself. The transformed steel was then subjected to mechanical tests to establish a structure-property relationship.

6.1 Experimental procedure

The composition of Alloy B investigated is shown in Table 3.1. It was designed to exploit a mixed structure of fine bainitic ferrite embedded in carbon-enriched retained austenite, for a potential jet-engine shaft application. The presence of both nickel and aluminium enable the formation of NiAl intermetallic compound in this alloy. An equilibrium thermodynamic calculation shows that NiAl can form in austenite between 550 °C and 800 °C, Fig. 6.1a. The aim here was to investigate the effect of NiAl precipitation in austenite, on its subsequent transformation into bainite. In order to induce NiAl formation, the austenite was cooled and held at 740 °C. Fig. 6.1b shows the composition of the β-NiAl as a function of temperature.

6.2 Heat treatment

Four separate heat treatments were carried out as illustrated schematically in Fig. 6.2. Heat Treatment – I involved heating the samples at 5 °C s^{-1} to 740 °C, 800 °C, and 850 °C, where they were held for 1 h, followed by cooling to room temperature at the same rate. The purpose was to determine whether the alloy is fully transformed into austenite at the holding temperature. The presence of cementite would reduce the amount of carbon available for the subsequent transformation. The martensite-start temperature M_S was measured beginning with the fully austenitic state cooled at 5 °C s^{-1}.

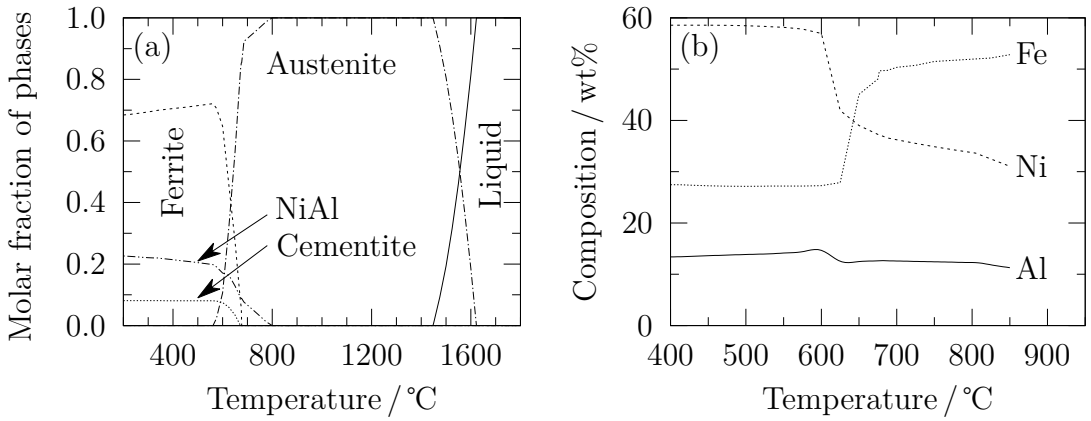


Figure 6.1: Thermodynamic modelling using the software *MatCalc* [176, 177]; with the Fe database version 5.62 to predict (a) stable phase fractions with liquid, austenite, ferrite, cementite and NiAl allowed to exist in the calculations. (b) Composition of the β-NiAl as a function of temperature.

Another heat treatment (Fig. 6.2b) promotes NiAl at 740 ℃, consistent with the calculations in Fig. 6.1a. The treatment illustrated in Fig. 6.2c additionally involves isothermal bainite formation prior to cooling to ambient temperature; Fig. 6.2d is similar to Fig. 6.2c but without the intermediate treatment that precipitates NiAl before the transformation to bainite. The heat treatments implemented on the dilatometer were replicated using a box furnace and fluidised bed on bigger samples for mechanical characterisation.

Transformation temperatures were determined by slope changes in the strain versus temperature dilatometric curve, using the offset method [136]. For comparison with the measured bainite kinetic and martensite-start temperatures, time-transformation-temperature (TTT) as well as both bainite and martensite-start temperatures were calculated using in-house developed algorithms [178, 179].

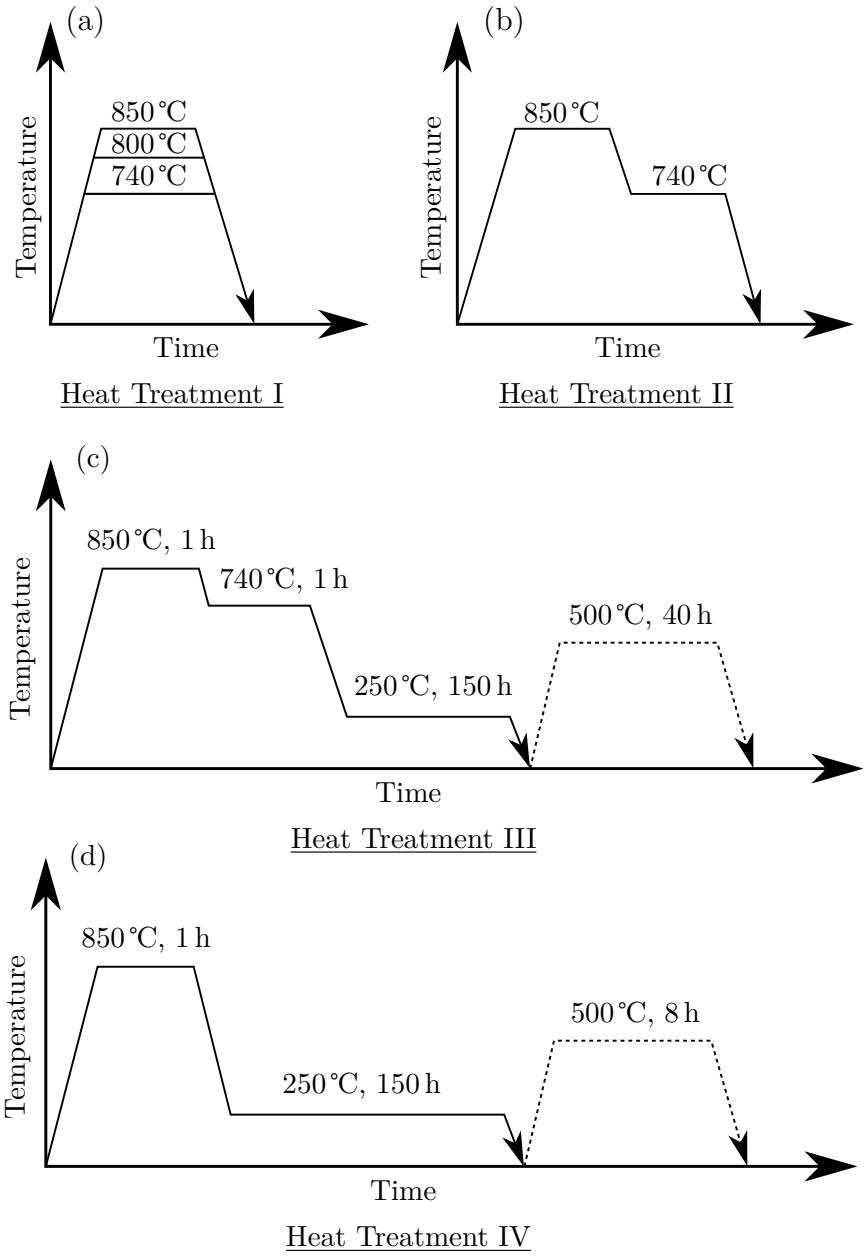


Figure 6.2: Heat treatments carried out using a dilatometer, box furnace and a fluidised bed. Arrows indicate the quench to room temperature using a jet of argon gas or free-air cooling. (a and b) The purpose here was to measure the M_S temperature after austenitisation and to ensure all cementite is dissolved. (c and d) To investigate and compare the effect of NiAl on bainite transformation and on the mechanical properties of this alloy in the as-transformed bainitic and tempered conditions.

6.3 Dilatometry

The dilatometric curve of the as-received martensitic material, Fig. 6.3a, shows two contractions during heating to 850 °C, at ≈ 500 °C and ≈ 700 °C. The first is as the martensite tempers to precipitate cementite. To test this, a sample that was heated to just 600 °C at 5 °C s^{-1} before cooling to ambient temperature, followed by reheating up to 850 °C, which eliminated the contraction as shown in Fig. 6.3b. Metallographic observations confirm the temperature at which the cementite forms, Fig. 6.3c.

The second contraction is due to austenite growth, Fig. 6.3d. The data indicate that the alloy is essentially austenitic at 730 °C, Fig. 6.3d. However, the microstructural evidence suggests otherwise. Fig. 6.4 shows that cementite that forms during reheating is not completely dissolved after holding for 1 h at 740 °C and 800 °C. And indeed, the dilatometry data Fig. 6.5a confirm in a preliminary manner, that the transformation does not reach completion during holding at 740 °C and cementite cannot be fully dissolved at 800 °C. Accordingly, the austenitisation temperature of 850 °C is chosen for subsequent investigations so that austenitisation can be completed before NiAl precipitation. Fig. 6.5b shows that the microstructure after the two austenitisation stages does not contain any cementite particles. Fig. 6.6 shows that M_S is 151 °C for one step austenitisation, and 155 °C for the two-step austenitisation where NiAl formation is stimulated.

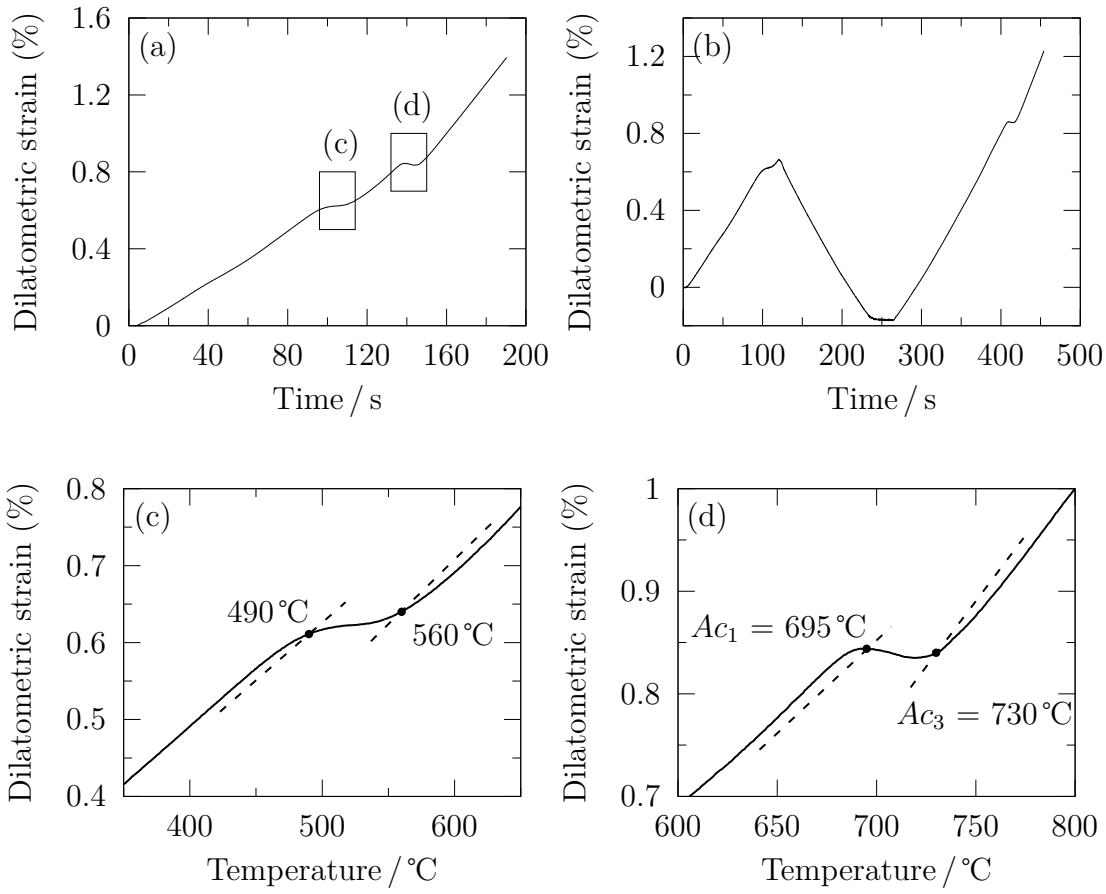


Figure 6.3: Dilatometry curves during heating an initially martensitic microstructure. (a) The fraction of cementite and austenite formation during heating at $5\,℃\,s^{-1}$ to 850 ℃. (b) The cementite contraction disappears during heating the sample at 600 ℃ then reheating to 850 ℃ without holding. (c) Beginning and the end of cementite formation during heating and (d) austenite start and finish temperatures Ac_1 and Ac_3 respectively during heating.

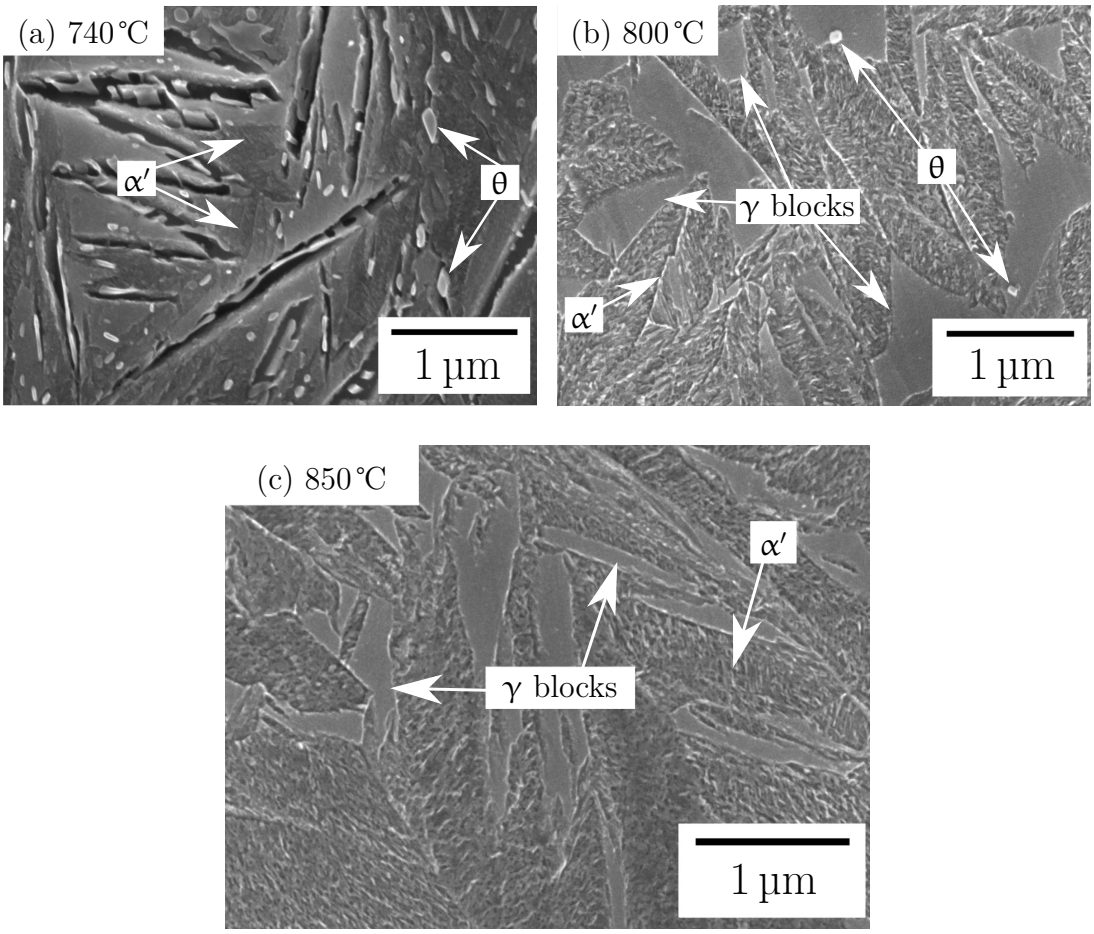


Figure 6.4: Microstructures after austenitisation at temperature indicated according to Heat Treatment I Fig. 6.2a. (a) The structure consists of large martensite plates. (b) Martensite plate and intervening regions of austenite. Cementite not fully dissolved at 740 °C and 800 °C. (c) Martensite plates and austenite grain boundaries. No sign of cementite, which has dissolved when the steel is heated up at 850 °C.

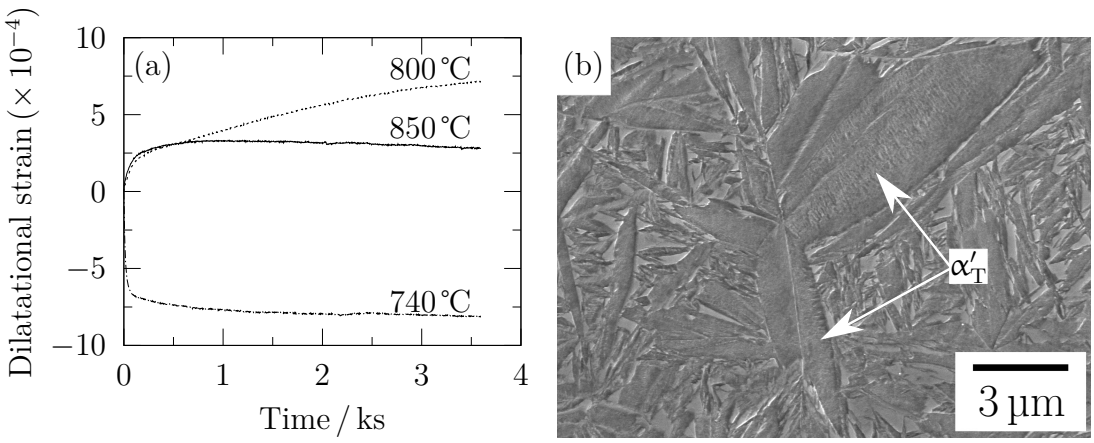


Figure 6.5: (a) Austenite transformation experiments during holding for 1 h at different temperatures as indicated. This alloy is predicted to be completely austenitic at 850 °C; at 800 °C the cementite not fully dissolved, and 740 °C indicates that the austenite transformation does not reach completion. (b) Microstructures after austenitisation according to Heat Treatment II (Fig. 6.2b). Large martensite plates exhibiting twins α'_{T}. No cementite formation after holding at 740 °C.

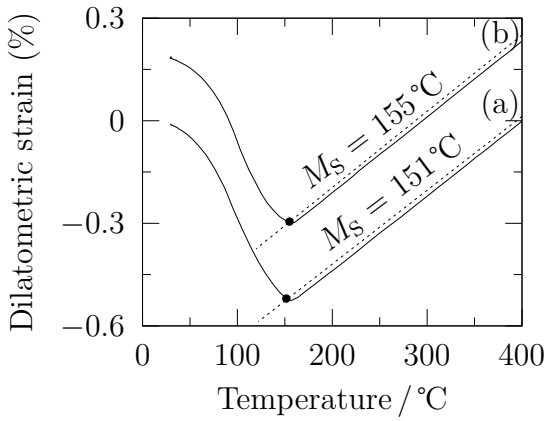


Figure 6.6: Cooling dilatometric curve showing the martensite starting temperature M_{S}. (a) One step austenisation at 850 °C of a period of 1 h. (b) Two step austenisation at 850 °C for 1 h then 740 °C for 1 h where NiAl formation is promoted. Both samples were cooled to room temperature at 5 °C s^{-1}.

6.3.1 Kinetics of the bainite transformation

The effect of NiAl on the bainite transformation kinetics is shown in Fig. 6.7 and some transformation-start times are listed in Table 6.1. The reaction is clearly more rapid in the presence of NiAl precipitates; for example, the difference in the transformation start time (Δt) is 7 h during transformation at 250 °C, Fig. 6.7c. Furthermore, the net amount of bainite obtained is greater when the NiAl is present prior to the bainite transformation.

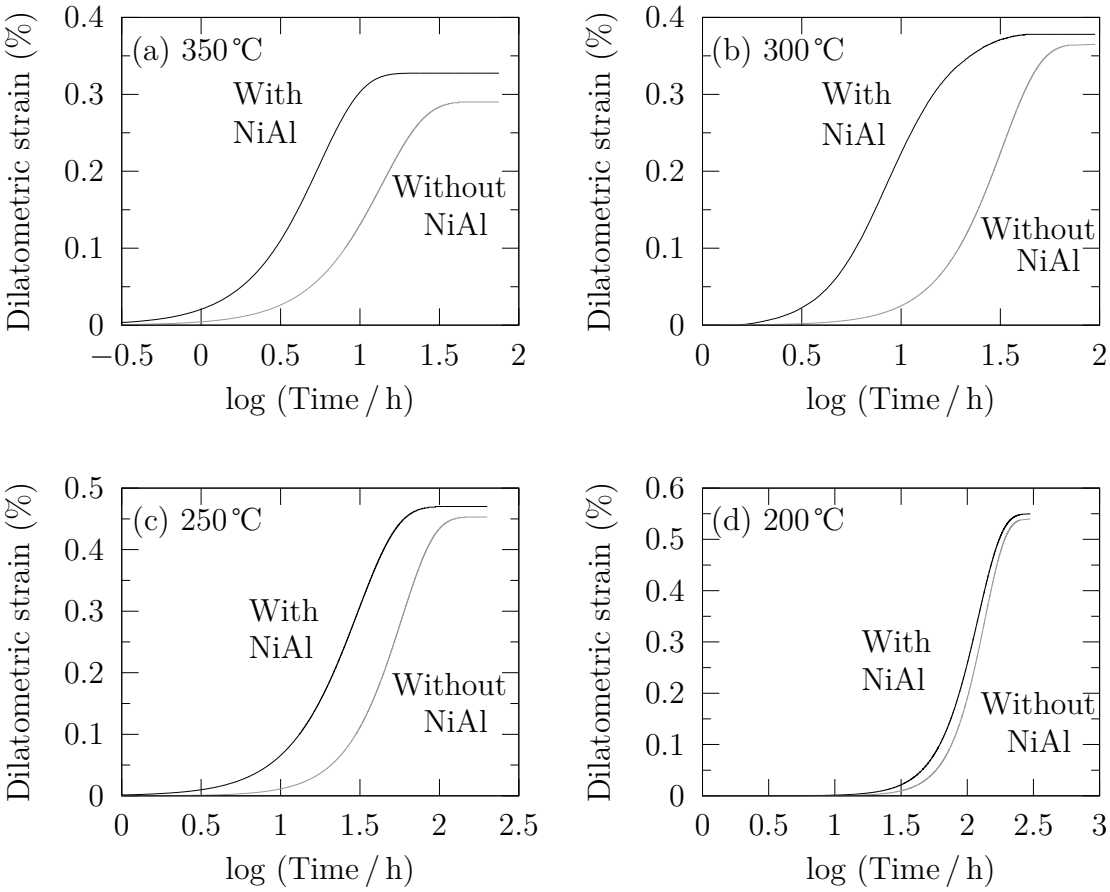


Figure 6.7: Isothermal reaction curves showing that the presence of NiAl not only accelerates transformation but can lead to a greater ultimate quantity of bainite.

Isothermal transformation temperature / ℃	Transformation – start time / h		Δt / h
	With NiAl	Without NiAl	
350	0.9	2.7	1.8
300	2.8	6.3	3.5
250	4	11.5	7.5
200	29	35	6

Table 6.1: The transformation-start time is shorter when the austenite contains NiAl precipitates. "Δt" refers to the difference in transformation-start time between the samples contain NiAl and without NiAl.

A thermodynamic model MTTTDATA (which is a combination of mucg83 and MTDATA thermodynamics database software) has been developed to allow the estimation of isothermal transformation in high alloy steels [134]. Thermodynamic data were retrieved from a database to facilitate kinetic predictions [131]. Fig. 6.9, shows that the transformation-start times obtained experimentally are somewhat shorter than those calculated. Transformation curves on TTT diagrams Fig. 6.10a are consistent with the hypothesis that the difference in the reaction rate peaks at intermediate isothermal transformation temperature. The diffusion of atoms becomes difficult at low temperatures whereas the driving force for transformation is reduced as the temperature is raised. Therefore, the reaction rates are slow both at high temperatures (300 and 350 ℃) and low temperature (200 ℃). Fig. 6.10a shows that the calculated B_S and M_S are higher when the steel contains NiAl before transformation. The chemical composition of the matrix used to investigate the effect of NiAl of the austenite on transformation temperature is obtained from the Matcalc calculation at 740 ℃.

A locus of the T_0 temperature as a function of the carbon concentration is plotted in Fig. 6.9b. This also indicates that a higher amount of bainite transformation is expected in the presence of NiAl, Fig. 6.7. This is because the T_0 curve is shifted to a higher carbon concentration by altering the chemical composition

of the austenite. The presence of NiAl clearly increases the amount of bainite transformation, which helps reduce the blocks of austenite.

Fig. 6.8 shows the dilatometric curve corresponding to $10^{-3}\,℃\,s^{-1}$ cooling rate. It indicates clearly that the bainite starts temperature is higher (460 ℃) when the steel contains NiAl precipitates compared with the one without precipitates (410 ℃).

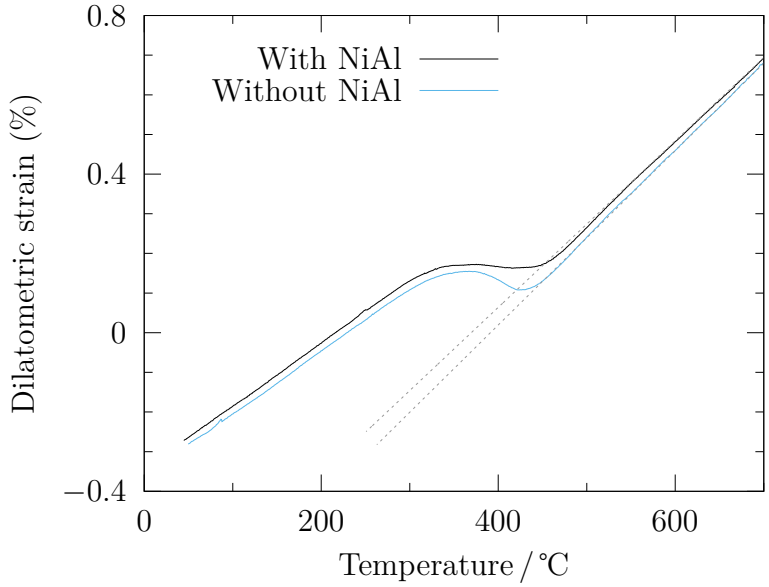


Figure 6.8: Typical dilatometric curve corresponding to $10^{-3}\,℃\,s^{-1}$ cooling rate showing the bainite transformations.

To test whether the primary role of NiAl precipitates is to stimulate nucleation, the apparent lengths of bainite sheaves were measured following partial transformation at 250 ℃ . Fig. 6.10 shows that there is no significant difference with and without the NiAl, confirming that the particles promote transformation by providing heterogeneous nucleation sites.

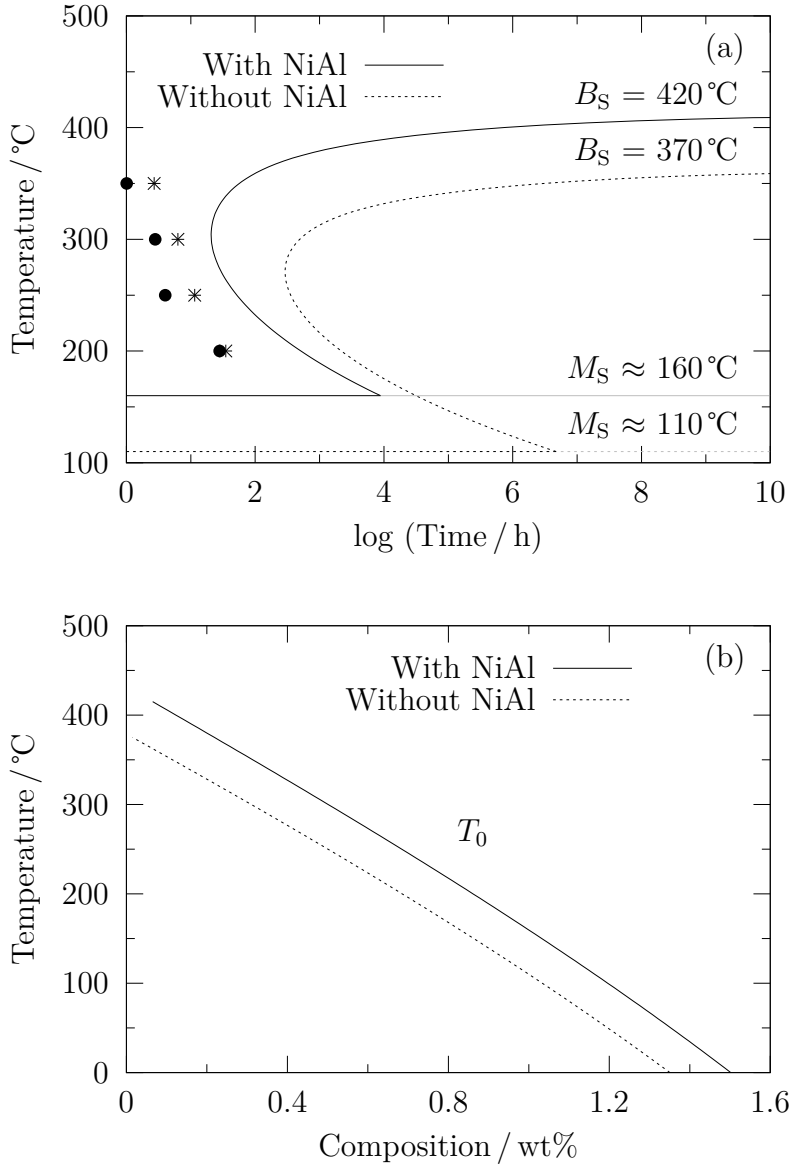


Figure 6.9: (a) TTT curve calculated using MTTTData [134]. Points [•] and [∗] are the bainite transformation start time obtained experimentally with and without NiAl precipitates respectively. (b) T_0 calculated using MTData, larger volume fraction of bainitic ferrite due to the precipitation of NiAl.

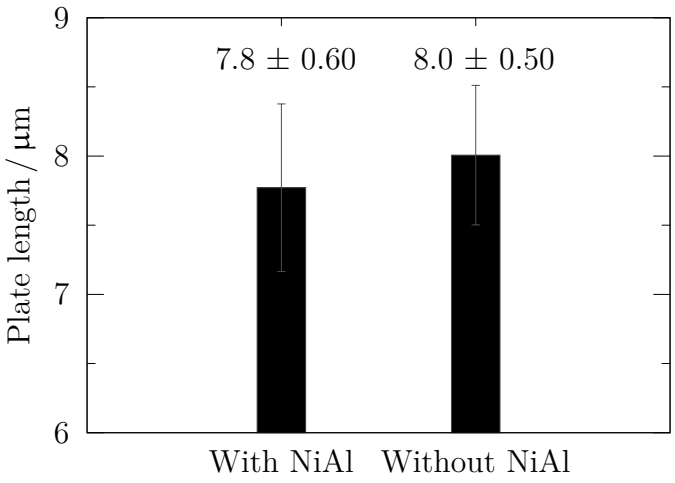


Figure 6.10: The average apparent-length of 100 bainite sheaves. The samples were transformed isothermally at 250 ℃ for 10 h followed by quenching to ambient temperature.

6.4 Deformation of austenite

One-stage uniaxial compression tests were carried out on the austenatic regions generated using the heat treatments described schematically in Fig. 6.11. This involved heating the samples at 5 ℃ s^{-1} to 850 ℃, where they were held for 1 h, followed by cooling to 740 ℃, where they were either deformed immediately (Fig. 6.11a) or held for a certain time before a compression load applied (Figs. 6.11b and 6.11c). The aim here was to study whether additional NiAl would form when sample holds at 740 ℃ for a longer time. Compression schedule with 60 % and a strain rate of 1 s^{-1}.

As expected, holding the samples at 740 ℃ for a longer time before the deformation occurs, stimulate more NiAl. This led to a higher strength as is evident from Fig. 6.12.

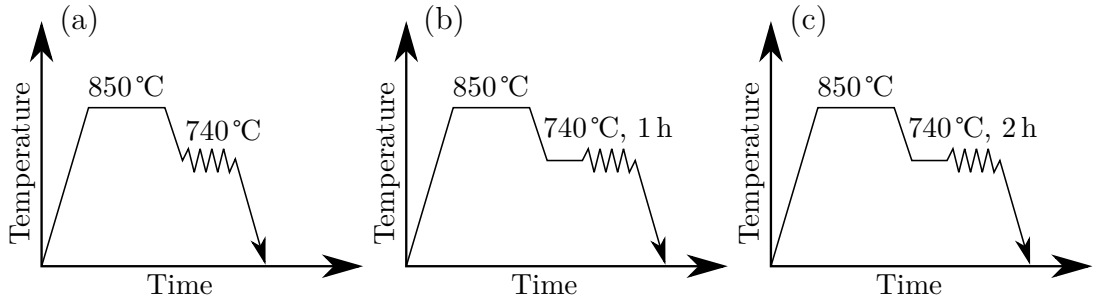


Figure 6.11: Heat treatments carried out using a deformation mode in a dilatometer. (a) Sample deformed immediately at 740 °C without holding; (b) and (c) hold at 740 °C for 1 h and 2 h respectively, followed by deformation.

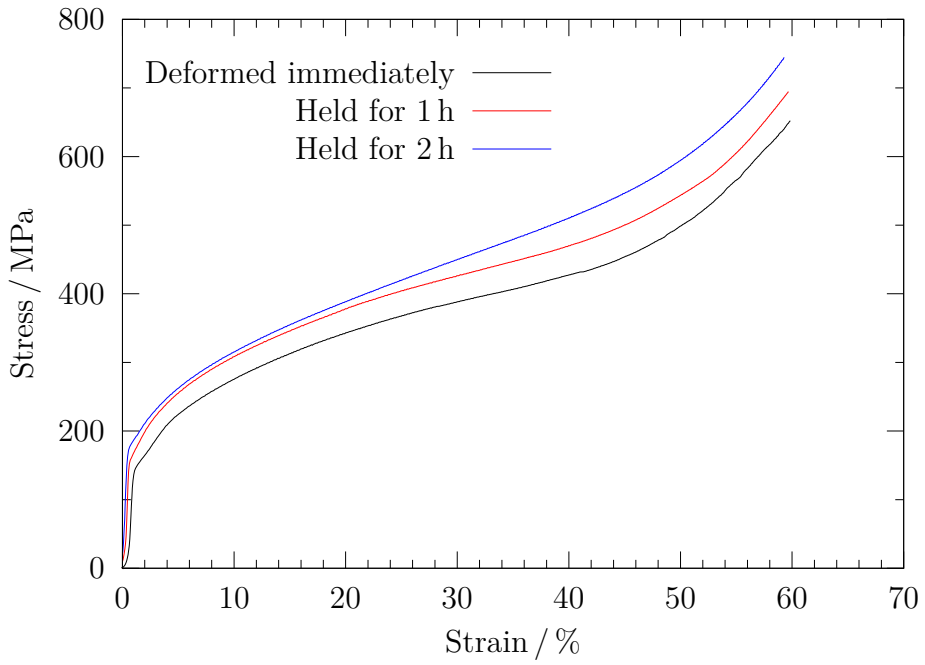


Figure 6.12: Engineering stress-strain curves for uniaxial compression implemented using a dilatometer.

6.5 Microstructural observations

Fig. 6.13 shows microstructural evidence of the greater degree of transformation achieved in the given time, when NiAl precipitates in austenite. Fig. 6.14a shows evidence for the intergranular nucleation of α_b on NiAl, leading to significantly different microstructure compared with austenite grain boundary dominated nucleation (Fig. 6.14b). STEM bright field images in Fig. 6.15 confirm this hypothesis. This also can be observed from the EBSD orientation images in Fig. 6.16, where the NiAl promotes a more chaotic and finer bainite structure compared to the NiAl-free sample. The corresponding pole figures show that the spread in bainite orientations within an individual austenite grain is greater on the sample with prior NiAl precipitation. Greater magnification and EBSD orientation images are provided as in Appendices A and B.

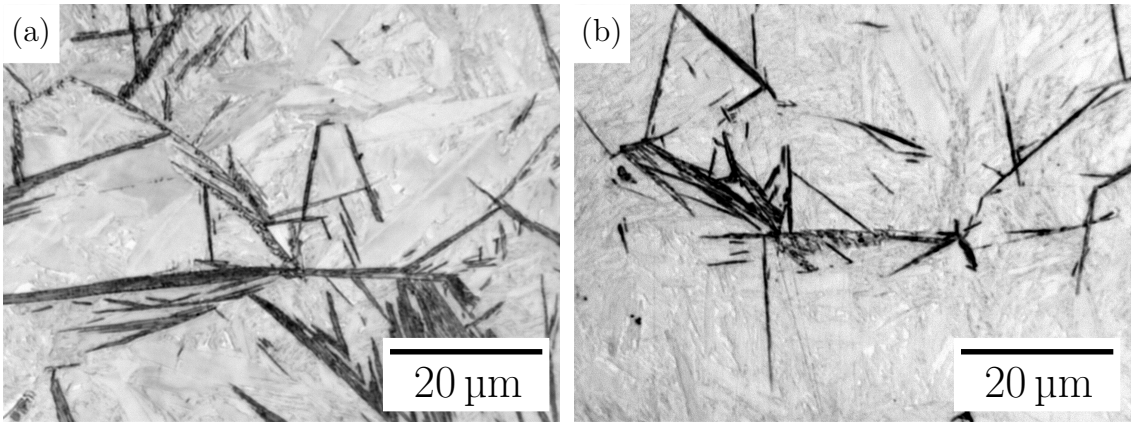


Figure 6.13: Micrographs of partial bainitic transformation at 250 ℃ for 10 h (a) with NiAl. (b) Without NiAl.

The structure consists of austenite and bainite plates with fine precipitates ($\simeq$ 100 nm) of NiAl embedded in the bainite plates (Fig. 6.17). The β-NiAl is confirmed by electron diffraction, Fig. 6.17c, where superlattice reflections are observed due to primitive cubic crystal structure with a motif of Ni at 0, 0, 0 and Al at $\frac{1}{2}$, $\frac{1}{2}$, $\frac{1}{2}$ associated with each lattice point. Energy dispersive spectroscopy confirmed that the fine precipitates are rich in nickel and aluminium Fig. 6.17d.

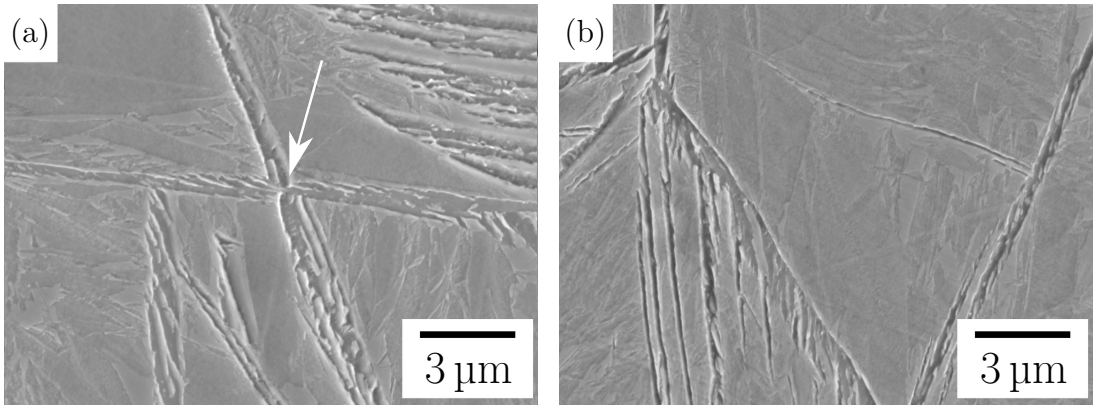


Figure 6.14: SEM of partial bainitic transformation, formed after transformation at 250 °C for 10 h (a) with NiAl. The arrow indicates the intragranular nucleation of bainite from the NiAl precipitates. (b) Without NiAl, nucleation is from the austenite grain boundaries.

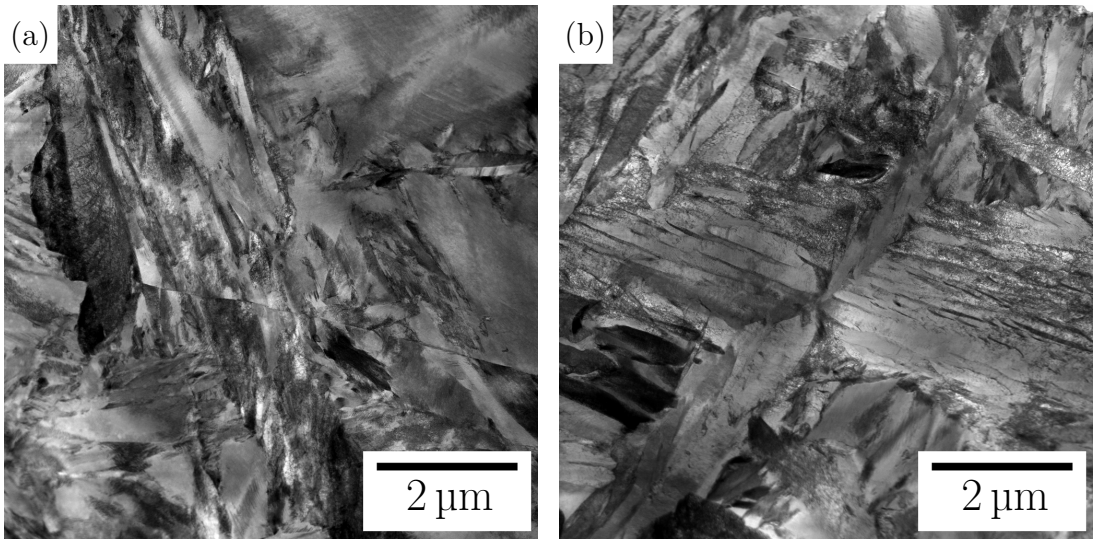


Figure 6.15: STEM bright field images of the transformed alloy. Microstructure of an interrupted bainitic transformation at 250 °C for (a) 10 h. (b) 50 h, (b) shows the the nucleation of bainite from the NiAl precipitates where the bainite is seen to grow into many directions.

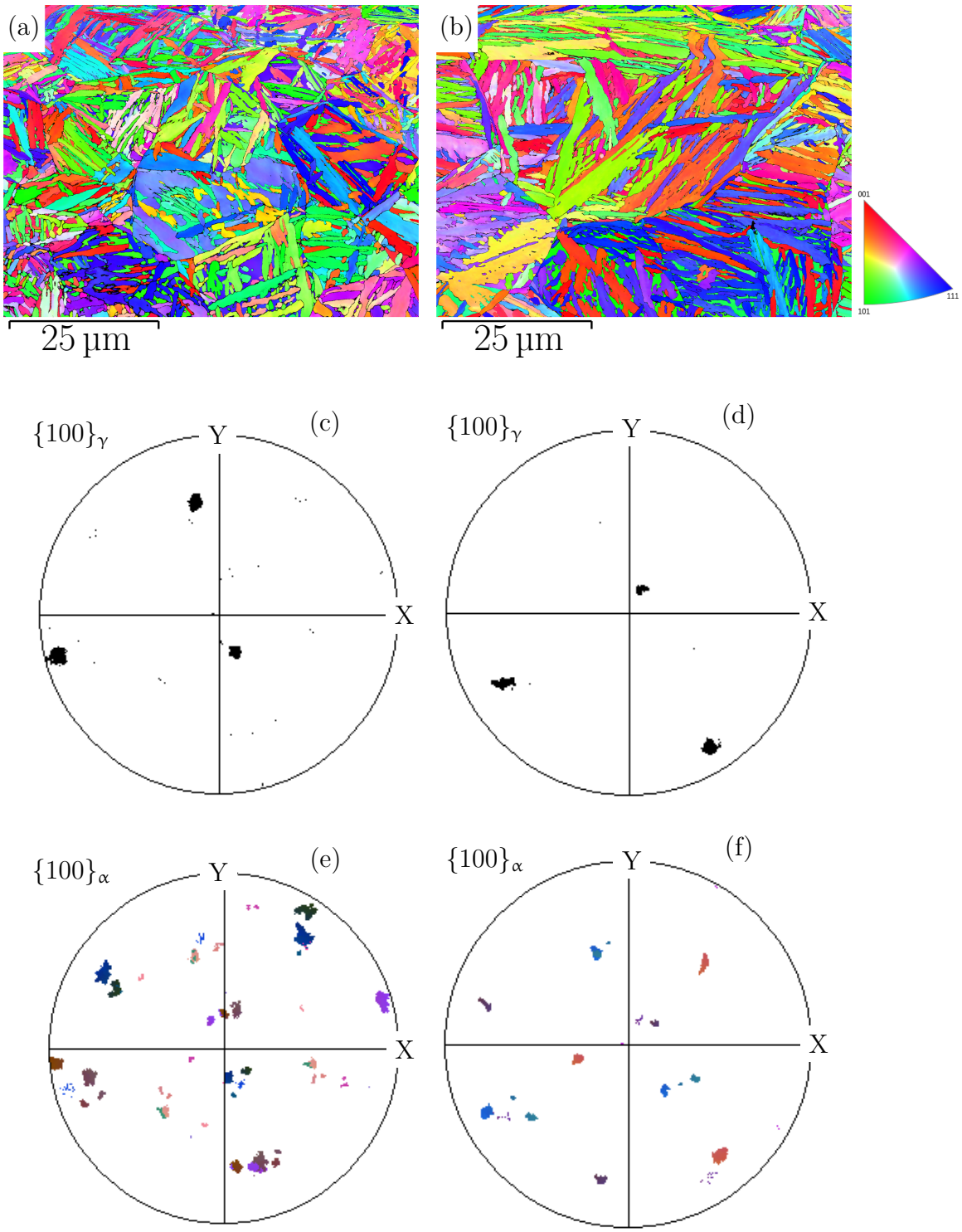


Figure 6.16: EBSD orientation image, sample transformed isothermally at 250 °C for 150 h followed by cooling to ambient temperature. (a) Bainite nucleated from NiAl promotes a more chaotic and finer bainite structure. (b) Grain boundary nucleated bainite. Pole figures from a parent austenite grain, (c and d) $\{100\}_\gamma$ pole figure, (e and f) corresponding $\{100\}_\alpha$ pole figure, more variants within the austenite grain (e).

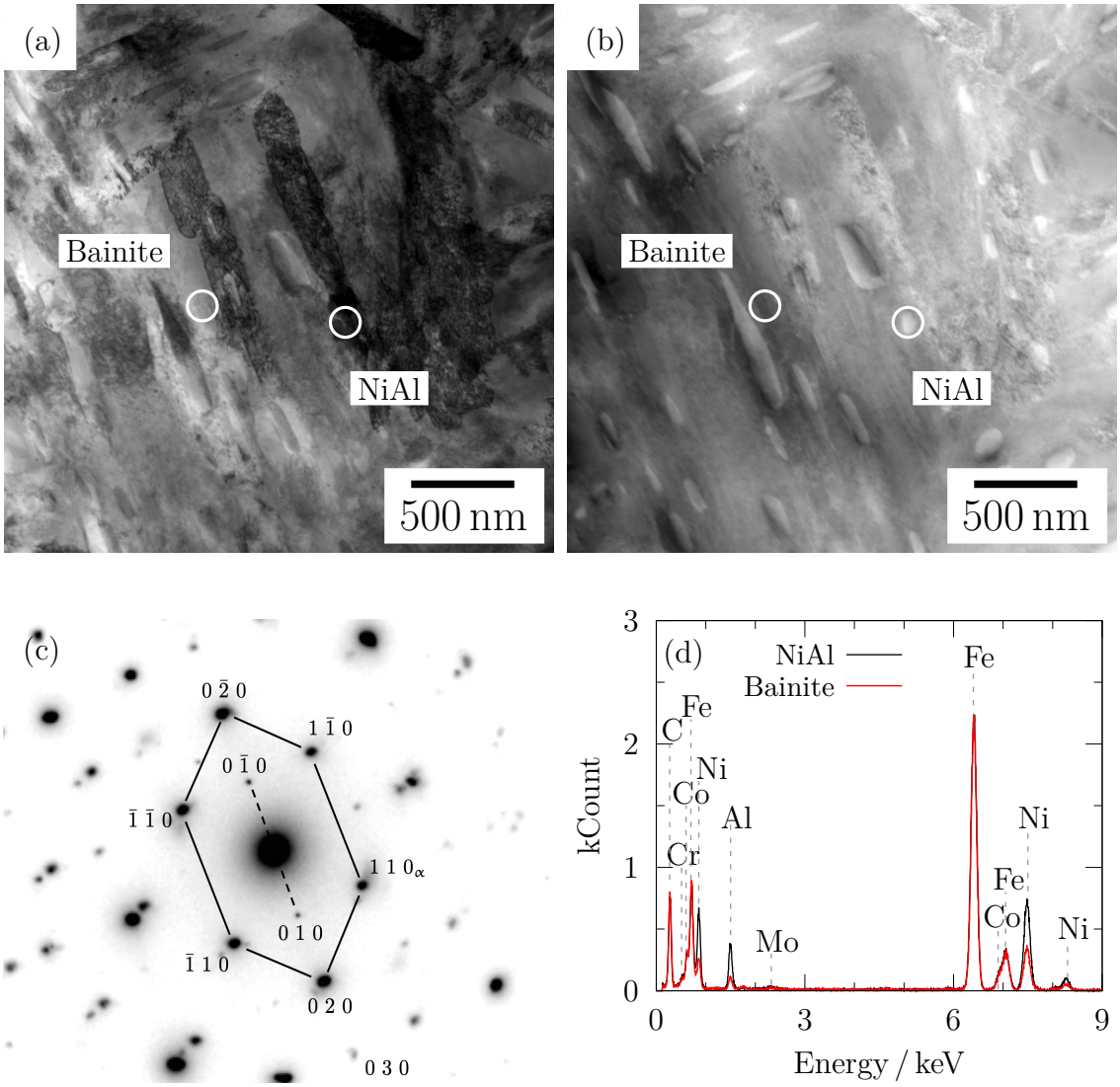


Figure 6.17: STEM bright field image transformed isothermally at 250 °C for 150 h followed by cooling to ambient temperature. (a) Microstructure of austenite and bainitic ferrite plates with fine precipitates of NiAl embedded in the latter. (b) Corresponding dark HAADF STEM image elliptical γ' inclusion can be seen (light). Highlighted area used for EDS point scanning. (c) Corresponding superimposed electron diffraction pattern from $[001]_\alpha$ matrix and γ'. The α matrix and γ' are, as expected, in cube-cube orientation. (d) EDS from the marked region showing enriched regions of aluminium and nickel in areas containing precipitates.

6.6 Hardness measurements

Vickers hardness tests as a function of fraction of the bainite were performed on dilatometric heat-treated samples as shown in Fig. 6.18, together with the measured phase fractions. The hardness (660 ± 6HV) of the as-quenched microstructure is greater when NiAl precipitates are present compared with the sample without precipitates (594 ± 4HV) Figs. 6.18a and 6.18b, with the amount of martensite being identical in both cases. This indicates that the increase in hardness is due to the formation of NiAl.

With interrupted bainitic transformation, there are trends with regards to the hardness obtained. Fig. 6.18a shows that alloy without NiAl, the measured hardness slightly peaks as the fraction of martensite decreases. As the amount of bainite increases, so does the carbon concentration of the austenite; therefore, the hardness of any martensite that forms subsequently also increases resulting in the peak. However, when sufficient bainite formed (Fig. 6.18c) this effect diminishes because the austenite tends to be retained. Similar effects have been observed previously [119].

6.7 Mechanical properties

6.7.1 Toughness

All measured fracture toughness values are given in Table 6.2. The sample containing NiAl precipitates exhibits a toughness significantly higher $\approx 15\%$ than the one without prior precipitates, and it is so tough that valid measurements of K_{Ic} were not possible. This also can be seen from Fig. 6.19a, where the as-transformed sample containing NiAl precipitates exposed higher load and greater crack opening displacement compared with NiAl free sample Fig. 6.19c. Charpy tests in (Table 6.2) confirmed these trends.

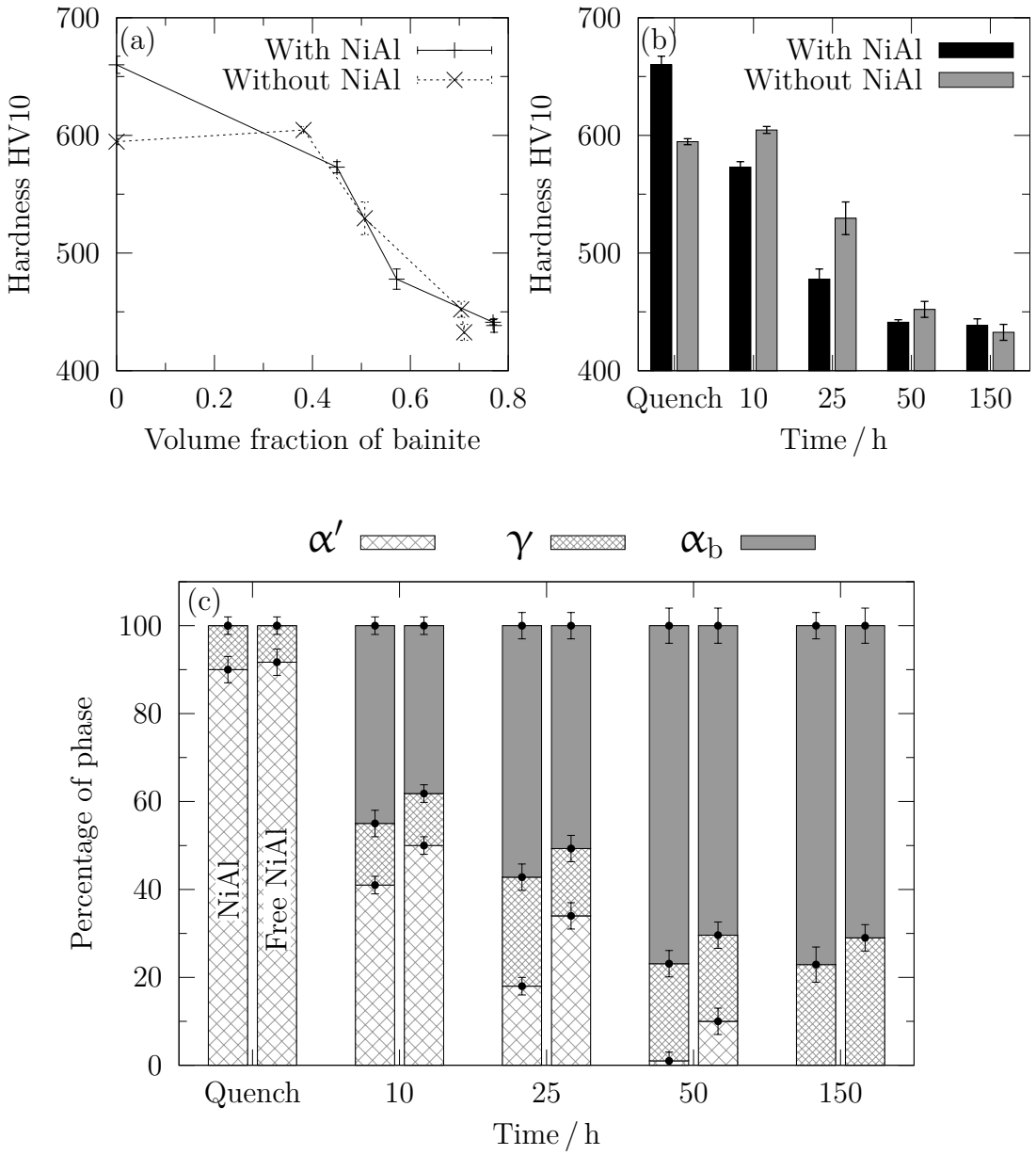


Figure 6.18: Vickers hardness as a function of (a) volume fraction of bainite transformed isothermally at 250 °C. (b) time. (c) Phase fractions determined using cooling dilatometric curves along with the X-ray data. 'Quench' samples represent the hardness of a mixture of martensite and austenite obtained by quenching from a fully austenitic state. Isothermal interrupted tests at 10, 25 and 50 h to fully bainitic microstructures at 150 h.

The fracture toughness values of the tempered bainite (with and without NiAl) are identical. This is because the exposure time has been chosen where both samples achieved the highest hardness value of $\approx 607\,\mathrm{HV}$ (Figs. 6.2c and 6.2d). This can be seen from (Figs. 6.19b and 6.19d), where both samples experienced equivalent applied load. The fracture toughness values for the tempered samples containing NiAl and NiAl free are $\approx 18\,\mathrm{MPa\,m^{\frac{1}{2}}}$, close to that of conventional nanostructured steels in the as-transformed condition [76, 96, 180]. Fractographs of fracture toughness and Charpy impact tests images are presented as supplemental data (D).

Alloy with NiAl	Temper	K_{Q} / $\mathrm{MPa\,m^{\frac{1}{2}}}$	K_{Ic} / $\mathrm{MPa\,m^{\frac{1}{2}}}$	Impact energy / J
✓	×	70.9		32.5
	✓	18		2.7
×	×		60.1	22.4
	✓	18.2		2.7

Table 6.2: Fracture toughness and Charpy impact results measured at ambient temperature in bainitic and tempered samples according to heat treatment shown in Fig. 6.2.

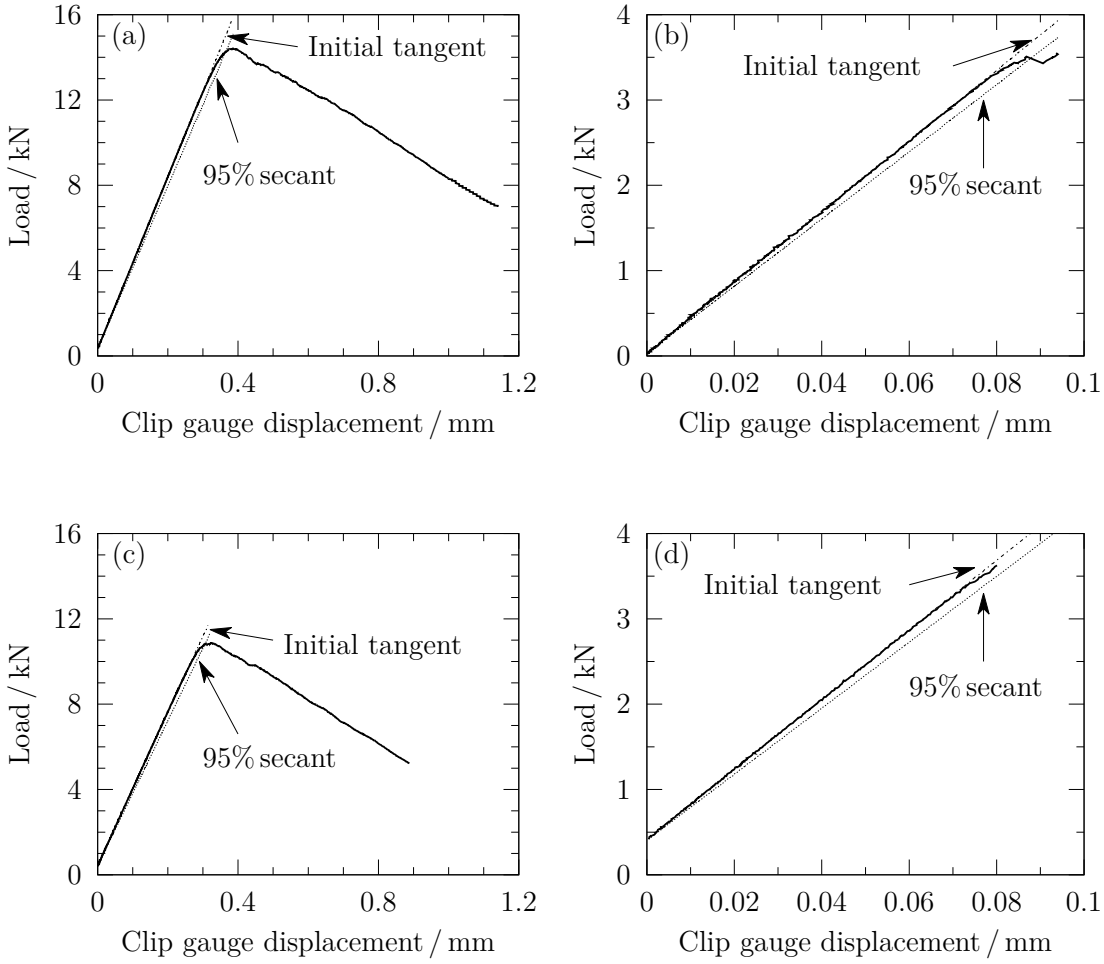


Figure 6.19: Load versus crack opening displacement used in fracture toughness testing recorded for: (a and b) with prior NiAl precipitation in as-transformed and tempered conditions respectively, (c and d) without prior NiAl precipitation in as-transformed and tempered conditions respectively.

6.7.2 Tensile properties

Room-temperature tensile tests were performed in the as-transformed bainitic and tempered conditions. The resulting engineering stress–strain curves are presented in Fig. 6.20, with derived parameters summarised in Table 6.3. The samples containing NiAl precipitates are slightly stronger than those without NiAl pre-

cipitation in the as-transformed bainitic condition. It is evident that both microstructures can accommodate significant plastic deformation before failure. A hardness comparison (Fig. 6.21) of the grip, gauge and fracture regions, shows that alloy contains NiAl samples tested at room temperature hardened slightly when compared with alloy without prior precipitation of the intermetallic particles.

The retained austenite is optimally stable during the tensile test consistent with the observed *increase* in the carbon concentration (Table 6.4) in the alloy contain NiAl. This also can be observed clearly from (Fig. 6.9b) where T_0 curve is shifted to a higher carbon concentration. Furthermore, the steel without prior NiAl precipitates shows a *decrease* in the carbon concentration of the retained austenite in the unstressed gauge section, making the austenite less stable to martensitic transformation. Tempering at 500 ℃ also increases the 0.2% proof stress and ultimate tensile strength of both cases, consistent with the transformation of austenite to the less-ductile ferrite and the precipitation of cementite.

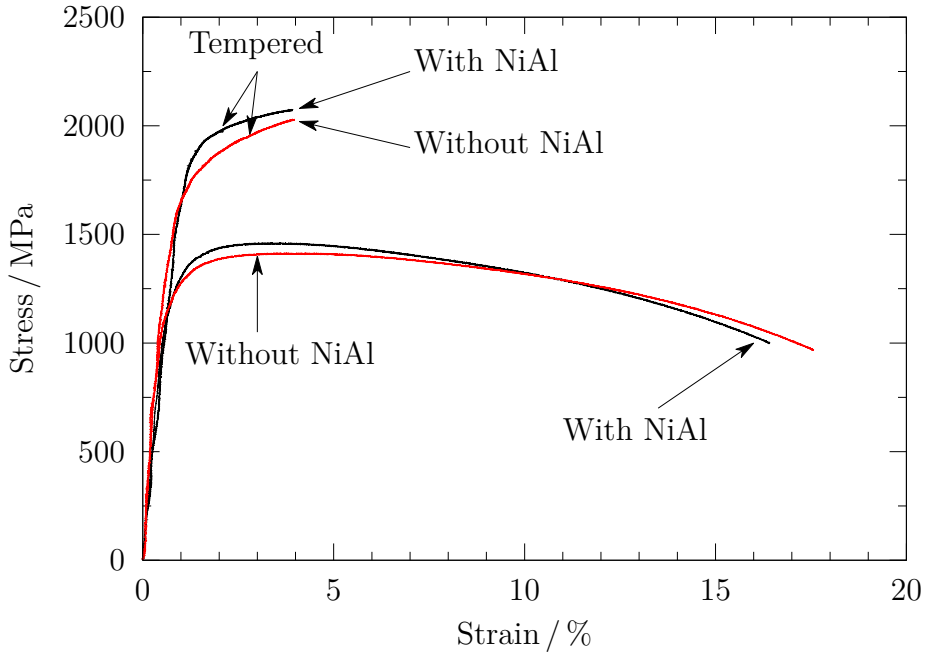


Figure 6.20: Engineering stress-strain curves measured during tensile tests for as-transformed and tempered conditions at ambient temperature.

Alloy with NiAl	Temper	E GPa	0.2% σ_{PS} MPa	σ_{UTS} MPa	ε_U %	ε_T %	ε_A %
✓	×	182	1245	1487	4.0	16.4	59.8
	✓	187	1767	2073	4.0	4.0	4.2
×	×	181	1123	1412	4.0	17.6	61.7
	✓	178	1508	2029	4.0	4.0	3.7

Table 6.3: Tensile test results for as-transformed and tempered conditions tested at ambient temperature. All tests performed at a constant crosshead speed of $0.002\,\mathrm{mm\,min^{-1}}$. σ_{PS} and σ_{UTS} are the proof and ultimate tensile strengths respectively, ε_U & ε_T are the uniform and total elongations respectively, and ε_A is the reduction of area.

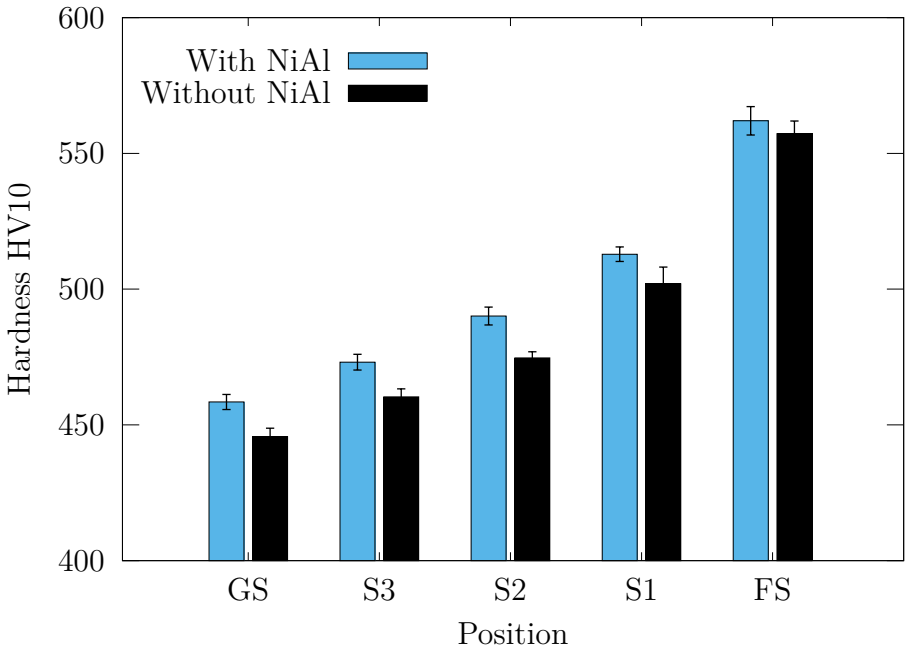


Figure 6.21: Measured Vickers hardness of tensile test samples, using a 10 kg load. NiAl precipitates cause the alloy to hardened slightly compared with the free NiAl alloy.

Alloy with NiAl	Section	V_γ	a_γ / Å	C_γ / wt%
	FS	0.11 ± 0.02	3.6404 ± 0.0041	1.49 ± 0.02
	S1	0.18 ± 0.01	3.6354 ± 0.0031	1.34 ± 0.02
✓	S2	0.24 ± 0.02	3.6302 ± 0.0031	1.18 ± 0.01
	S3	0.25 ± 0.01	3.6292 ± 0.0029	1.15 ± 0.01
	GS	0.26 ± 0.02	3.6285 ± 0.0022	1.13 ± 0.01
	FS	0.16 ± 0.02	3.6349 ± 0.0035	1.33 ± 0.02
	S1	0.20 ± 0.01	3.6321 ± 0.0030	1.24 ± 0.02
×	S2	0.26 ± 0.01	3.6255 ± 0.0028	1.04 ± 0.01
	S3	0.27 ± 0.01	3.6241 ± 0.0023	1.00 ± 0.01
	GS	0.28 ± 0.01	3.6235 ± 0.0021	0.98 ± 0.01

Table 6.4: Diffraction data for both set of alloys tested at the ambient temperature. FS represents the fracture surface and GS is the undeformed area, (S1-S3) gauge sections as shown in Fig. 3.1. V_γ and C_γ stands for volume fraction and carbon content of austenite respectively and a_γ is the austenite lattice parameter.

6.8 Fractograph

Fractographs of both heat treated conditions (with and without NiAl prior bainite transformation) of tensile test samples tested in the as-transformed condition show broad ductile cleavage (Figs. 6.22 and 6.23). Nonetheless, both alloys do not induce a huge change in fracture mode, and show obvious necking and a lot of dimples, indicating a characteristic mode of a ductile fracture. This is expected with the higher ultimate tensile strength of both steel Table. 6.3, which delays final fracture until cracks expend an extensive range of the cross-sectional area. What is more, alloy without prior NiAl precipitates exhibits mixed fracture mode, with cleavage features detectable in areas generally comprising of dimpled rupture or intergranular fracture (Fig. 6.23b). As it has been stated before, aluminium is essential to accelerate transformation and suppress cementite, however, aluminium is a strong nitride forming element. Since an amount of 2 ppm nitrogen is presence in the alloy, aluminium nitride phase forms and appears as inclusions after the solidification of the steel Fig. 6.24. The fracture mode of both alloys changes after tempering, areas of intergranular failure with large cracks and many fine voids (Figs. 6.25 and 6.26) appeared, proposing a decrease in ductility and toughness Table. 6.3. Fractographs of fracture toughness and Charpy impact tests images are provided in Appendix C.

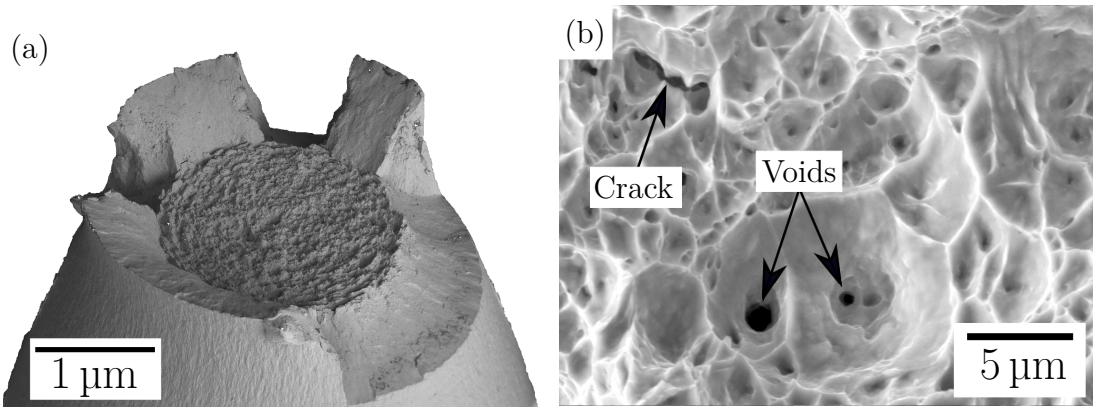


Figure 6.22: Scanning electron micrographs of the tensile test fracture surfaces for alloy contains NiAl precipitates in the as-transformed condition (a) low magnification obtained at 45 °; (b) high magnification. Sample exhibits extensive ductile cleavage.

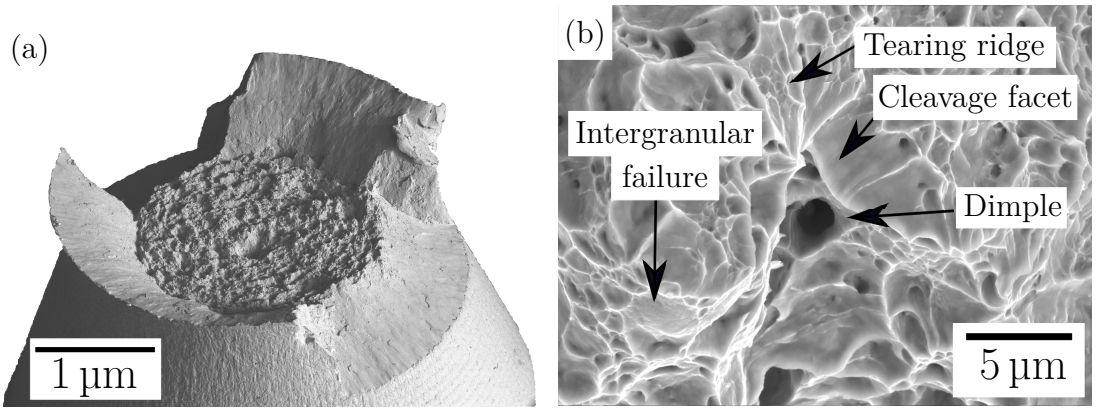


Figure 6.23: Scanning electron micrographs of the tensile test fracture surfaces for alloy without prior NiAl precipitates in the as-transformed condition (a) low magnification obtained at 45 °; (b) high magnification. Sample exhibits extensive ductile cleavage.

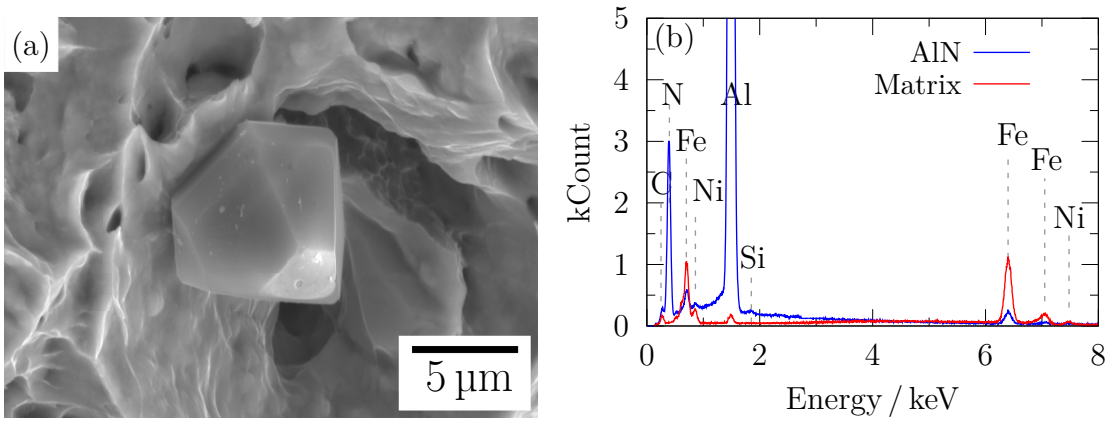


Figure 6.24: (a) Typical SEM micrographs showing hexagonal symmetry of aluminum nitride "AlN" precipitates and (b) corresponding EDX pattern displays the presence of aluminium and nitrogen in the hexagonal crystal structure.

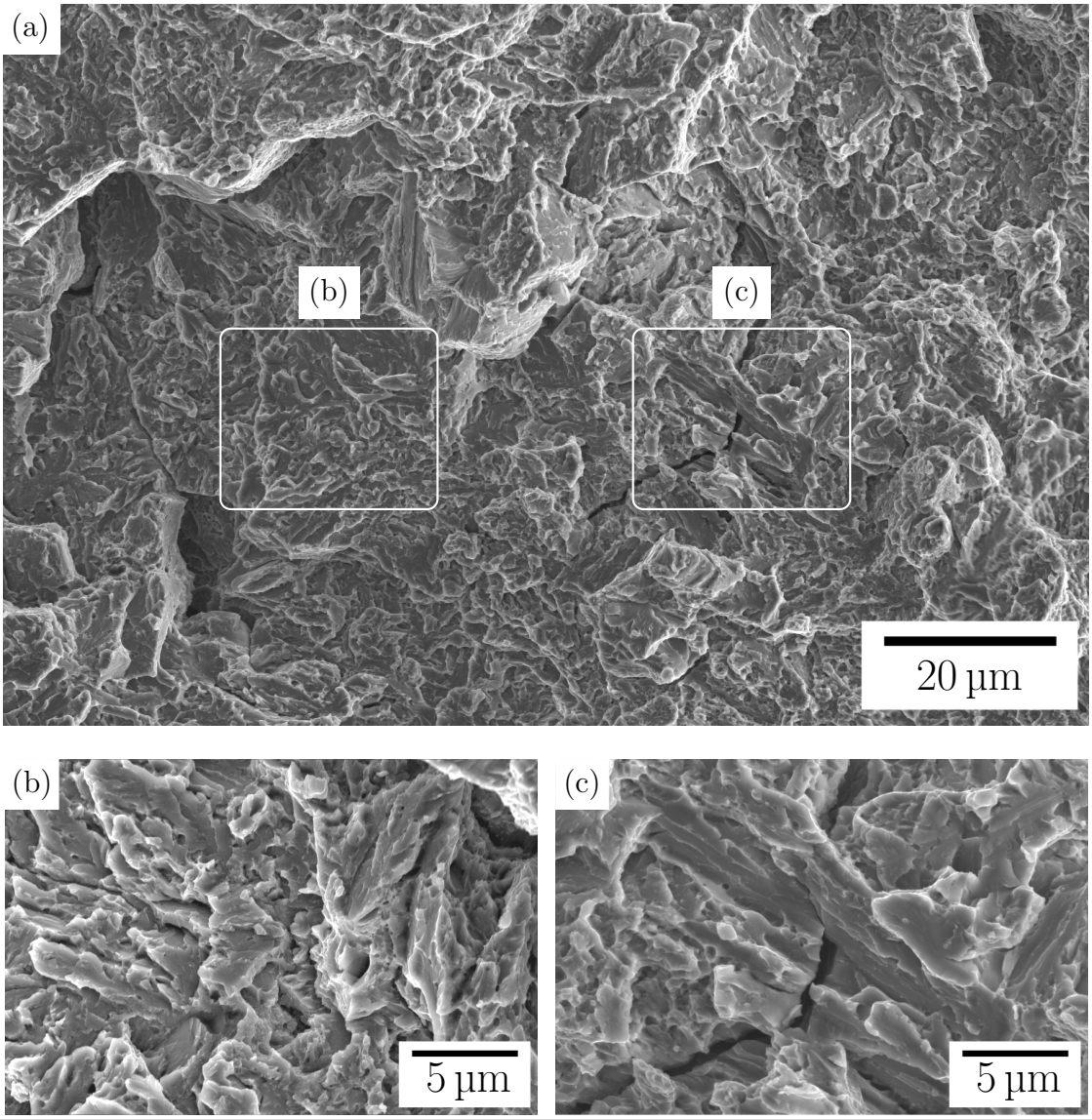


Figure 6.25: Scanning electron micrographs following tensile testing at ambient temperature in the tempered alloy contains NiAl precipitates indicates brittle failure revealing the quasi-cleavage facets and intergranular cracks, together with few voids.

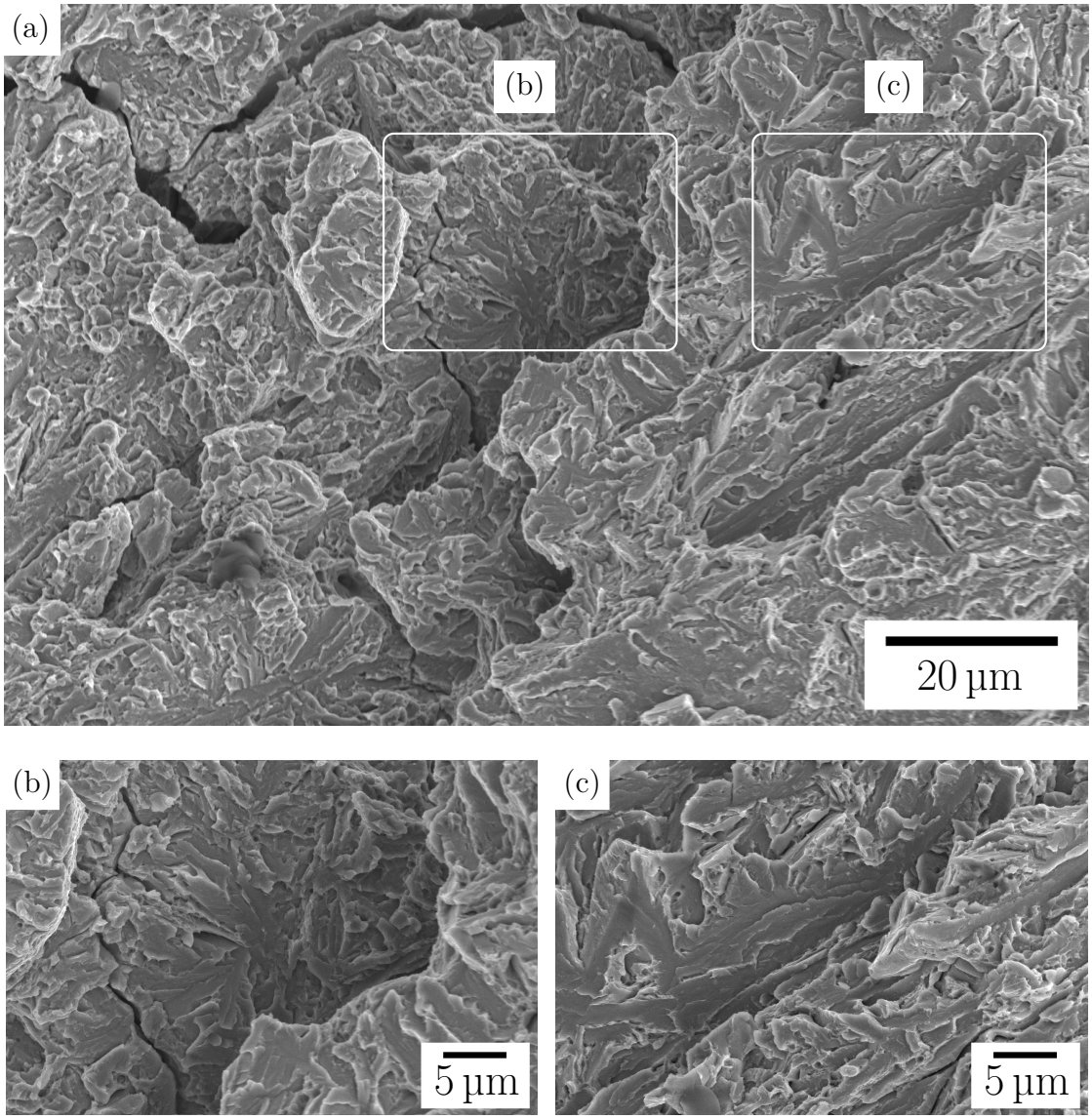


Figure 6.26: Scanning electron micrographs of the fracture surface of the tempered sample without prior NiAl precipitates after tensile testing at ambient temperature indicate the quasi-cleavage facets and intergranular cracks.

6.9 Conclusions

All of the experimental results indicate that the formation of NiAl in the austenite accelerated the subsequent transformation to bainite. Since the sheaf length does not change significantly in the presence or absence of NiAl, it can be concluded that NiAl promotes the heterogeneous nucleation of bainite. This is because the acceleration of the bainite reaction in the presence of NiAl change the chemical composition of the austenite matrix. This also results in an increase in the amount of bainite which has the consequence of reducing the coarse regions of retained austenite. All of these factors lead to greater strength and toughness in the NiAl containing samples.

Conclusions & future work

In steels, there is a temperature regime where none of the atoms can diffuse during the course of transformation from undercooled austenite. The change in crystal structure on transformation is, therefore, achieved by a homogeneous deformation of the lattice. The transformation of austenite into bainite falls in this regime of limited atomic mobility so the plates of bainite grow without diffusion, but carbon can redistribute or precipitate shortly after transformation. A major consequence of this displacive mechanism is that the transformation product is in the form of thin plates, a natural mechanism of grain refinement that does not require any thermomechanical processing. This makes the bainitic steels strong and tough, provided that cementite precipitation is avoided.

The two steels studied here were designed originally for thermal stability, i.e., any austenite retained following partial transformation to bainitic ferrite should be maintained at reasonably high temperatures. Whereas there are many studies on the deformation-induced transformation of austenite into martensite, the alloys studied here have revealed some unusual behaviour, partly because of their rich chemical compositions but also because tensile tests were conducted at a variety of temperatures.

One of the alloys featured a high concentration of silicon (Alloy A) and the other a large nickel, aluminium and a lower carbon contents than existing nanostructured steels (Alloy B). Surprisingly, the alloys are found to have greater ultimate tensile strengths and ductility when tested at 200 °C, compared with corresponding tests at ambient temperature. This is demonstrated to be a consequence of the more gradual deformation-induced transformation of the retained austenite at

200 ℃. In contrast, there is a dramatic reduction in both strength and uniform ductility during testing at 450 ℃. Some carbides precipitate during testing of the high-silicon alloy, thus making the austenite less stable to both thermally and mechanically, this temperature is much higher than in "conventional" nanostructured steels. The high-nickel alloy suffers from the same fate but for different reasons, that the austenite actually grows at the 450 ℃ test temperature, leading to a reduction in its thermodynamic stability. The experimental data on the stability of the retained austenite both at the test temperature and during cooling was studied systematically and modelled mathematically to demonstrate the different kinds of behaviour that occur when mechanical properties are measured at temperature.

In another example, It is demonstrated that the nickel aluminide precipitation lead to an increase in the kinetics of the bainite either by depleting the parent phase from certain solutes, or by inducing the intragranular nucleation of bainitic ferrite. Furthermore, their presence increases the total quantity of bainite that forms, thus helping to reduce the scale of the austenite retained in the final microstructure. There is therefore, an increase in the fracture and impact toughnesses without sacrificing the strength.

The main outcome of this work is a new understanding of the thermal stability of high silicon or high nickel bulk nanostructured bainitic steel. Furthermore, it is now possible to specify the optimal stability of the austenite in the nanostructure in order to achieve the best combinations of mechanical properties.

Future work

Both alloys and the principles outlined in this thesis represent a significant advance in nanostructured bainitic steels that have greater thermal stability when compared with the original concept. More work is needed before these alloys can be used for high-temperature engineering applications:

- Further thermal stability investigations might focus on the effects of repeated heating and cooling. This may lead to interesting outcomes, possibly by influencing the distribution of solutes or through a recovery of internal stresses.
- The properties might be improved further by controlling the austenite grain size. For example, the inclusion of aluminium nitride into Alloy B, may provide grain boundary pining and may lead to improved toughness.
- A detailed investigation of the fatigue and creep properties could reveal interesting phenomena, especially for the case where some austenite growth occurs at relatively low temperatures.
- It would be interesting to discover a way of adjusting the lattice parameter of the intermetallic compound "NiAl" so that it can match with that of the matrix. In this way it may be possible to apply this material to elevated temperature applications. The matching will then ensure that the precipitates do not coarsen at the elevated service temperature, and yet are able to resist deformation because their structure is chemically ordered. The unique feature of this concept is that the matrix in which the precipitates are dispersed itself has a nanostructure. Intermetallic compounds can be found in other alloys for example stainless steels containing aluminium they are not particularly strong because the matrix has relatively coarse grains.
- It would be interesting to study the potential effect of the matrix in comparison with the retained austenite during tensile testing at ambient and elevated temperatures. This may lead to further understanding of thermal stability in terms of the changes in the proportion and texture of the parent and the product phases [181].

Appendix A

SEM micrographs of Alloy B

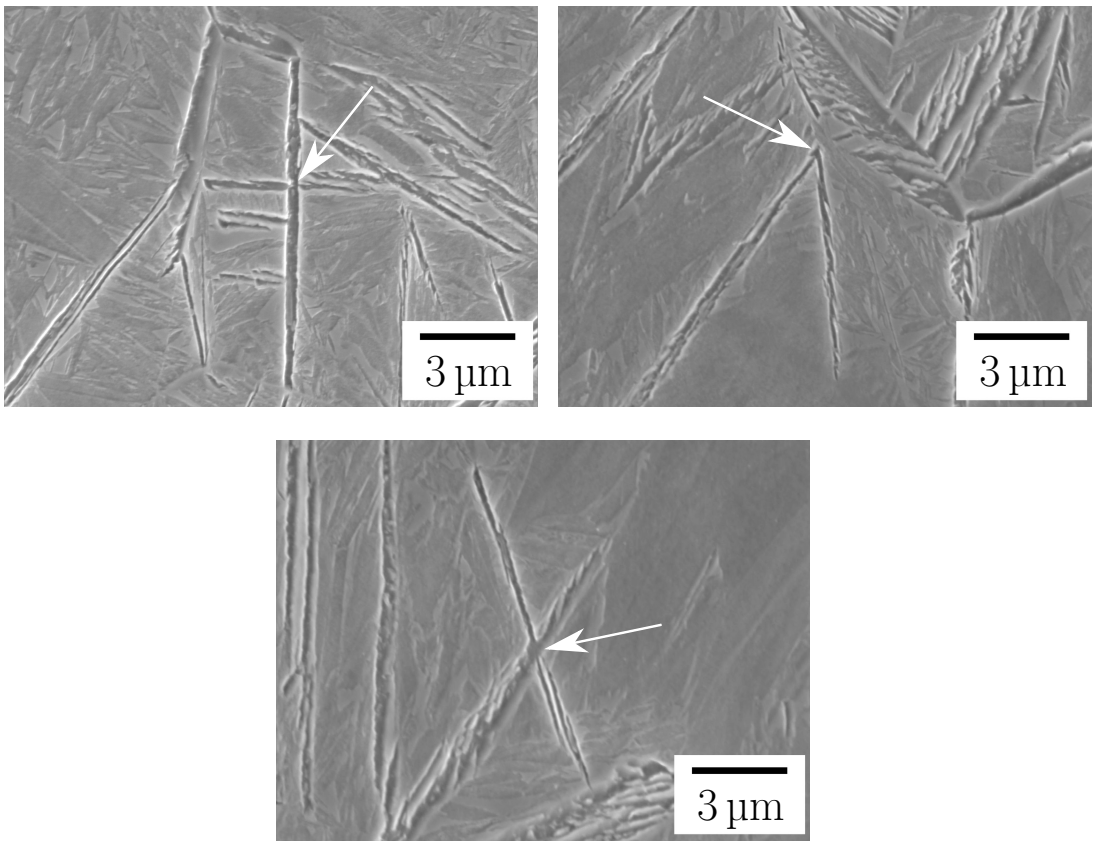


Figure A.1: Scanning electron microscopy (SEM) micrographs of Alloy B, formed after austenitisation and interrupted bainitic transformation at 250 °C for 10 h to observe the nucleation from the precipitates. Arrows indicate the nucleate of bainite from the NiAl precipitates.

Appendix B

EBSD orientation images of Alloy B

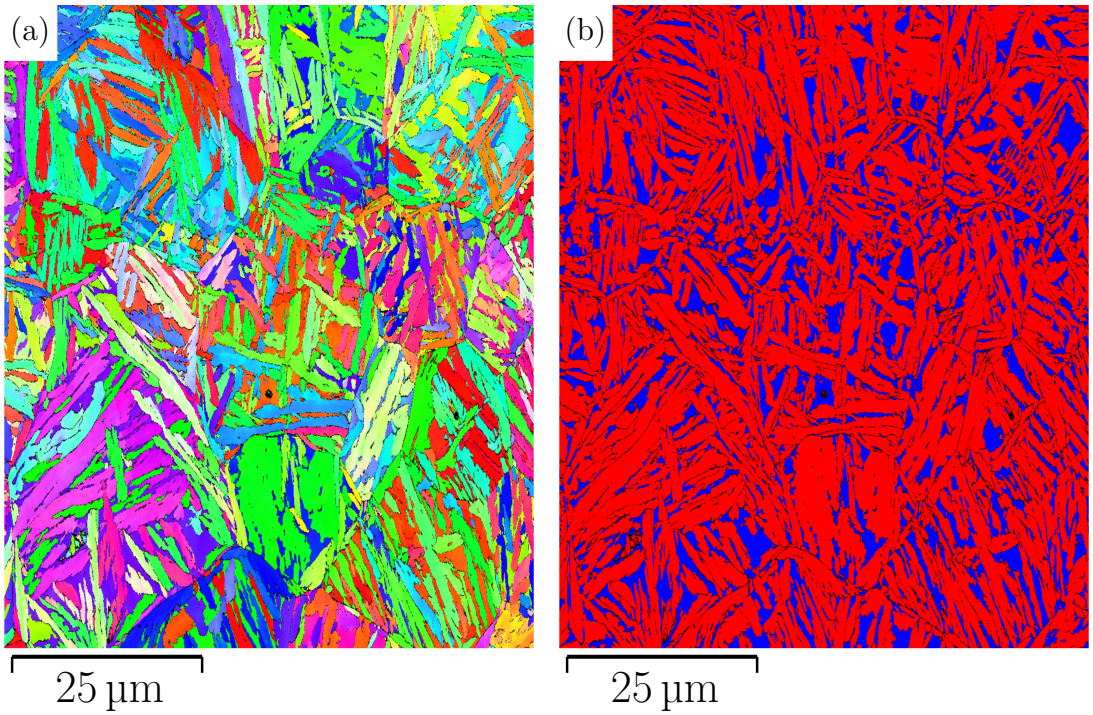


Figure B.1: EBSD orientation image, sample transformed isothermally at 250 °C for 150 h followed by cooling to ambient temperature. (a) Bainite nucleated from NiAl promotes a more chaotic distribution of plates. (b) Distribution of retained austenite (blue) and bainitic ferrite (red).

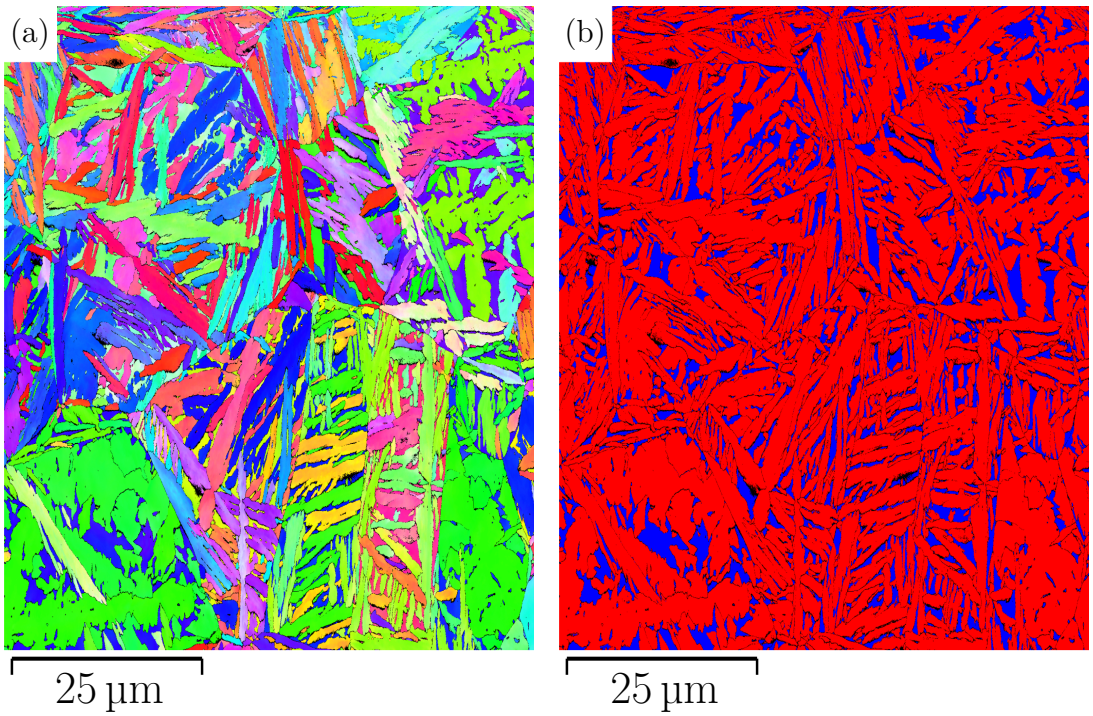


Figure B.2: EBSD orientation image, sample transformed isothermally at 250 °C for 150 h followed by cooling to ambient temperature. (a) Grain boundary nucleated bainite. (b) Distribution of retained austenite (blue) and bainitic ferrite (red).

Appendix C

SEM fractographs of Alloy B

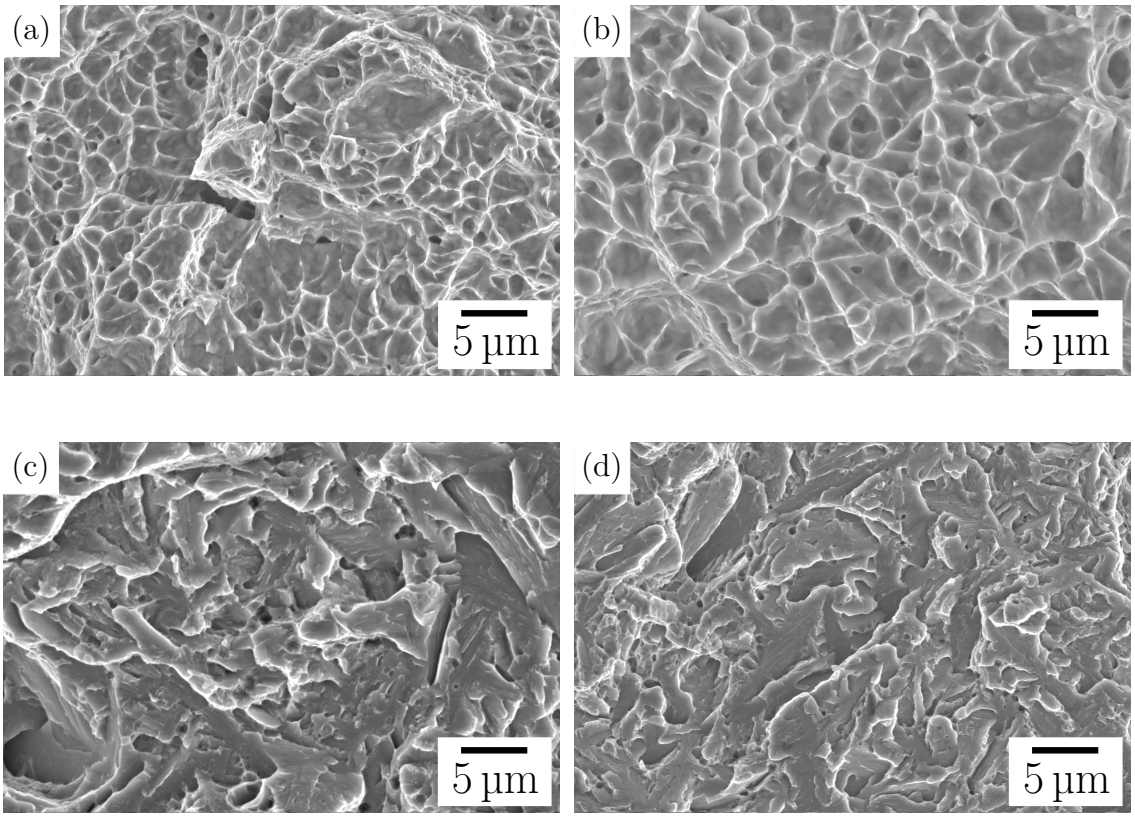


Figure C.1: Scanning electron micrographs of the fracture toughness test for (a,c) alloy with prior NiAl precipitates in as-transformed and tempered conditions respectively and (b,d) alloy without prior NiAl precipitates in the as-transformed and tempered conditions respectively.

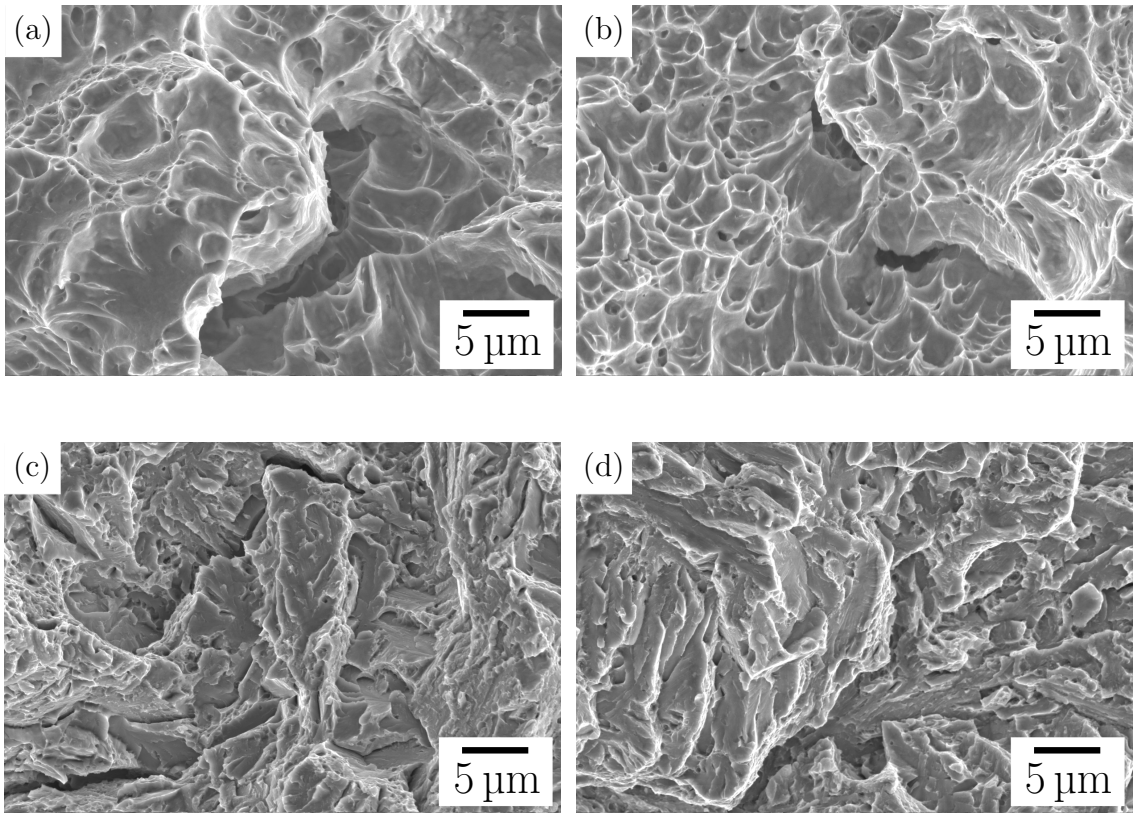


Figure C.2: Scanning electron micrographs of the Charpy impact test for (a,c) alloy with prior NiAl precipitates in as-transformed and tempered conditions respectively and (b,d) alloy without prior NiAl precipitates in as-transformed and tempered conditions respectively.

Bibliography

[1] H. K. D. H. Bhadeshia. *Bainite in Steels: Theory and Practice*. Maney Publishing, Leeds, U.K., 3rd edition, 2015.

[2] V. M. Segal, V. I. Reznikov, A. E. Drobyshevski, and V. I. Kopylov. Plastic treatment of metals by simple shear. *Russian Metallurgy* (Metally), 1:99–105, 1981.

[3] N. Tsuji, Y. Ito, Y. Saito, and Y. Minamino. Strength and ductility of ultrafine grained aluminium and iron produced by ARB and annealing. *Scripta Materialia*, 47:893–899, 2002.

[4] N. Tsuji. Unique mechanical properties of nanostructured metals. *Journal of Nanoscience and Nanotechnology*, 7:3765–3770, 2007.

[5] S. Tamimi, M. Ketabchi, and N. Parvin. Microstructural evolution and mechanical properties of accumulative roll bonded interstitial free steel. *Materials and Design*, 30:2556–2562, 2009.

[6] A. Cottrell. The importance of being imperfect. *European Review*, 1(July 2009):169–176, 1993.

[7] J. W. Christian. *Theory of Transformations in Metals and Alloys, Part I.* Pergamon Press, Oxford, U. K., 2nd edition, 1975.

[8] J. Christian. Recovery, Recrystallization and Grain Growth. In *The Theory of Transformations in Metals and Alloys*, pages 832–858. Elsevier Ltd, 2nd edition, 2002.

[9] A. Turner. Steels: Microstructure and properties. *Journal of Mechanical Working Technology*, 6(4):389–390, 1982.

[10] H. K. D. H. Bhadeshia and R. W. K. Honeycombe. *Steels–Microstructure and Properties*. Elsevier Ltd, Cambridge, 4th edition, 2017.

[11] E. O. Hall. The Deformation and Ageing of Mild Steel: III Discussion of Results. *Proceedings of the Royal Physical Society B*, 64:747–753, 1951.

[12] N. Petch. The fracture of metals. *Progress in Metal Physics*, 5(2):1–52, 1954.

[13] J. P. Naylor. The Influence of the Lath Morphology on the Yield Stress and Transition Temperature of Martensitic-Bainitic Steels. 10(July):861–873, 1979.

[14] J. Daigne, M. Guttmann, and J. P. Naylor. The Influence of Lath Boundaries and Carbide Distribution on the Yield Strength of 0.4% C Tempered Martensitic Steels. 56:1–10, 1982.

[15] T. Yokota, C. García-Mateo, and H. K. D. H. Bhadeshia. Formation of nanostructured steels by phase transformation. *Scripta Materialia*, 51:767–770, 2004.

[16] Rolls-Royce. *The Jet Engine*. Derby, 5th edition, 1986.

[17] J. M. Allwood, J. M. Cullen, M. A. Carruth, D. R. Cooper, M. McBrien, L. Milford, Rachel, M. C. Moynihan, and A. C. H. Patel. *Sustainable Materials With Both Eyes Open*. 2012.

[18] K. Fang, J. G. Yang, X. S. Liu, K. J. Song, H. Y. Fang, and H. K. D. H. Bhadeshia. Regeneration technique for welding nanostructured bainite. *Materials & Design*, 50:38–43, 2013.

[19] DoITPoMS - Micrograph Library. Avaible from `http://www.doitpoms.ac.uk/miclib/index.php`, University of Cambridge, 2015.

[20] T. Maki, S. Shimooka, S. Fujiwara, and I. Tamura. Formation Temperature

Thin Plate Martensite and Growth Behavior of in Fe-Ni-C Alloys. *Transactions of the Japan Instuitute of Metals*, 16:35–41, 1975.

[21] S. M. C. Van Bohemen, M. J. M. Hermans, and G. den Ouden. Monitoring of martensite formation during welding by means of acoustic emission. *Journal of Physics D: Applied Physics*, 34:3312–3317, 2001.

[22] F. Foerster and E. Scheil. Akustische Untershung der Bildung von Martensitnadeln. *Zeitschrift für Metallkunde*, 9:245–247, 1936.

[23] H. K. D. H. Bhadeshia. Interpretation of the Microstructure of Steels. Available from `https://www.phase-trans.msm.cam.ac.uk/2008/Steel_Microstructure/SM.html`, 2008.

[24] H. K. D. H. Bhadeshia and D. V. Edmonds. The Mechanism of Bainite Formation in Steels. *Acta Metallurgica*, 28:1265–1273, 1980.

[25] R. F. Hehemann. The bainite transformation. In H. I. Aaronson and V. F. Zackay, editors, *Phase Transformations*, pages 397–432, Materials Park, Ohio, USA, 1970. American Society of Materials.

[26] A. R. Troiano and A. B. Greninger. Transformation and retention of austenite in SAE 5140, 2340 and T1340 steels of comparable hardenability. *Transactions ASM*, 41:1093–1112, 1949.

[27] H. K. D. H. Bhadeshia and D. V. Edmonds. The Mechanism of Bainite Formation in Steels. *Acta Metallurgica*, 28:1265–1273, 1980.

[28] H. K. D. H. Bhadeshia and D. V. Edmonds. The bainite transformation in a silicon steel. *Metallurgical Transactions A*, 10A:895–907, 1979.

[29] H. K. D. H. Bhadeshia. Bainite: Overall transformation kinetics. *Journal de Physique Colloque*, C4 43:443–448, 1982.

[30] H. I. Aaronson and C. Wells. Sympathetic nucleation of ferrite. *Trans. A.I.M.E.*, 206:1216–1223, 1956.

[31] G. R. Speich. Growth Kinetics of Bainite in a Three Per Cent Chromium Steel. In V. F. Zackay and H. I. Aaronson, editors, *Decomposition of Austenite by Diffusional Processes*, pages 353–367. 1962.

[32] K. Shimizu, T. Ko, and Z. Nishiyama. Transmission Electron Microscope Observation of the Bainite of Carbon Steel. *Transactions of the Japan Instuitute of Metals*, 5:225–230, 1964.

[33] H. K. D. H. Bhadeshia and D. V. Edmonds. The bainite transformation in a silicon steel. *Metallurgical Transactions A*, 10A:895–907, 1979.

[34] H. K. D. H. Bhadeshia and D. V. Edmonds. Bainite in silicon steels: new composition–property approach Part 1. *Metal Science*, 17(September):420–425, 1983.

[35] J. Liu and C. P. Luo. Precipitation behavior of the lower bainitic carbide in a medium-carbon steel containing Si, Mn and Mo. *Materials Science and Engineering A*, 438-440:153–157, 2006.

[36] E. P. Klier and T. Lyman. The bainite reaction in hypoeutectoid steels. *Trans. A. S. M.*, 158:395–422, 1944.

[37] H. K. D. H. Bhadeshia. Bainite: The Incomplete-Reaction phenomenon and the approach to equilibrium. In M. S. H. I. Aaronson D. E. Laughlin and C. M. Wayman, editors, *Solid-Solid Phase Transformations*, pages 1041–1048, Materials Park, Ohio, USA, 1981. TMS-AIME.

[38] T. Lyman and A. R. Troiano. Influence of carbon content upon the transformations in 3% chromium steel. *Trans. ASM*, 37:402–448, 1946.

[39] L. C. Chang and H. K. D. H. Bhadeshia. Microstructure of lower bainite formed at large undercoolings below martensite start temperature. *Materials Science and Technology*, 12:233–236, 1996.

[40] E. Kozeschnik and H. K. D. H. Bhadeshia. Influence of silicon on cementite precipitation in steels. *Materials Science and Technology*, 24:343–347, 2008.

[41] H. K. D. H. Bhadeshia and J. W. Christian. Bainite in Steels. *Metallurgical Transactions A*, 21A:767–797, 1990.

[42] H. K. D. H. Bhadeshia. *Bainite in Steels*. Institute of Materials, London, 2nd edition, 2001.

[43] E. S. Davenport, E. C. Bain, and N. J. Kearny. Transformation of Austenite at Constant Subcritical Temperatures. *Transactions of the American Intsitute of Metallurgical Engineers*, 90:117–154, 1930.

[44] T. Ko and S. A. Cottrell. The formation of bainite. *Journal of the Iron and Steel Institute*, 172:307–313, 1952.

[45] D. Hull. The characteristics of the martensite transformation. *Bulletin of the Institute of Metals*, 2:134–139, 1954.

[46] J. W. Christian. Accommodation strains in martensite formation, the use of the dilatation parameter. *Acta Metallurgica*, 6:377–379, 1958.

[47] J. W. Christian. The origin of surface relief effects in phase transformations. In V. F. Zackay and H. I. Aaronson, editors, *Decomposition of austenite by diffusional processes*, pages 371–386, New York, USA, 1962. Interscience.

[48] E. Swallow and H. K. D. H. Bhadeshia. High resolution observations of displacements caused by bainitic transformation. *Materials Science and Technology*, 12:121–125, 1996.

[49] B. P. J. Sandvik. The Bainite Reaction in Fe-Si-C Alloys: The Primary Stage. *Metallurgical Transactions A*, 13:777–787, 1982.

[50] P. Yan and H. K. D. H. Bhadeshia. Mechanism and kinetics of solid-state transformation in high-temperature processed linepipe steel. *Metallurgical and Materials Transactions A: Physical Metallurgy and Materials Science*, 44:5468–5477, 2013.

[51] B. P. J. Sandvik and H. P. Nevalainen. Structure-property relationships in

commercial low-alloy bainitic-austenitic steel with high strength, ductility, and toughness. *Metals Technology*, 8:213–220, 1981.

[52] P. J. Withers and H. K. D. H. Bhadeshia. Residual stress. Part 2 – Nature and origins. *Materials Science and Technology*, 17:366–375, 2001.

[53] F. B. Pickering. Mechanism of bainite formation in low-alloy steels containing up to 0.4% carbon. In *4th International Conference on Electron Microscopy*, pages 626–637. Springer Verlag, Berlin, 1958.

[54] H. K. D. H. Bhadeshia and D. V. Edmonds. Bainite in silicon steels: new composition–property approach Part 2. *Metal Science*, 17:420–425, 1983.

[55] F. B. Pickering. The structure and properties of bainite in steels. In *Transformation and hardenability in steels*, pages 109–132, Michigan, USA, 1967. Climax Molybdenum Co.

[56] E. S. Davenport and E. C. Bain. Transformation of austenite at constant subcritical temperatures. *Trans. Am. Inst. Min. Metall. Engng.*, 90:117–154, 1930.

[57] K. J. Irvine and F. B. Pickering. The impact properties of low carbon bainitic steels. *Journal of the Iron and Steel Institute*, 201:518–531, 1963.

[58] D. B. McCutcheon, T. W. Trumper, and J. D. Embury. Controlled rolling of acicular ferrite plate. *Revue de Métallurgie*, 73:143–174, 1976.

[59] K. J. Irvine and F. B. Pickering. High-carbon bianitic steels. Technical report, Iron and Steel Institute, 1965.

[60] E. R. Morgan, T. E. Dancy, and M. Korchynsky. Improved HSLA steels through hot strip mill controlled cooling. *Blast furnace and steel plant*, 53: 921–929, 1965.

[61] A. J. DeArdo. Accelerated cooling: A physical metallurgy perspective. In

G. E. Ruddle and A. F. Crawley, editors, *Accelerated cooling or rolled steel*, pages 3–26, Oxford, U. K., 1988. Pergamon Press.

[62] V. F. Zackay. The enhancement of ductility in high-strength steels. *ASM Transactions Quaterly*, 60:252–259, 1967.

[63] O. Matsumura, Y. Sakuma, and H. Takechi. Enhancement of elongation by retained austenite in intercritical annealed 0.4C-1.5Si-0.8Mn steel. *Transactions of the Iron and Steel Institute of Japan*, 27:570–579, 1987.

[64] O. Matsumura, Y. Sakuma, and H. Takechi. TRIP and its kinetic aspects in austempered 0.4C-1.5Si-0.8Mn steel. *Scripta Metallurgica*, 27:1301–1306, 1987.

[65] K. S. Raghavan, A. S. Sastri, and M. J. Marcinkowski. Nature of the Work-Hardening Behavior in Hadfield's Manganese Steel. *The American Institute of Mining, Metallurgical, and Petroleum Engineers*, 245:1569–1575.

[66] F. G. Caballero, H. K. D. H. Bhadeshia, K. J. A. Mawella, D. G. Jones, and P. M. Brown. Very strong low temperature bainite. *Materials Science and Technology*, 18:279–284, 2002.

[67] C. García-Mateo, F. G. Caballero, T. Sourmail, M. Kuntz, J. Cornide, V. Smanio, and R. Elvira. Tensile behaviour of a nanocrystalline bainitic steel containing 3 wt% silicon. *Materials Science and Engineering A*, 549: 2–9, 2012.

[68] F. G. Caballero, H.-W. Yen, M. K. Miller, J.-R. Yang, J. Cornide, and C. García-Mateo. Complementary use of transmission electron microscopy and atom probe tomography for the examination of plastic accommodation in nanocrystalline bainitic steels. *Acta Materialia*, 59:6117–6123, 2011.

[69] C. García-Mateo, F. G. Caballero, and H. K. D. H. Bhadeshia. Low Temperature Bainite. *Journal de Physique IV*, 112:285–288, 2003.

[70] F. G. Caballero and H. K. D. H. Bhadeshia. Very strong bainite. *Current Opinion in Solid State and Materials Science*, 8:251–257, 2004.

[71] H. K. D. H. Bhadeshia. Hard bainite. *The Minerals, Metals and Materials Society*, 1:469–484, 2005.

[72] P. M. Brown and D. P. Baxter. Hyper-strength Bainitic steels. Technical report, Porton Down / Qinetiq, Salisbury / Farnborough, 2004.

[73] F. G. Caballero, C. García-Mateo, and M. K. Miller. Design of Novel Bainitic Steels: Moving from UltraFine to Nanoscale Structures. *Jom*, 2014.

[74] C. García-Mateo, F. G. Caballero, T. Sourmail, V. Smanio, and C. G. de Andres. Industrialised nanocrystalline bainitic steels. Design approach. *International Journal of Materials Research*, 105:725–734, 2014.

[75] C. García-Mateo, F. G. Caballero, and H. K. D. H. Bhadeshia. Acceleration of Low-temperature Bainite. *ISIJ International*, 43:1821–1825, 2003.

[76] C. García-Mateo and F. G. Caballero. Ultra-high-strength Bainitic Steels. *ISIJ International*, 45:1736–1740, 2005.

[77] F. G. Caballero, M. J. Santofimia, C. García-Mateo, J. Chao, and C. G. de Andres. Theoretical design and advanced microstructure in super high strength steels. *Materials & Design*, 30:2077–2083, 2009.

[78] S. B. Singh and H. K. D. H. Bhadeshia. Esitmation of Bainite Plate-Thickness in Low-Alloy Steels. *Materials Science and Engineering A*, 245: 72–79, 1998.

[79] L. Kaufman and M. Cohen. Thermodynamics and kinetics of martensitic transformations. *Progress in Metal Physics*, 7:165–246, jan 1958.

[80] H. K. D. H. Bhadeshia. A rationalisation of shear transformations in steels. *Acta Metallurgica*, 29:1117–1130, 1981.

[81] G. Ghosh and G. B. Olson. Computational thermodynamics and the kinetics of martensitic transformation. *Journal of Phase Equilibria*, 22:199–207, 2001.

[82] H. K. D. H. Bhadeshia. Very Short and Very Long Heat Treatments in the Processing of Steel. *Materials and Manufacturing Processes*, 25:1–6, 2010.

[83] F. G. Caballero, H. K. D. H. Bhadeshia, K. J. A. Mawella, D. G. Jones, and P. Brown. Very Strong, Low-Temperature Bainite. *Materials Science and Technology*, 18:279–284, 2002.

[84] C. Garcia-Mateo, F. G. Caballero, and H. K. D. H. Bhadeshia. Low-Temperature Bainite. *Journal de Physique Colloque*, 112:285–288, 2003.

[85] C. Garcia-Mateo, F. G. Caballero, and H. K. D. H. Bhadeshia. Development of Hard Bainite. *{ISIJ} International*, 43:1238–1243, 2003.

[86] A. A. Howe. Ultrafine grained steels: industrial prospects. *Materials Science and Technology*, 16(11):1264–1266, 2000.

[87] A. A. Howe. Industry perspective on ultrafine grained steels. *Materials Science and Technology*, 25:815–819, 2009.

[88] M. J. Peet, S. S. Babu, M. K. Miller, and H. K. D. H. Bhadeshia. Three-dimensional atom probe analysis of carbon distribution in low-temperature bainite. *Scripta Materialia*, 50:1277–1281, 2004.

[89] F. G. Caballero, M. K. Miller, S. S. Babu, and C. García-Mateo. Atomic scale observations of bainite transformation in a high carbon high silicon steel. *Acta Materialia*, 55:381–390, 2007.

[90] P. Bruna, T. Pradell, D. Crespo, C. García-Mateo, and H. K. D. H. Bhadeshia. Mössbauer Analysis of Low-Temperature Bainite. pages 338–343, 2005.

[91] F. Caballero, H. Bhadeshia, K. Mawella, D. Jones, and P. Brown. Design of

novel high strength bainitic steels: Part 1. *Materials Science and Technology*, 17(5):517–522, 2001.

[92] F. G. Caballero, H. K. D. H. Bhadeshia, K. J. A. Mawella, D. G. Jones, and P. M. Brown. Design of novel high strength bainitic steels: Part 2. *Materials Science and Technology*, 17:517–522, 2001.

[93] M. J. Peet. *Transformation and tempering of low-temperature bainite*. PhD thesis, University of Cambridge, 2010.

[94] J. G. Speer, D. V. Edmonds, F. C. Rizzo, and D. K. Matlock. Partitioning of carbon from supersaturated plates of ferrite, with application to steel processing and fundamentals of the bainite transformation. *Current Opinion in Solid State and Materials Science*, 8:219–237, 2004.

[95] M. Sherif. *Characterisation and Development of Nanostructured, Ultrahigh Strength, and Ductile Bainitic Steels*. Phd, University of Cambridge, 2009.

[96] C. García-Mateo, F. G. Caballero, and H. K. D. H. Bhadeshia. Mechanical properties of low-temperature bainite. *Materials Science Forum*, 500-501: 495–502, 2005.

[97] H. K. D. H. Bhadeshia. The first bulk nanostructured metal. *Science and Technology of Advanced Materials*, 14:14202, 2013.

[98] A. Saha Podder and H. K. D. H. Bhadeshia. Thermal stability of austenite retained in bainitic steels. *Materials Science and Engineering A*, 527:2121–2128, 2010.

[99] C. N. Hulme-Smith, I. Lonardelli, M. J. Peet, A. C. Dippel, and H. K. D. H. Bhadeshia. Enhanced thermal stability in nanostructured bainitic steel. *Scripta Materialia*, 69:191–194, 2013.

[100] K. H. Jack. Structural Transformations in the Tempering of High-Carbon Martensitic Steels. *Journal of the Iron and Steel Institute*, 169:26–36, 1951.

[101] H. J. Goldschmidt. A New Carbide in Chomium Steels. *Nature*, 162:855–856, 1948.

[102] J. van Aswegen, R. W. K. Honeycombe, and D. Warrington. Precipitation on stacking faults in Cr-Ni austenitic steels. *Acta Metallurgica*, 12:1–13, 1964.

[103] A. L. Bowman, G. P. Arnold, E. K. Storms, and N. G. Nereson. The crystal structure of $Cr_{23}C_6$. *Acta Crystallographica Section B Structural Crystallography and Crystal Chemistry*, 28:3102–3103, 1972.

[104] S. Murphy and J. A. Whiteman. The Kinetics of Mo_2C Precipitation in Tempered Martensite. *Metal Science*, 4:58–62, 1970.

[105] J. B. Lupton. The Kinetics of Mo2C Precipitation in Tempered Martensite. *Metal Science*, 5:160–160, 1971.

[106] K. J. Kurzydłowski and W. Zieliński. $Mo_2C \rightarrow Mo_6C$ carbide transformation in low alloy Cr-Mo ferritic steels. *Metal Science*, 18:223–224, 1984.

[107] E. Smith. An investigation of secondary hardening of a 1% vanadium - 0.2% carbon steel. *Acta Metallurgica*, 14:583–593, 1966.

[108] S. Yamasaki and H. K. D. H. Bhadeshia. Modelling and characterisation of V_4C_3 precipitation and cementite dissolution during tempering of Fe-C-V martensitic steel. *Materials Science and Technology*, 19:1335–1343, 2003.

[109] H. K. D. H. Bhadeshia and R. W. K. Honeycombe. *Steels–Microstructure and Properties*. 2006.

[110] A. Saha Podder. *Tempering of a Mixture of Bainite and Retained Austenite*. Phd, University of Cambridge, 2011.

[111] P. J. Jacques, Q. Furnémont, A. Mertens, and F. Delannay. On the sources of work hardening in multiphase steels assisted by transformation-induced plasticity. *Philosophical Magazine A*, 81:1789–1812, 2001.

[112] M. Sherif, C. Garcia-Mateo, T. Sourmail, and H. K. D. H. Bhadeshia. Stability of Retained Austenite in {TRIP}-Assisted Steels. *Materials Science and Technology*, 20:319–322, 2004.

[113] H. K. D. H. Bhadeshia. Properties of Fine-Grained Steels Generated by Displacive Transformation. *Materials Science and Engineering A*, 481-482: 36–39, 2008.

[114] E. F. Bailey. Effect of nonmartensite decomposition products on the properties of quenched and tempered steels. *Trans. A. S. M.*, 46:830–850, 1954.

[115] R. F. Hehemann, V. J. Luhan, and A. R. Troiano. The influence of bainite on mechanical properties. *Trans. A. S. M.*, 49:409–426, 1957.

[116] A. R. Troiano and L. J. Klinger. Limitations of the end-quench hardenability test. *Trans. A. S. M.*, 44:775–801, 1952.

[117] D. P. Edwards. Toughness of martensite and bainite in a 3\%{Ni Cr Mo V} steel. *Journal of the Iron and Steel Institute*, 207:1494–1502, 1969.

[118] T. A. Mutiu, A. J. Kinderman, and I. M. Bernstein. The effects of concurrent deformation on the transformation kinetics. In J. B. Ballance, editor, *The Hot Deformation of Austenite*, pages 410–427, Warrendale, Pennsylvania, USA, 1977. TMS-AIME.

[119] Y. Tomita and K. Okabayshi. Improvement in lower temperature mechanical properties of 0.40 Pct C-Ni-Cr-Mo ultrahigh strength steel with 2nd phase. *Metallurgical Transactions A*, 14:485–492, 1983.

[120] C. N. Hulme-Smith. *The thermal stability of bulk nanocrystalline steels.* PhD thesis, University of Cambridge, 2016.

[121] H. I. Aaronson and H. A. Domian. Partitioning of Alloying Elements Between Austenite and Proeutectoid Ferrite or Bainite. *Transactions Of The Metallurgical Society Of AIME*, 237:781–796, 1966.

[122] H. M. Rietveld. A profile refinement method for nuclear and magnetic structures. *Journal of Applied Crystallography*, 2:65–71, 1969.

[123] B. H. Toby. R factors in Rietveld analysis: How good is good enough? *Powder Diffraction*, 21(01):67–70, 2006.

[124] D. J. Dyson and B. Holmes. Effect of alloying additions on the lattice parameter austenite. *Journal of the Iron and Steel Institute*, 208:469–474, 1970.

[125] R. H. Davies, A. T. Dinsdale, J. A. Gisby, J. A. J. Robinson, and S. M. Martin. MTDATA-thermodynamic and phase equilibrium software from the national physical laboratory. *Calphad*, 26:229–71, 2002.

[126] TCAB thermodynamic database for steels version 1.0, 2001.

[127] J.-O. Andersson, T. Helander, L. Höglund, P. Shi, and B. Sundman. Thermo-Calc & DICTRA, computational tools for materials science. *CALPHAD*, 26: 273–312, 2002.

[128] B. Sundman, B. Jansson, and J.-O. Andersson. The Thermo-Calc databank system. *CALPHAD*, 9:153–190, 1985.

[129] NPL PLUS thermodynamic database version 3.02, 1993.

[130] H. S. Yang and H. K. D. H. Bhadeshia. Designing low carbon, low temperature bainite. *Materials Science and Technology*, 24:335–342, 2008.

[131] H. K. D. H. Bhadeshia. Thermodynamic analysis of isothermal transformation diagrams. *Metal Science*, 16:159–165, 1982.

[132] M. N. Shetty. Dislocations and mechanical behaviour of materials. *PHI Learning Pvt. Ltd*, 2013.

[133] G. E. Dieter. *Mechanical Metallurgy*. McGraw-Hill Book Company (U. K.) Limited, si metric edition, 1988.

[134] T. Okumura and T. Sourmail. MTTTData. Available from `http://www.msm.cam.ac.uk/map/steel/programs/MTTTDATA.html`, 2004.

[135] D. Bombač. Program for calculation of TTT diagrams in steels , version 3.0, 2015.

[136] H. S. Yang and H. K. D. H. Bhadeshia. Uncertainties in dilatometric determination of martensite start temperature. *Materials Science and Technology*, 23:556–560, 2007.

[137] SGTE thermodynamic Database for steels, version 4.2, 2006.

[138] P. J. Jacques, E. Girault, T. Catlin, N. Geerlofs, T. Kop, S. van der Zwaag, and F. Delannay. Bainite transformation of low carbon Mn–Si TRIP-assisted multiphase steels: influence of silicon content on cementite precipitation and austenite retention. *Materials Science and Engineering A*, 273-275:475–479, 1999.

[139] J. H. Jang, I. G. Kim, and H. K. D. H. Bhadeshia. Substitutional solution of silicon in cementite: A first-principles study. *Computational Materials Science*, 44:1319–1326, 2009.

[140] J. Gordine and I. Codd. The influence of silicon up to 1.5 wt% on the tempering characteristics of a spring steel. *Journal of the Iron and Steel Institute*, 207.1:461–468, 1969.

[141] S. Khare, K. Y. Lee, and H. K. D. H. Bhadeshia. Carbide-Free Bainite: Compromise between Rate of Transformation and Properties. *Metallurgical and Materials Transactions A*, 41:922–928, 2010.

[142] C. García-Mateo and F. G. Caballero. Understanding the Mechanical Properties of Nanostructured Bainite. In *NANOBAIN: Significant Extension of the Bainite Transformation Theory*, pages 35–65. 2015.

[143] H. K. D. H. Bhadeshia. Nanostructured bainite. *Proceedings of the Royal Society A: Mathematical, Physical and Engineering Sciences*, 466:3–18, 2009.

[144] H. S. Hasan, M. J. Peet, M.-N. Avettand-Fénoël, and H. K. D. H. Bhadeshia. Effect of tempering upon the tensile properties of a nanostructured bainitic steel. *Materials Science and Technology*, 615:1–22, 2014.

[145] H. K. D. H. Bhadeshia. Properties of fine-grained steels generated by displacive transformation. *Materials Science and Engineering A*, 481-482:36–39, 2008.

[146] B. Avishan, C. García-Mateo, L. Morales-Rivas, S. Yazdani, and F. G. Caballero. Strengthening and mechanical stability mechanisms in nanostructured bainite. *Journal of Materials Science*, 48:6121–6132, 2013.

[147] I. Lonardelli, M. Bortolotti, W. van Beek, L. Girardini, M. Zadra, and H. K. D. H. Bhadeshia. Powder metallurgical nanostructured medium carbon bainitic steel : Kinetics , structure , and in situ thermal stability studies. *Materials Science and Engineering A*, 555:139–147, 2012.

[148] C. Mack and M. S. Bartlett. On clumps formed when convex laminae or bodies are placed at random in two or three dimensions. *Mathematical Proceedings of the Cambridge Philosophical Society*, 52:246, 1956.

[149] H. S. Yang and H. K. D. H. Bhadeshia. Austenite grain size and the martensite-start temperature. *Scripta Materialia*, 60:493–495, 2009.

[150] H. K. D. H. Bhadeshia. Developments in martensitic and bainitic steels: role of the shape deformation. *Materials Science and Engineering A*, 378A: 34–39, 2004.

[151] S. Chatterjee, M. Murugananth, and H. K. D. H. Bhadeshia. δ TRIP steel. *Materials Science and Technology*, 23:819–827, 2007.

[152] L. Kaufman and M. Cohen. Thermodynamics and kinetics of martensitic transformation. *Progress in Metal Physics*, 7:165–246, 1958.

[153] D. Koistinen and R. Marburger. A general equation prescribing the extent of

the austenite-martensite transformation in pure iron-carbon alloys and plain carbon steels. *Acta Metallurgica*, 7:59–60, 1959.

[154] J. R. Patel and M. Cohen. Criterion for the action of applied stress in the martensitic transformation. *Acta Metallurgica*, 1(05):531–538, 1953.

[155] S. Denis, E. Gautier, A. Simon, and G. Beck. Stress-phase-transformation interactions – basic principles, modelling and calculation of internal stresses. *Materials Science and Technology*, 1:805–814, 1985.

[156] C. Zener. Equilibrium Relations in Medium-alloy Steels. *Transactions of the American Intsitute of Metallurgical Engineers*, 167:513–534, 1946.

[157] Secretary of State for Defence, H. K. D. H. Bhadeshia, C. Mateo, and P. Brown. Bainite steel and methods of manufacture thereof. Technical Report {GB}2462197, Intellectual Property Office, London, U.K., 2010.

[158] S. Jin, J. Morris, Y. L. Chen, G. Thomas, and R. I. Jaffee. An investigation of transformation strengthening in precipitation-hardened Fe-Ni austenite. *Metallurgical Transactions A*, 9:1625–1633, 1978.

[159] J. M. Dowling, J. M. Corbett, and H. W. Kerr. Inclusion phases+nucleation of acicular ferrite in SMA welds. *Metallurgical Transactions A*, 17:1611–1623, 1986.

[160] A. Ali and H. K. D. H. Bhadeshia. Aspects of the nucleation of {W}idmanstätten ferrite. *Materials Science and Technology*, 6:781–784, 1990.

[161] G. I. Rees, J. Perdrix, T. Maurickx, and H. K. D. H. Bhadeshia. The effect of niobium in solid solution on the transformation kinetics of bainite. *Materials Science & Engineering A*, 194:179–186, 1995.

[162] H. Mabuchi, R. Uemori, and M. Fujioka. Role of Mn depletion in intragranular ferrite transformation in the heat affected zone of welded joints with large heat input in structural steels. *ISIJ International*, 36:1406–1412, 1996.

[163] J. M. Gregg and H. K. D. H. Bhadeshia. Solid-state nucleation of acicular ferrite on minerals added to molten steel. *Acta Materialia*, 45:739–748, 1997.

[164] T. Furuhara, J. Yamaguchi, N. Sugita, G. Miyamoto, and T. Maki. Nucleation of proeutectoid ferrite on complex precipitates in austenite. *ISIJ International*, 43:1630–1639, 2003.

[165] H. Hu, G. Xu, L. Wang, Z. Xue, Y. Zhang, and G. Liu. The effects of Nb and Mo addition on transformation and properties in low carbon bainitic steels. *Materials Science & Engineering A*, 84:95–99, 2015.

[166] C. Stallybrass, A. Schneider, and G. Sauthoff. The strengthening effect of (ni,fe)al precipitates on the mechanical properties at high temperatures of ferritic fe–al–ni–cr alloys. *Intermetallics*, 13(12):1263 – 1268, 2005. Discussion Meeting on the Development of Innovative Iron Aluminium Alloys.

[167] Z. B. Jiao, J. H. Luan, M. K. Miller, and C. T. Liu. Precipitation mechanism and mechanical properties of an ultra-high strength steel hardened by nanoscale nial and cu particles. *Acta Materialia*, 97:58 – 67, 2015.

[168] C. N. Hulme-Smith, S. W. Ooi, and H. K. D. H. Bhadeshia. Intermetallic-strengthened nanocrystalline bainitic steel. *Materials Science and Technology*, 34(16):1976–1979, 2018.

[169] R. P. Kolli and D. N. Seidman. The temporal evolution of the decomposition of a concentrated multicomponent fe–cu-based steel. *Acta Materialia*, 56(9): 2073 – 2088, 2008.

[170] M. Kapoor, D. Isheim, S. Vaynman, M. Fine, and Y.-W. Chung. Effects of increased alloying element content on nial-type precipitate formation, loading rate sensitivity, and ductility of cu- and nial-precipitation-strengthened ferritic steels. *Acta Materialia*, 104:166 – 171, 2016.

[171] Z. B. Jiao, J. H. Luan, W. Guo, J. D. Poplawsky, and C. T. Liu. Atom-probe study of cu and nial nanoscale precipitation and interfacial segregation in a

nanoparticle-strengthened steel. *Materials Research Letters*, 5(8):562–568, 2017.

[172] A. G. Allten. Discussion to "the effect of silicon on the kinetics of tempering". *Trans. ASM*, 46, 812-829 1954.

[173] E. W. Langer. An Investigation of Carbide Precipitation in Iron. *Metal Science*, 2:59–66, 1968.

[174] M. S. Bhat. *Microstructure and mechanical properties of AISI 4340 Steel modified with Al and Si*. PhD thesis, Lawrence Berkley Laboratories, California, USA, 1977.

[175] H. K. D. H. Bhadeshia. Cementite. *International Materials Reviews*, 64: https://doi.org/10.1080/09506608.2018.1560984, 2019.

[176] E. Kozeschnik. MATCALC - a simulation tool for multicomponent thermodynamics, diffusion and phase transformations. In *Fifth International Seminar on the Numerical Analysis of Weldability*, pages 349–361, 1999.

[177] E. Povoden-Karadeniz. MATCALC thermodynamic database for iron v2.021. Technical report, 2014.

[178] H. K. D. H. Bhadeshia, S. A. David, J. M. Vitek, and R. W. Reed. Stress induced transformation to bainite in Fe-Cr-Mo-C pressure vessel steel. *Materials Science and Technology*, 7:686–698, 1991.

[179] H. K. D. H. Bhadeshia. Thermodynamic Extrapolation and the Martensite-Start Temperature of Substitutionally Alloyed Steels. *Metal Science*, 15: 178–180, 1981.

[180] F. G. Caballero, J. Chao, J. Cornide, C. García-Mateo, M. J. Santofimia, and C. Capdevila. Toughness deterioration in advanced high strength bainitic steels. *Materials Science and Engineering A*, 525:87–95, 2009.

[181] S. S. Babu, S. Vogeld, C. Garcia-Mateo, B. Clausen, L. Morales-Rivas, and

F. G. Caballero. Microstructure evolution during tensile deformation of a nanostructured bainitic steel. *Scripta Materialia*, 69:777–780, 2013.